NUMERICAL STUDY OF RAYLEIGH BÉNARD THERMAL CONVECTION VIA SOLENOIDAL BASES

A THESIS SUBMITTED TO
THE GRADUATE SCHOOL OF NATURAL AND APPLIED SCIENCES
OF
MIDDLE EAST TECHNICAL UNIVERSITY

BY

CİHAN YILDIRIM

IN PARTIAL FULFILLMENT OF THE REQUIREMENTS
FOR
THE DEGREE OF DOCTORATE
IN
ENGINEERING SCIENCES

March 2011

Approval of the thesis:

NUMERICAL STUDY OF RAYLEIGH BÉNARD THERMAL CONVECTION VIA SOLENOIDAL BASES

submitted by **CİHAN YILDIRIM** in partial fulfillment of the requirements for the degree of **Doctorate in Engineering Sciences Department, Middle East Technical University** by,

Prof Dr. Canan Özgen ______________
Dean, Graduate School of **Natural and Applied Sciences**

Prof. Dr. Turgur Tokdemir ______________
Head of Department, **Engineering Sciences**

Assoc. Prof. Dr. Hakan I. Tarman ______________
Supervisor, **Department of Engineering Sciences**

Examining Committee Members:

Prof. Dr. Turgut Tokdemir
Dept. of Eng. Sci., METU ______________

Assoc. Prof. Dr. Hakan I. Tarman
Dept. of Eng. Sci., METU ______________

Assoc. Prof. Dr. Erol Kurt
Faculty of Tech. Edu., Gazi University ______________

Assoc. Prof. Dr. Utku Kanoğlu
Dept. of Eng. Sci., METU ______________

Assist. Prof. Dr. Cüneyt Sert
Dept. of Mech. Eng., METU ______________

Date: ______________

I hereby declare that all information in this document has been obtained and presented in accordance with academic rules and ethical conduct. I also declare that, as required by these rules and conduct, I have fully cited and referenced all material and results that are not original to this work.

Name, Last Name: CİHAN YILDIRIM

Signature :

ABSTRACT

NUMERICAL STUDY OF RAYLEIGH BÉNARD THERMAL CONVECTION VIA SOLENOIDAL BASES

Yıldırım, Cihan
Ph.D., Department of Engineering Sciences
Supervisor : Assoc. Prof. Dr. Hakan I. Tarman

March 2011, 140 pages

Numerical study of transition in the Rayleigh-Bénard problem of thermal convection between rigid plates heated from below under the influence of gravity with and without rotation is presented. The first numerical approach uses spectral element method with Fourier expansion for horizontal extent and Legendre polynomal for vertical extent for the purpose of generating a database for the subsequent analysis by using Karhunen-Loéve (KL) decomposition. KL decompositions is a statistical tool to decompose the dynamics underlying a database representing a physical phenomena to its basic components in the form of an orthogonal KL basis. The KL basis satisfies all the spatial constraints such as the boundary conditions and the solenoidal (divergence-free) character of the underlying flow field as much as carried by the flow database. The optimally representative character of the orthogonal basis is used to investigate the convective flow for different parameters, such as Rayleigh and Prandtl numbers.

The second numerical approach uses divergence free basis functions that by construction satisfy the continuity equation and the boundary conditions in an expansion of the velocity flow field. The expansion bases for the thermal field are constructed to

satisfy the boundary conditions. Both bases are based on the Legendre polynomials in the vertical direction in order to simplify the Galerkin projection procedure, while Fourier representation is used in the horizontal directions due to the horizontal extent of the computational domain taken as periodic. Dual bases are employed to reduce the governing Boussinesq equations to a dynamical system for the time dependent expansion coefficients. The dual bases are selected so that the pressure term is eliminated in the projection procedure. The resulting dynamical system is used to study the transitional regimes numerically.

The main difference between the two approaches is the accuracy with which the solenoidal character of the flow is satisfied. The first approach needs a numerically or experimentally generated database for the generation of the divergence-free KL basis. The degree of the accuracy for the KL basis in satisfying the solenoidal character of the flow is limited to that of the database and in turn to the numerical technique used. This is a major challenge in most numerical simulation techniques for incompressible flow in literature. It is also dependent on the parameter values at which the underlying flow field is generated. However the second approach is parameter independent and it is based on analytically solenoidal basis that produces an almost exactly divergence-free flow field. This level of accuracy is especially important for the transition studies that explores the regions sensitive to parameter and flow perturbations.

Keywords: Solenoidal Basis, Karhunen-Loéve Analysis, Rayleigh-Bénard Convection, Rotating Rayleigh-Bénard Convection, Galerkin Projection, Spectral Methods

ÖZ

SOLENOIDAL BAZLARLA RAYLEIGH BÉNARD ISI KONVEKSİYONU ÜZERİNE SAYISAL ÇALIŞMA

Yıldırım, Cihan
Doktora, Mühendislik Bilimleri Bölümü
Tez Yöneticisi : Doç. Dr. Hakan I. Tarman

Mart 2011, 140 sayfa

Yerçekimi etkisinde bulunan alttan ısıtılmış iki rijit tabaka arasındaki dönen ve dönmeyen Rayleigh-Bénard ısı konveksiyonunun geçiş evreleri sayısal yaklaşım ile incelenmiştir. Birinci yaklaşım, Karhunen-Loéve (KL) ayrıştırmasıyla analiz yapmak için veritabanı oluşturmak amacıyla, yatay düzlemde Fourier serileri ve düşey düzlemde Legendre polinomlarını kullanan spektral elamanlar metodunu kullanmaktadır. KL ayrıştırması, fiziksel olguyu ifade eden veritabanının dinamiğini ortogonal KL bazları cinsinden basit bileşenlerine ayrıştırmak için kullanılan istatiksel bir araçtır. KL bazları, sınır şartları, akış alanı ve akış veritabanının temelini oluşturan solenoidal karakter gibi bütün uzamsal kısıtlamaları sağlamaktadır. Ortogonal bazların sistemi optimum açıklama kabiliyeti konvektif akışın Rayleigh ve Prandtl sayıları gibi farklı parametreleri için incelenmiştir.

İkinci yöntem konvektif hız alanını açmak için süreklilik denklemini ve sınır şartlarını sağlayan diverjanstan bağımsız bazları kullanmaktadır. Isı alanı için kullanılan bazlar sınır şartlarını sağlayacak şekilde oluşturulmuşlardır. Her iki baz düşey düzlemde Legendre polinomları tarafından açımlanmaktadır. Yatay düzlemin periyodik kabulu

neticesinde Fourier açılımının kullanılması ile birlikte sistem Galerkin projeksiyon yöntemi ile sadeleştirilmiştir. Çifteş bazları dinamik sistemin Boussinesq temel denklemlerini zamana bağlı açılım katsayıları cinsine indirgeyebilmek için kullanılmıştır. Projeksiyon bazları basınç terimini projeksiyon işleminde elimine edecek şekilde seçilmiştir. Elde edilen dinamik sistem geçiş rejimlerinin sayısal incelemesinde kullanılmaktadır.

İki yaklaşım arasındaki temel fark diverjansdan kaynaklı hatalardan oluşan sayısal kirlenmedir. Akışkanlar dinamiği problemlerinde süreklilik denkleminin sağlanması büyük bir problemdir. Birinci metod akış alanının analizi için tam simülasyona ihtiyaç duyar, dolayısıyla sayısal hatalardan etkilenir. Bununla beraber ikinci metod analitik olarak diverjanstan bağımsız bazlara dayanır.

Anahtar Kelimeler: Solenoidal bazlar, Karhunen-Loéve Analizi, Rayleigh-Bénard Konveksiyonu, Dönen Rayleigh-Bénard Konveksiyonu, Galerkin Projeksiyonu, Spektral Metodlar

to my family

ACKNOWLEDGMENTS

I would like to express his gratitude to all those who gave him the possibility to complete this thesis.

The author is deeply indebted to his supervisor Assoc. Prof. Dr. Hakan I. Tarman his continuous support and help, stimulating suggestions, criticism and encouragement helped him in all the time of research and writing of this thesis.

During the PhD period, I am supported and encouraged by my parent to go ahead with my thesis. I furthermore wish to express my deepest gratitude to each member of my family for provided me a comfortable and excellent enviroment.

I would like to thank Prof. Dr. M. Ruşen Geçit and Prof. Dr. Turgut Tokdemir for all their help, support and interest. I would also like to thank Assoc. Prof. Dr. Erol Kurt, Assoc. Prof. Dr. Utku Kanoğlu and Assist. Prof. Dr. Cüneyt Sert for their criticisms and suggestions.

I would like to thank my friends, Durmuş Yarımpabuç, Baran Aydın, Ozan Tuğluk, Ersan Güray and Cengizhan Durucan for their help, suggestions and friendship.

In addition to these people, open source community, especially Debian and Gfortran teams contribute their knowledge, experience and self devotion to my works.

This study was supported by The Scientific and Technological Research Council of Turkey (TÜBİTAK-109M435) and State Planning Organization (BAP-08-11-DPT-2002K120510)

TABLE OF CONTENTS

LIST OF TABLES

TABLES

LIST OF FIGURES

FIGURES

CHAPTER 1

INTRODUCTION

1.1 RAYLEIGH BÉNARD CONVECTION

Thermal convection in a fluid layer has been a cradle of nonlinear stability studies. The classical Rayleigh-Benard problem of thermal convection in a horizontal layer heated from below has been the most studied problem amongst the natural convective flows. This is due to its transition dynamics exhibiting a sequence of discrete steps from steady regime to periodic, quasi-periodic regimes and eventually to chaotic regime as well as the simplicity of the geometry. The geometry of infinite fluid layer confined between rigid plates has been approximated by a periodic horizontal extent in the numerical studies and by large-aspect-ratio containers in the experiments.

Rayleigh-Benard thermal convection occurs if the temperature difference between the bottom and top layer is high enough. Natural convection phenomena are quite relevant in both natural and industrial applications. Some astrophysical phenomena such as solar granulation or convection in the planetary boundary layer and some industrial processes such as thermal convection in electric power industry (especially in nuclear reactors cooling), cooling electronic components, solar heating devices and crystallization processes involve this phenomena. The dynamics is governed by three non-dimensional parameters: Rayleigh number, Prandtl number and the aspect ratio of the convective box. Depending on these parameters, the flow exhibits a number of discrete transitions before reaching turbulence.

Rayleigh-Benard thermal convection in a periodic box is investigated in this thesis because it has the simple geometry to adapt the numerical procedure easily. Abundant studies in literature make it convenient to test and compare new numerical approaches.

1.1.1 NUMERICAL AND EXPERIMENTAL INVESTIGATIONS

The literature on numerical studies of the Rayleigh-Benard problem can be collected in two main categories. First category involves the stability analysis. Second category involves numerical simulation for the different aspects of the convection, e.g. heat transfer, turbulence, etc.

Henri Bénard showed the formation of steady hexagonal flow pattern between very thin layer (Bénard 1901). Lord Rayleigh introduced theoretical explanation of Bénard's results and determined stability condition of flow heated from below and cooled from above (Rayleigh 1916). He showed that fluid layer is motionless if the temperature gradient is small. When the temparature gradient reaches to a spesific value corresponding to a critical value of Rayleigh number, the fluid layer looses its stability. The system reaches to a new stable state in which convective rolls transport the heat flux.

Early thoretical works dealt with stability analysis and heat transport of the convective motion. Malkus [3] theoretically investigated various properties of the turbulent convection especially maximum heat transport capacity and its constraint. Malkus and Veronis [4] determined the amplitude and the form of the thermal convection and its dependencies caused by external disturbance. Chandrasekhar [2] extensively explained the various features of hydrodynamic and hydromagnetic stability in his well-known book. Schlüter, Lortz and Busse [5] proved Malkus's "Hypothesis of maximum heat transport" for finite amplitude steady solution. They showed that all steady solutions of convection are unstable except the two dimensional roll motion.

Most of the numerical works utilized finite difference and finite volume methods. Spectral methods has been used extensively after the Orszag and co-authors' works. Plows [6] used two dimensional iterative finite difference technique to calculate convective heat flux and compare his results with early works. He investigated the relation between Nusselt number and mesh density, iteration cycles and extrapolation zero zone thickness for steady two dimensional convection.

Busse and his co-authors widely conducted experimental [7, 8] and numerical works [1, 9, 10, 11]. They used a Galerkin method to investigate instabilities and transition for different Prandtl number in the numerical studies. Clever and Busse [1] focused on the stability of the two dimensional roll motion with three dimensional disturbances. They showed the features of a number of instabilities with different control parameters. They worked on [9] the steady solution of two dimensional rolls for low Prandtl number range. They performed some numerical experiments to demonstrate the effect of the Prandtl number on the nonlinear heat transport character. They also inspected nonlinear features of oscillatory convection for different Prandtl, Rayleigh numbers and wavenumber combination in the paper [11]. Frick, Busse and Clever [10] investigated bimodal convection and square pattern convection for high Prandtl number fluid. They obtained steady solution in the limit of infinite Prandtl number and investigated its stability with galerkin approach. Further, Busse and Clever [12] discussed the symmetry considerations in the bifurcated solution of the numerical analysis.

Another important and widely referenced study is by Lipps. He used finite differences to calculate the three dimensional thermal convection in air for different regimes [13]. He calculated some illuminative properites of motion such as heat flux, kinetic energy etc. Grötzbach investigated convection in air with a finite volume code (TURBIT-3) considering the mesh requirements of the Rayleigh-Bénard problem [14, 15].

The transition to turbulance was studied by Mclaughlin and Orszag for air. They used a spectral method utilizing Fourier representation and Chebyshev polynomials with flow symmetries to simulate transition to turbulent regime for air. They searched the frequency content of different regimes in view of Ruelle-Takens Theory. [16]. Meneguzzi et. al simulated low Prandtl number fluid using pseudospectral method [17] for both free and rigid boundaries. They also discussed the effect of a magnetic force parallel to the roll axis. Verzicco and Camussi investigated the Prandtl variation effect on the Nusselt number. They conducted three sets of studies including low to high Prandtl number range numerical experiment using second order finite difference method [18].

More recently, Guessous proposed a numerical procedure that utilizes Fourier series and Legendre interpolants to investigate corelations between dimensionless parameters in natural convection in her PhD thesis [19]. She extended this procedure to the forced convection problem [20] as well.

Busse and Whitehead [7] showed the development of different oscillatory instabilities included cross roll, zigzag, pinching instabilities for varying wavenumber. They provided some explanatory shadowgraph illustrations of these instabilities. They also conducted some experiments [8]on the oscillatory instability of bimodal convection for high Prandtl number fluids.

Krishnamurti investigated convection at several different Prantl number values and indicated the relationship between Prandtl and Rayleigh numbers for different regimes [21]. Krishnamurti produced a parametric flow regime diagram which includes stability condition of two dimensional rolls, bimodal convection and oscillatory convection in that experimental work. According to this diagram transition range between conduction and turbulent convection regimes increasing with increasing Prandtl number. The underlying nonlinear instability mechanisms of transition has been extensively studied experimentally by Krishnamurti [21], Golub and Benson [22], Busse [23].

Somerville and Lipps [24] invastigated the difference between two dimensional and three dimensional modelling of Rayleigh-Bénard problem with rigid boundaries. They found increase in the wavelength of the convective structures in their three dimensional simulation as indicated by experimental studies. Koschmieder [25] reviewed many theoretical, numerical and experimental work in literature about the Rayleigh-Bénard convection.

1.1.2 RAYLEIGH BÉNARD CONVECTION WITH ROTATION

Many geophysical and astrophysical phenomena such as flow motion in oceans, stars or planets are affected by the rotational forces in addition to the thermal forces. Miesch [26] reviewed some of these work about solar convection with rotation. Evonuk and Glatzmaier [27] studied the effect of planetary rotation rate on the pattern of thermal convection for giant planets.

In earlier time, Veronis contributed to the current knowledge on convection with rotation in literature. He generally worked on the two dimensional system with stress free boundary conditions. He [28] observed that steady finite amplitude convection can exist for lower than the critical Rayleigh number for a limited range of rotation. Veronis [29] theoretically examined the effects of rotation and viscosity on the cellular motion of convection for different boundary conditions. He clearly explained the energy releasing and dissipative mechanisms in regards to viscosity. Veronis also [30] examined the differences between convection in low Prandtl and high Prandtl fluids confined in rotating two dimensional stress free boundaries. He observed the unstable behaviour for low Prandtl numbers. Because of this unstability, convective motion starts at lower than the critical Rayleigh number. Finite amplitude instability occurs due to the nonlinear effects but it can be damped by the increasing rotation.

Clever and Busse [31] investigated the stability of two dimensional convection under three dimensional disturbances. They considered rigid plates rotating around its vertical axis. They obtained some quantitative stability criterion depending on the varied rotation and constructed a stability diagram of the natural convection with respect to rotation. They observed that coriolis force reduces the heat transport for low Rayleigh and high Prandtl numbers flow. On the other hand, limited rotation is observed to enhance the heat transport for decreasing Prandtl number.

Rossby [32] investigated the natural convection in several fluids confined between rotating and stationary plates, experimentaly. He tested the predictions of the stability theory on the onset of convection. He also tried to determine the relation between heat flux and control parameters. He found finite amplitude instability in mercury for a limited range of rotation. Küppers and Lortz [33] theoretically investigated the stability behavior for a specific case, infinite Prandtl number and free-free boundaries. They showed that there is no stable steady-state convection for higher than the critical Taylor number, $Ta^2 = 2285$ ($\Omega \approx 23.9$). Küppers [34] conducted the same analysis in [33] and extended the work to rigid boundaries and finite Prandtl number.

Somerville and Lipps [35] repeated Rossby's work in a three dimensional numerical simulation. They studied experimentally observed quasi-steady or quasi-two dimensional flows by numerical simulation at the same experimental parameters of

Rossby's. Clune and Knobloch [36] focused on the previous experimental work and obtained the results of linear stability and weakly nonlinear calculations under the same experimental conditions. They calculated critical points, hopf frequency, critical Taylor number affected by Küppers-Lortz instability and the angle of rotated rolls. Scheel [37] in her Phd work investigated pattern formation and spatiotemporal chaos in rotating frame. She also investigated the stability of Rayleigh Bénard convection with rotation. Recently Clever and Busse [38] studied numerically two and three dimensional convection under the influence of rotation. Unusual dynamical features for low Prandtl number were the main attention in their work.

Kurt et. al. [39, 40] studied rotating cylindrical annulus with small gap approximation. They conducted stability analysis of convection influenced by rotation and magnetic field. They also observed some instabilities.

1.2 KARHUNEN LOÉVE DECOMPOSITION

The Karhunen-Loéve (KL) procedure was proposed independently by Karhunen [41] and Loéve [42]. This technique is used in many different fields including the identification of coherent structures in turbulent flows, low dimensional representation of PDEs, filtering data, reconstruction of incomplete data, face recognition, image compression, etc. Main idea of this procedure is capturing the dominant features in numerically or experimentally generated database representing a phenomena. It is also known as Proper Orthogonal Decomposition (POD), Principal Component Analysis (PCA) or Empirical Orthogonal Function (EOF) in the literature. Popularity of the method increases with increasing computational capabilities and new fields of applications.

In early times, Lorenz proposed a weather forecasting method based on EOF [43] in his scientific report. Lumley used this method in his turbulence work with the name of POD and provided the conceptual details to the turbulence community [44]. His book [45] is also an important contribution to the fluid mechanics literature. Different aspects of this procedure for fluid problems especially for turbulence can be found in the book by Holmes *et.al*. [46].

Sirovich [47, 48, 49] provided a systematic formulation of the KL procedure and proposed the method of snapshots to extract the KL modes or coherent structures in large data sets representing turbulent flow. He introduced a practical methodology of constructing the KL modes by decomposing the covariance tensor for fluid mechanics problems. This methodology requires enough data in order to capture all the features of the flow experimentally or numerically. He proposed to use physical symmetries in order to expand the available data and provide more features about the flow for robust analysis. Applications of this procedure to minimal channel flow problem explained in Webber, Handler and Sirovich [50] and Webber [51]. They constructed the velocity field using Chebyshev-Fourier spectral method and then produced optimal KL basis which best represent the turbulance in channel flow in energy sense.

Tarman [52] used this decomposition technique for turbulent natural convection with stress free boundaries. He separated the flow into mean and fluctuating components and used the fluctuation component to construct the covariance matrix. He used symmetry and translational invariance to enhance the flow sample. As a continuation, Tarman [53] used this technique in order to construct a reduced order approximation to Boussinesq equations. The energy content of the KL modes is used to devise a truncation scheme towards a dynamical approximation. Further, Tarman [54] incorporated the truncated modes into the dynamical approximation in order to recapture the lost dissipative effects without increasing the degrees of freedom. Tarman and Sirovich [55] extended the previous work [54] by generating the KL bases using the the mechanical and thermal fields separately and without separating the flow field into the mean and the fluctuating components. This removed the need to model the time rate of change of the mean flow, separately and so increased the accuracy. Tarman [56] performed a parametric study of Rayleigh-Bénard convection in air with stress free boundaries in a periodic box by varying Rayleigh number. He used thermal and mechanical KL bases obtained from a thermal convection database for this purpose. The results of this work is in qualitative agreement with literature.

More recently, Yıldırım, Yarımpabuç and Tarman [57] conducted some numerical experiment with Rayleigh-Bénard convection with rigid boundaries. They used KL bases to reduce the Boussinesq equations to a low dimensional dynamical system. The resulting system is used to study the transition regimes as Rayleigh number varied for low, unity and high Prandtl numbers. The issue of the KL basis being poorly solenoidal is raised here. The KL basis reflects the nature of the underlying numerical flow field. Unfortunately, numerical schemes available for resolving the continuity equation generally produce poorly solenoidal flow field.

1.3 DIVERGENCE FREE METHODS

The incompressibility condition appears as a constraint in the governing system of equations and is an important source of difficulty in numerical simulations. There are schemes developed solely to satisfy the continuity constraints such as fractional step scheme Orszag and Kells [58] and a spectral scheme by Kleiser and Schumann [59].

Others used representations which inherently satisfy the continuity constraints in a Galerkin approach. Moser, Moin and Leonard [60] presented a spectral method to automaticaly satisfy the continuity equation and boundary conditions and tested for the channel flow and the flow between concentric cylinders. They expanded the vertical and horizontal extend with Chebyshev polynomials and Fourier series, respectively. They used the benefit of cosine Fourier transform for Chebyshev polynomial representation, but had to tackle the non-unity weight function associated with Chebyshev polynomials. They reported that their low dimensional representation help to save on computer storage in addition to provide operational efficiency. They also investigated aliasing error for time dependent and steady flow.

Kessler [61] studied steady and oscillatory regimes of Rayleigh Bénard convection with explicitly constructed solenoidal basis based on poloidal-toroidal decomposition. Trigonometric polynomials and the beam functions are used in the construction of the solenoidal basis satisfying the boundary conditions in a rectangular container. The effects of the adiabatic and conduction sidewalls on the convective structures are investigated. Noack and Eckelmann [62] constructed a low dimensional Galerkin method with divergence free basis for the three dimensional flow around a circular cylinder. They discussed the advantages and disadvantages of this Galerkin solution as compared to other simulation.

Gelfgat [63] carried out a parametric study for two and three dimensional Rayleigh-

Bénard convection in rectangular 2D and 3D boxes with divergence free Galerkin method based on Chebyshev polynomials of the first and the second type. Puigjaner, Herrero, Giralt and Simó [64] studied stability and bifurcation in convective flow in air in a cubical cavity heated from below numerically. They used a divergence free Galerkin spectral method to discretize the system and a parameter continuation method to determine the different branches of solution. They used combination of trigonometric and hyperbolic function instead of Jacobi family function.

Most recently Meseguer and Trefethen reported [65, 66] a spectral Petrov-Galerkin formulation based on divergence free basis. They used this new method to study linear stability analysis of pipe flow in their first report. In latter report they investigated nonlinear evolution of pipe flow. They evaluated nonlinear terms by transforming between real and Fourier spaces. They also used this technique to investigate high Reynolds pipe flow [67].

The use of solenoidal type representation is especially useful in applying the techniques of bifurcation theory to the resulting dynamical system representation of the problem. For the optimal flow control problems, on the other hand, it means a reduction in the number of constraints to satisfy when searching for an optimal solution within the flow constraints. In this study, we extend the approach presented in previous work on the study of linear stability and nonlinear simulation of transition in thermal convection. The solenoidal basis is based on Legendre polynomial expansion of the flow field in the vertical wall direction. This representation provides a simpler form of the basis and highly accurate quadrature for evaluating integrals arising from Galerkin projection onto the dual space.

1.4 SCOPE OF THE WORK

In this thesis, the physics of Rayleigh-Bénard convection explained and governing equations are derived in chapter 2. A spectral element method is implemented to solve the governing PDE with dealiasing and explained in chapter 3. KL representation of the resulting solution database is used to analyse the underlying convection phenomena in this chapter as well. In chapter 4, divergence-free basis and solenoidal spectral method are introduced. In addition to the linear stability analysis using solenoidal spectral method, the implementation of time solver and the treatment of the nonlinear terms are discussed. The Fortran code developed for the implementation of divergence free spectral method is tested and the results are presented in chapter 5. The effect of rotation on Rayleigh-Bénard convection is studied using soleniodal spectral method in chapter 6. The results are discussed in chapter 7. Finally, a detailed formulation of the KL decomposition and a flow chart representation of the code are presented in the appendices.

CHAPTER 2

RAYLEIGH-BÉNARD PROBLEM

2.1 GOVERNING EQUATIONS

A viscous, incompressible fluid layer with periodic horizontal extent confined between two isothermal, rigid, parallel infinite plates seperated by a distance $H = 2h$ is considered for Rayleigh-Bénard convection problem. If the temperature at the bottom plate is high enough in comparison to the top plate, hot fluid will tend to rise due to bouyoncy force and cold fluid will tend to sink due to gravity. This mechanism produces "cell" pattern which transport heat from bottom to top plates. When temperature differences ΔT between the plates is high enough, the cell pattern exhibits increasingly complex behavior eventually reaching to disorderly state or chaos.

Rayleigh-Bénard problem is governed by a system of partial differential equations reduced from the Navier-Stokes equations by Oberbeck-Boussinesq (or Boussinesq) approximation. According to this approximation temperature differences in the plates are assumed small and all fluid property is assumed independent of the temperature except buoyancy term. Thus fluid density ρ is considered to depend linearly on the temperature [68].

A cartesian space is considered with the z-axis directed vertically upwards opposing the gravity direction between $-H/2 < z < H/2$. Rayleigh-Benard convection is governed by Boussinesq equations in the form:

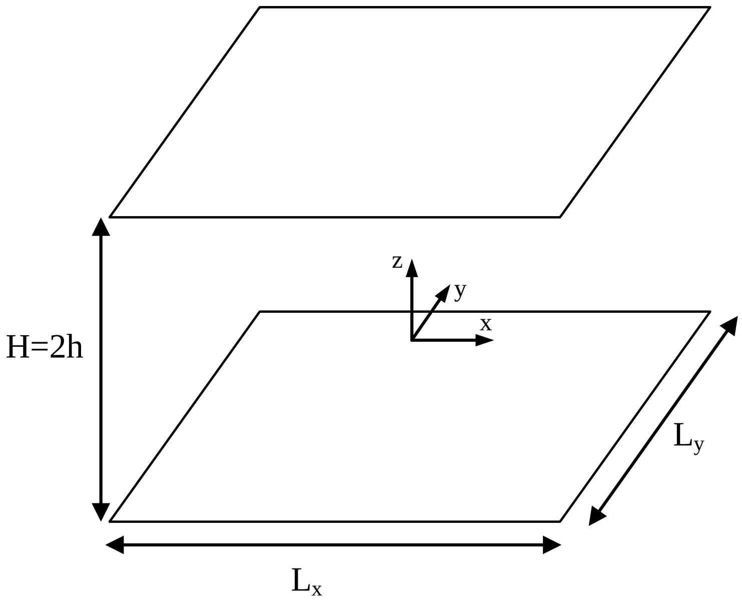

Figure 2.1: Convective box

$$\nabla \cdot \mathbf{u} = 0, \tag{2.1}$$

$$\frac{\partial \mathbf{u}}{\partial t} + (\mathbf{u} \cdot \nabla)\, \mathbf{u} = -\frac{1}{\rho_0} \nabla p - \frac{\rho}{\rho_0} g e_z + \nu \nabla^2 \mathbf{u}, \tag{2.2}$$

$$\frac{\partial T}{\partial t} + (\mathbf{u} \cdot \nabla)\, T = \alpha \nabla^2 T, \tag{2.3}$$

where

$$\mathbf{u} = \left(u_x, u_y, u_z\right) = (u, v, w)\,,$$

$$\rho = \rho_0 \left[1 - \beta (T - T_0)\right]. \tag{2.4}$$

Flow field and temperature can be decomposed into conductive state, i.e. no convective motion, and small perturbation

$$\mathbf{u}\,(\mathbf{x}, t) = 0 + \acute{\mathbf{u}}\,(\mathbf{x}, t)\,, \tag{2.5}$$

$$T\,(\mathbf{x}, t) = T\,(z) + \acute{\theta}\,(\mathbf{x}, t)\,, \tag{2.6}$$

$$p\,(\mathbf{x}, t) = P\,(z) + \acute{p}\,(\mathbf{x}, t)\,. \tag{2.7}$$

where $\mathbf{x} = (x, y, z)$ are the cartesian coordinates, α is the thermal diffusivity, β is the thermal expansion coefficient, ρ is the fluid density and $\mathbf{u}, \theta, p$ are the independent variables respectively.

The heat flux in the conductive state is transferred by the static fluid layer conductively, so (2.2), (2.3) and (2.4) reduce to:

$$0 = -\frac{1}{\rho}\frac{dP}{dz} - g\left[1 - \beta\left(T - T_0\right)\right], \tag{2.8}$$

$$0 = \alpha\frac{d^2T}{dz^2}. \tag{2.9}$$

The conductive temperature distrubution in the fluid layer is then:

$$T(z) - T_0 = \Delta T\left(\frac{1}{2} - \frac{z}{H}\right) = \frac{\Delta T}{2}\left(1 - \frac{z}{h}\right). \tag{2.10}$$

The governing equations for the convective perturbation are obtained by subtracting the equations for the basic conduction state from equations (2.1), (2.2) and (2.3) to obtain

$$\nabla \cdot \acute{\mathbf{u}} = 0, \tag{2.11}$$

$$\frac{\partial \acute{\mathbf{u}}}{\partial t} + \left(\acute{\mathbf{u}} \cdot \nabla\right)\acute{\mathbf{u}} = -\frac{1}{\rho_0}\nabla \acute{p} + \beta g \acute{\theta} e_z + \nu \nabla^2 \acute{\theta}, \tag{2.12}$$

$$\frac{\partial \acute{\theta}}{\partial t} + \left(\acute{\mathbf{u}} \cdot \nabla\right)\acute{\theta} = \acute{\mathbf{u}} \cdot e_z \frac{\Delta T}{2h} + \alpha \nabla^2 \acute{\theta}. \tag{2.13}$$

The advection term $\acute{\mathbf{u}} \cdot e_z \Delta T/2h$ comes from,

$$\left(\acute{\mathbf{u}} \cdot \nabla\right)T = \acute{\mathbf{u}} \cdot e_z\left(\frac{dT}{dz}\right) = -\acute{\mathbf{u}} \cdot e_z\left(\frac{\Delta T}{2h}\right).$$

The no-slip boundary conditions at the upper and lower rigid walls lead to

$$\acute{\mathbf{u}} = \acute{\theta} = 0 \quad \text{at} \quad z = \pm\frac{H}{2}.$$

Under the scaling of the respective physical variables by the thermal diffusion time h^2/α, the fluid layer half-height $H/2$ and temperature difference between the rigid boundaries ΔT, the equations (2.11), (2.12) and (2.13) become:

$$\nabla \cdot \mathbf{u} = 0, \tag{2.14}$$

$$\frac{\partial \mathbf{u}}{\partial t} + \left(\mathbf{u} \cdot \nabla\right)\mathbf{u} = -\nabla p + PrRa_h \theta e_z + Pr\nabla^2 \mathbf{u}, \tag{2.15}$$

$$\frac{\partial \theta}{\partial t} + \left(\mathbf{u} \cdot \nabla\right)\theta = \frac{\mathbf{u} \cdot e_z}{2} + \nabla^2 \theta. \tag{2.16}$$

where

$$Ra_h = \frac{g\beta\Delta T h^3}{\nu\alpha} = \frac{Ra}{8} \quad \text{and} \quad Pr = \frac{\nu}{\alpha}.$$

are Rayleigh (Ra) and Prandtl (Pr) numbers. Ra_h is Rayleigh number based on the half-depth. H is used normally as a length-scale however for computational convenience half-depth $h = H/2$ is used so that normalized z variable varies in $-1 \leq z \leq 1$.

Nusselt number is the ratio between the convective heat flux and total heat flux transported from bottom to top plate. It is calculated at the plate as an average of the slope of temperature profile in the horizontal plane.

$$Nu = \frac{convection + conduction}{conduction} = 1 + \left|\left\langle \frac{\partial\theta}{\partial z} \right\rangle\right|_{wall}.$$

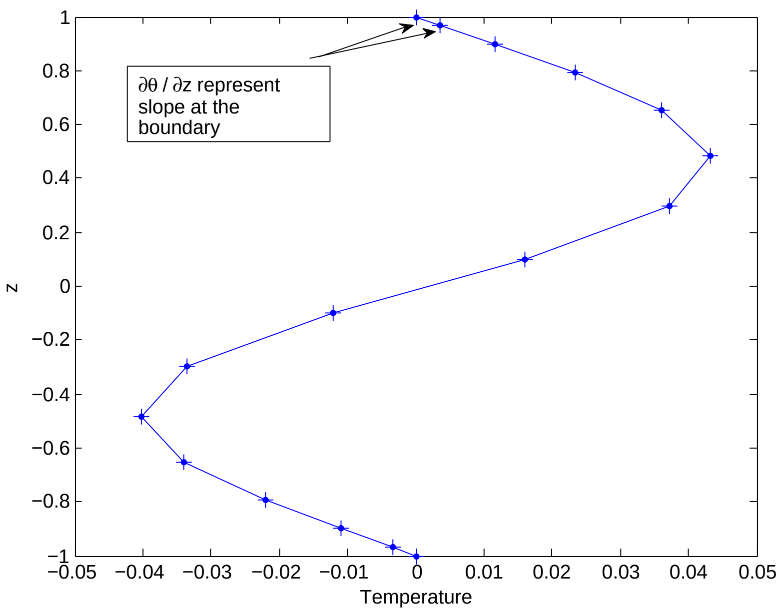

Figure 2.2: Representation of typical temperature profile

2.2 ROTATING RAYLEIGH BÉNARD CONVECTION

An additional force in Rayleigh Bénard convection may be introduced by rotation in the vertical direction normal to the isothermal plates bounding the convective layer. This is the Coriolis force in addition to the forces already acting in the form of viscous and buoyancy forces in Rayleigh Bénard convection. This force mainly depends on the velocity. Centrifugal force is also present in rotating systems, however, it depends on the aspect ratio (width to depth) of the convective box and is neglected in most of the work in literature involving small aspect ratios. Centrifugal force become too small in comparison to gravity induced forces for small aspect ratio containers in comparison to geometries with larger aspect ratio as reported in [69]. This study is restricted to small aspect ratio L/H geometries, thus, the centrifugal forces are ignored and our interest is mainly limited Coriolis force with its effect on convection.

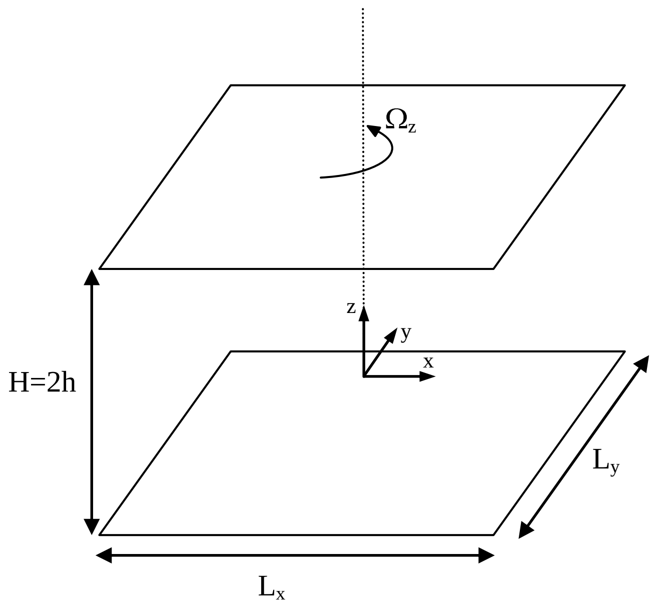

Figure 2.3: Convective box under action of rotation

Coriolis force can be simply added to momentum equation 2.12 as an additional forcing to form the governing equations:

$$\nabla \cdot \mathbf{\acute{u}} = 0, \tag{2.17}$$

$$\frac{\partial \mathbf{\acute{u}}}{\partial t} + (\mathbf{\acute{u}} \cdot \nabla)\, \mathbf{\acute{u}} = -\frac{1}{\rho_0}\nabla \acute{p} + \beta g \acute{\theta} e_z + \nu \nabla^2 \acute{\theta} - 2\Omega_z e_z \times \mathbf{\acute{u}}, \tag{2.18}$$

$$\frac{\partial \acute{\theta}}{\partial t} + (\mathbf{\acute{u}} \cdot \nabla)\, \acute{\theta} = \acute{w}\frac{\Delta T}{2h} + \alpha \nabla^2 \acute{\theta}, \tag{2.19}$$

where $\acute{w}$ is the vertical component of the velocity and Ω_z is the rotation rate about the vertical axis. The no-slip boundary conditons at the upper and lower rigid walls are considered

$$\mathbf{\acute{u}} = \acute{\theta} = 0 \quad \text{at} \quad z = \pm\frac{H}{2}.$$

Under the scaling of the respective physical variables by the thermal diffusion time h^2/α, the fluid layer half-height $H/2$ and temperature difference between the rigid boundaries ΔT, the equations (2.17), (2.18) and (2.19) become:

$$\nabla \cdot \mathbf{u} = 0, \tag{2.20}$$

$$\frac{\partial \mathbf{u}}{\partial t} + (\mathbf{u} \cdot \nabla)\, \mathbf{u} = -\nabla p + PrRa_h \theta e_z + Pr\nabla^2 \mathbf{u} - 2Pr\Omega e_z \times \mathbf{u}, \tag{2.21}$$

$$\frac{\partial \theta}{\partial t} + (\mathbf{u} \cdot \nabla)\, \theta = \frac{w}{2} + \nabla^2 \theta, \tag{2.22}$$

where

$$\Omega = \frac{\Omega_z h^2}{\nu},$$

is the Coriolis parameter in addition to Rayleigh (Ra) and Prandtl (Pr) numbers. The square of the Coriolis parameter is known as Taylor (Ta) number ($Ta = 4\Omega^2$).

CHAPTER 3

KARHUNEN LOÉVE ANALYSIS OF RAYLEIGH-BENARD PROBLEM

3.1 SPECTRAL-ELEMENT FORMULATION

KL analysis is based on an optimal parametrization of the underlying flow field in the energy sense. This is accomplished by representing the flow field in terms of KL basis functions generated using a database characterizing the flow field. For this purpose, a database is generated first by numerically integrating the governing equations (2.14), (2.15), (2.16). Introducing the vorticity $\omega = \nabla \times \mathbf{u}$, the governing equations become:

$$\nabla \cdot \mathbf{u} = 0, \tag{3.1}$$

$$\frac{\partial \mathbf{u}}{\partial t} + \mathbf{u} \times \omega = -\nabla \Pi + PrRa_h \theta e_z + Pr\nabla^2 \mathbf{u}, \tag{3.2}$$

$$\frac{\partial \theta}{\partial t} + (\mathbf{u} \cdot \nabla)\,\theta = \frac{\mathbf{u} \cdot e_z}{2} + \nabla^2 \theta. \tag{3.3}$$

where $\Pi = p + \mathbf{u} \cdot \mathbf{u}/2$ is the stagnation pressure. The numerical technique is based on a spectral-element approach presented in Guessous [19, 20]. It uses Fourier series representation in the horizontal directions while a rescaled Legendre Lagrangian expansion is used in the vertical direction. The formulation is repeated below for completeness.

All spatial variables are discretized by Fourier expansion in horizontal directions:

$$\begin{pmatrix} \mathbf{u} \\ \theta \\ \Pi \end{pmatrix}(x, y, z, t) = \sum_{|m| \le N_x/2} \sum_{|n| \le N_y/2} \begin{pmatrix} \hat{\mathbf{u}} \\ \hat{\theta} \\ \hat{\Pi} \end{pmatrix}(m, n, z, t) \times exp\left(i\left(mk_x x + nk_y y\right)\right). \tag{3.4}$$

Variables are evaluated at the horizontal collocation points which are

$$x_i = \frac{2\pi i}{k_x N_x}, \qquad y_j = \frac{2\pi j}{k_y N_y}.$$

In the vertical direction, the velocity and temperature variables are expanded in terms of scaled Legendre-Lagrange interpolants,

$$\hat{\mathbf{u}}(m,n,z,t) = \sum_{p=0}^{N_z} \bar{\mathbf{u}}(m,n,p,t)\bar{h}_p(z), \tag{3.5}$$

$$\hat{\theta}(m,n,z,t) = \sum_{p=0}^{N_z} \bar{\theta}(m,n,p,t)\bar{h}_p(z), \tag{3.6}$$

while the pressure is expanded in terms of Legendre polynomials [70]

$$\hat{P}(m,n,z,t) = \sum_{p=1}^{N_z-1} \bar{P}(m,n,p,t)L_{p-1}(z). \tag{3.7}$$

Here $\bar{h}_p(z) = h_p(z)/\sqrt{\bar{w}_p}$ with Legendre-Lagrange interpolants

$$h_p(z) = \prod_{\substack{j=0\\ j\neq p}}^{N_z} \frac{\left(z - z_j\right)}{\left(z_p - z_j\right)}.$$

z_p and $\bar{w}_p$ are the Legendre-Gauss-Lobatto grid points and the Gauss-Lobatto quadrature weights, respectively.

After introducing the expansions (3.5, 3.6, 3.7) and projecting (3.4) onto the Fourier space in "x" and "y" and onto appropriate test spaces in "z", the resulting weak form of the equations are integrated in time by a semi-implicit scheme which treats the nonlinear advection terms explicitly using the second-order Adams Bashforth method and the pressure and the diffusion terms using implicit Crank-Nicolson scheme [19, 20].

$$\nabla \cdot \mathbf{u}^{n+1} = 0, \tag{3.8}$$

$$\begin{aligned}\frac{\mathbf{u}^{n+1} - \mathbf{u}^n}{\Delta t} =& \frac{3}{2}\left(\mathbf{u}\times\omega + PrRa_h\theta e_z\right)^n - \frac{1}{2}\left(\mathbf{u}\times\omega + PrRa_h\theta e_z\right)^{n-1} \\ &- \frac{1}{2}\nabla\left(\Pi^{n+1} + \Pi^n\right) + \frac{Pr}{2}\nabla^2\left(\mathbf{u}^{n+1} + \mathbf{u}^n\right),\end{aligned} \tag{3.9}$$

$$\frac{\theta^{n+1} - \theta^n}{\Delta t} = \frac{3}{2}\left(\frac{\mathbf{u}\cdot e_z}{2} - (\mathbf{u}\cdot\nabla)\,\theta\right)^n - \frac{1}{2}\left(\frac{\mathbf{u}\cdot e_z}{2} - (\mathbf{u}\cdot\nabla)\,\theta\right)^{n-1} + \frac{1}{2}\nabla^2\left(\theta^{n+1} + \theta^n\right). \tag{3.10}$$

where $n-1$, n and $n+1$ represent the time iterations and Δt refers to time incrementing between the subsequent iterations. This formulation can be represented in more clear form,

$$\nabla \cdot \mathbf{u}^{n+1} = 0, \tag{3.11}$$

$$\left(Pr\nabla^2 - \frac{2}{\Delta t}\right)\mathbf{u}^{n+1} = \nabla\Pi^{n+1} + \mathbf{g}^n, \tag{3.12}$$

$$\left(\nabla^2 - \frac{2}{\Delta t}\right)\theta^{n+1} = f^n, \tag{3.13}$$

where

$$\mathbf{g}^n = -3\left(\mathbf{u} \times \omega + PrRa_h\theta e_z\right)^n + \left(\mathbf{u} \times \omega + PrRa_h\theta e_z\right)^{n-1} + \nabla\Pi^n - \left(Pr\nabla^2 + \frac{2}{\Delta t}\right)\mathbf{u}^n,$$

$$f^n = -3\left(\frac{\mathbf{u} \cdot e_z}{2} - (\mathbf{u} \cdot \nabla)\,\theta\right)^n + \left(\frac{\mathbf{u} \cdot e_z}{2} - (\mathbf{u} \cdot \nabla)\,\theta\right)^{n-1} - \left(\nabla^2 + \frac{2}{\Delta t}\right)\theta^n.$$

with no-slip and unperturbed boundary conditions are

$$\mathbf{u}^{n+1} = \theta^{n+1} = 0 \text{ and } z = \pm 1.$$

Discritized momentum and energy equations are solved by iteratively in time. An obstacle can be handled because of unknown pressure boundary conditions at the plates by Uzawa method [71].

3.1.1 ALIASING REMOVAL

Poor spatial resolution introduces inaccuracies in the numerical representation of the dynamics of the flow. As the forcing parameter Rayleigh number increases, so does the resolution requirement of the representation. This, in turn, increases the cost of the computation. In the collocation approach, inadequate resolution causes aliasing error. Aliasing error occurs when evaluating the nonlinear terms where product of the variables in truncated representations with inadequate resolution is involved. 3/2 rule is used for removing this handicap [72]. Consider the product of the functions, for example,

$$a_k(x) = \sum_{k=-K}^{K} \hat{a}_k \; exp(ikx) \qquad \text{and} \qquad b_k(x) = \sum_{k=-K}^{K} \hat{b}_k \; exp(ikx).$$

that gives

$$c(x_j) = \sum_{k=-K}^{K} \hat{c}_k \, exp(ikx_j) = a(x_j)b(x_j).$$

where $K = N/2$. Then, the product in the Fourier space is contaminated by aliased convolution sum

$$\tilde{c}_k = \underbrace{\sum_{\binom{p,q=-K}{p+q=k}}^{K} \hat{a}_p \, \hat{b}_q}_{\hat{c}_k} + \underbrace{\sum_{\binom{p,q=-K}{p+q=k+N}}^{K} \hat{a}_p \, \hat{b}_q + \sum_{\binom{p,q=-K}{p+q=k-N}}^{K} \hat{a}_p \, \hat{b}_q}_{\text{aliasing term}} .$$

The classical 3/2 rule of filtering the aliasing error involves the product to be evaluated in the mesh size (resolution) expanded as much as 3/2 times the original mesh size. The aliasing removal is used when the resolution requirements of the flow are high at regimes with high Rayleigh number.

3.2 KL FORMULATION

The KL method is a statistical procedure to analyze the physical phenomena from numerically and experimentally generated database. The procedure is used to generate an emprical basis (KL basis) in terms of which the database can be parametrized optimally in the energy norm (see Appendix A for details). The resulting subspace spanned by the KL basis can also be used to reduce the governing equations into a low dimensional form using Galerkin projection. The elements of the basis set are the eigenfunctions of the integral equation A.12 and the corresponding eigenvalues give the energy of the corresponding modes. The kernel of that equation obtained from DNS solution in §3.1. The addition of symmetries expands the existing database and in turn produce sharper basis carrying the character of the flow. In this thesis, the numerical database consists of three dimensional velocity and temperature fields $v_i^n(x_1, x_2, x_3)$ where v_i denotes the flow vector, n denotes the snapshots (samples) in time, i $(= 1, 2, 3)$ denotes the velocity vector and $(= 4)$ temperature, and $\mathbf{x} = (x_1, x_2, x_3)$ or interchangibly $\mathbf{x} = (x, y, z)$ denote the spatial directions. This set of

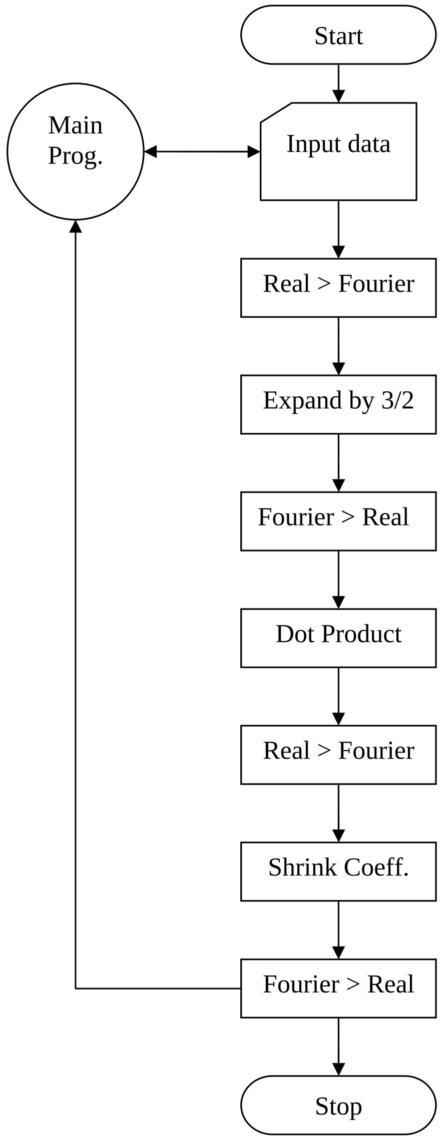

Figure 3.1: Flowchart of the 3/2 rule based on FFT

KL modes may be paired in such a way to provide a convenient parametric representation of the flow database in the terms of real and physical *flowlets* $\mathbf{v}^k$,

$$\mathbf{v}(\mathbf{x},t) = \sum_k \mathbf{v}^k = \sum_k \left[a_k(t)\boldsymbol{\Psi}^k(\mathbf{x}) + a_{k^*}(t)\boldsymbol{\Psi}^{k^*}(\mathbf{x})\right]. \tag{3.14}$$

where the summation index k runs through the conjugate pairs of the KL modes $\{k, k^*\}$ defined by

$$k = (m, n, q) \qquad \text{and} \qquad k^* = (-m, -n, q), \tag{3.15}$$

where

$$\boldsymbol{\Psi}^{k^*} = \left(\boldsymbol{\Psi}^k\right)^* \qquad \text{and} \qquad a_{k^*} = a_k^*. \tag{3.16}$$

Here, $(^*)$ represents the complex conjugate. Translational invariance of the flow in the horizontal directions implies that the eigenfunctions are in the form

$$\boldsymbol{\Psi}^k(\mathbf{x}) \equiv \boldsymbol{\Psi}(m, n, q; \mathbf{x}) = \boldsymbol{\Phi}^k(z)exp(2\pi i(mx/s_x + ny/s_y)). \tag{3.17}$$

In addition, there are some rotational symmetries satisfied by the solution to the governing PDE in the periodic box. When the box is assumed to have square planform, there are added rotational symmetries that are considered in Table 3.1.

Table 3.1: Rotational symmetries and their actions

	Symmetry group element	Its action
Identity	I	$\{u, v, w, \theta, x, y, z\}$
Rotation 90°	R	$\{-v, u, w, \theta, -y, x, z\}$
Rotation 180°	R^2	$\{-u, -v, w, \theta, -x, -y, z\}$
Rotation 270°	R^3	$\{v, -u, w, \theta, y, -x, z\}$
Reflection in x	F	$\{-u, v, w, \theta, -x, y, z\}$
Diagonal Flip	FR	$\{v, u, w, \theta, y, x, z\}$
Reflection in y	FR^2	$\{u, -v, w, \theta, x, -y, z\}$
Diagonal Flip	FR^3	$\{-v, -u, w, \theta, -y, -x, z\}$
Vertical Flip	Z	$\{u, v, -w, -\theta, x, y, -z\}$

Since flow generated by these symmetries are possible solutions to the governing PDEs, a generated flow database can be expanded 16-fold by the action of these symmetries

$$\left\{I, R, R^2, R^3, F, FR, FR^2, FR^3\right\} \times \{I, Z\},$$

resulting in sharper KL bases when the expanded database is used in the construction of the bases. As a consequence, the KL bases come as families of modes with maximum number of members (degeneracy) 8, for example,

$$\{\mathbf{\Psi}(0, 1, q; \mathbf{x}), \mathbf{\Psi}(1, 0, q; \mathbf{x}), \mathbf{\Psi}(-1, 0, q; \mathbf{x}), \mathbf{\Psi}(0, -1, q; \mathbf{x})\},$$

and with odd-even parity in the vertical variable z. The governing equations (3.1, 3.2, 3.3) are numerically integrated using the numerical scheme described in §3.1 for various parameter values in different regimes. The resulting flow database $\mathbf{v} = [u, v, w, \theta]\,(\mathbf{x}, t)$ is symmetrically expanded before generating the KL bases $\Phi_j(m, n, q; z)$, $j = 1, ..., 4$ and these bases are in turn used to parametrize the database to study the underlying dynamics of the flow in different regimes and for different parameter values.

3.3 KL ANALYSIS

Different Prandtl regions, namely $Pr < 1, Pr \approx 1, Pr > 1$, and different transition regimes, steady to weakly turbulent, are investigated. For this purpose, in the steady regime, three Pr cases are considered. The resulting Nusselt number (Nu) values are calculated at the wall and compared with Clever and Busse [1] in Table 3.2. The energy distribution amongst KL modes are compared in Table 3.3 for the steady regime.

Table 3.2: Comparison of Nusselt number for different Rayleigh numbers

Ra	2000			50000	
Pr	7	0.71	0.025	7	0.71
Nu	1.2129	1.2105	1.0614	3.864	4.245
Nu[1]	1.214	1.212	1.0610	3.894	3.9587

It can be seen that the first KL mode dominates in the energy content in all cases. This is an indication of the efficient parametrization of the flow database by KL representation. In the storage or reconstruction of the flow field only a few KL modes need to be considered. Further, the drop in the energy content towards less energetic KL modes sharpens as Pr increases. Thus the flow at low Pr contains more structure to be resolved and so it takes more KL modes to resolve it. This can clearly be seen in Figures 3.2, 3.3, 3.4.

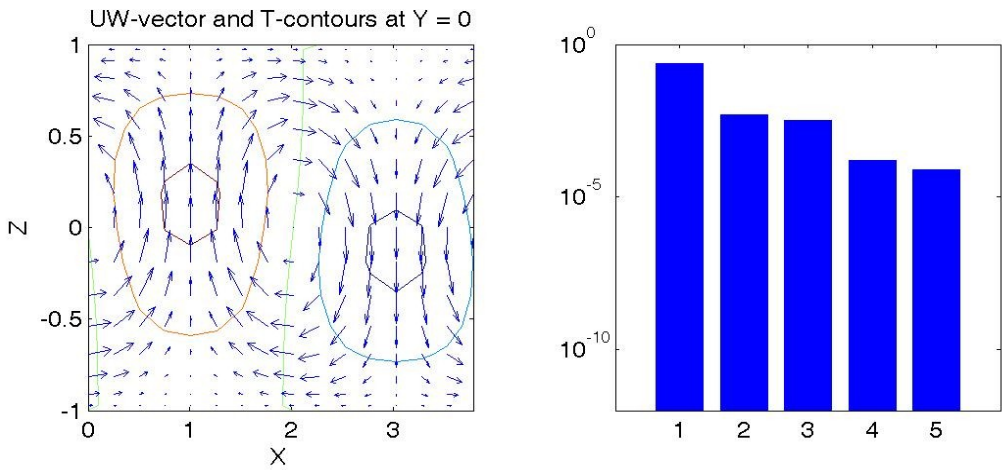

Figure 3.2: Convective rolls and KL energy spectrum for steady regime for Pr=0.025, at 16x16x16 resolution

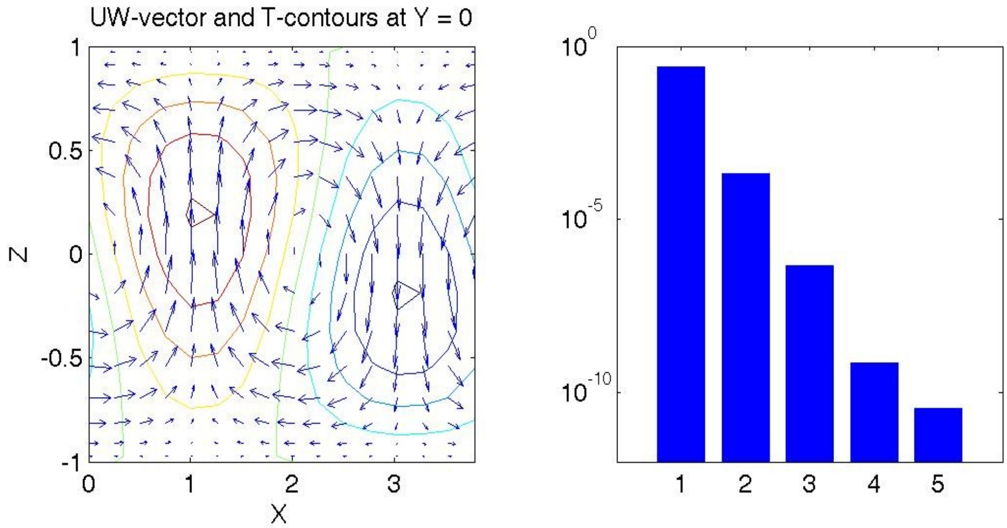

Figure 3.3: Convective rolls and KL energy spectrum for steady regime for Pr=0.71, at 16x16x16 resolution

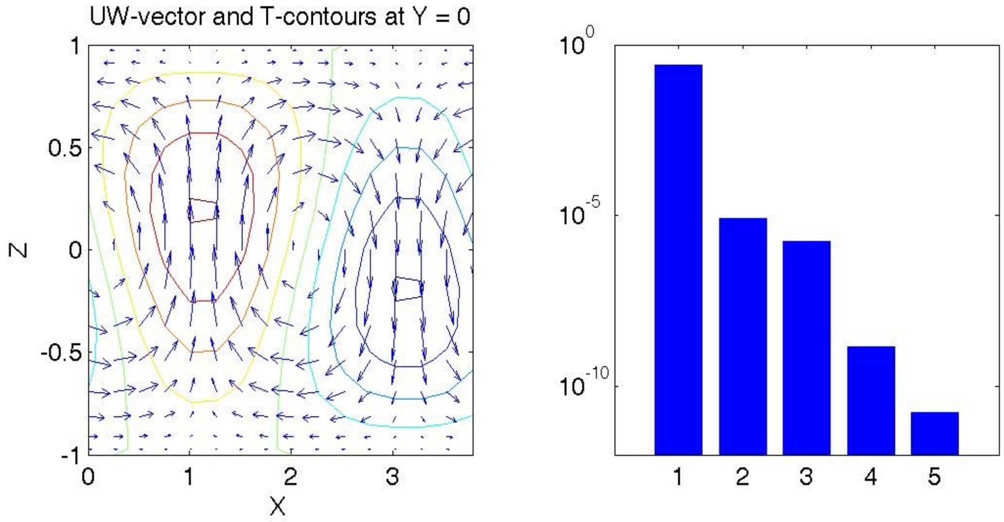

Figure 3.4: Convective rolls and KL energy spectrum for steady regime for Pr=7, at 16x16x16 resolution

Table 3.3: KL energy distribution in steady roll regime (Ra=2000)

	$Pr = 0.025$		$Pr = 0.71$		$Pr = 7$	
	mnq	λ	mnq	λ	mnq	λ
1	101	8.82e+1	101	3.5e+2	101	3.56e+2
2	301	1.84e+0	201	2.84e-1	201	1.17e-2
3	201	1.15e+0	301	6.5e-4	301	2.53e-3
4	501	5.90e-2	401	9.71e-7	401	2.12e-6
5	401	2.79e-2	501	4.94e-8	501	2.48e-8

The vertical profiles $\Phi_j(m, n, q; z)$ of the two most energetic KL modes for three Pr numbers are shown in Figure 3.5. The first mode $m = 1, n = 0, q = 1$, being the main mode present when convection sets in, shows almost no variation with Pr. This corresponds to the fact that the point when convection just sets in is independent of Pr. The mode $m = 2, n = 0, q = 1$, on the other hand, show some variation with Pr. This variation manifests itself in the thickness of the boundary layer which gets thinner as Pr is reduced as expected, as well as, in the dominance of the mechanical components relative to the thermal component of the mode for small Pr. The thinning of the boundary layer leaves a relatively wide area in the core region in which the $\Phi_1(2, 0, 1; z)$ profile is flat. These features of the KL basis may be considered in a future effort to develop a KL based model of the phenomena.

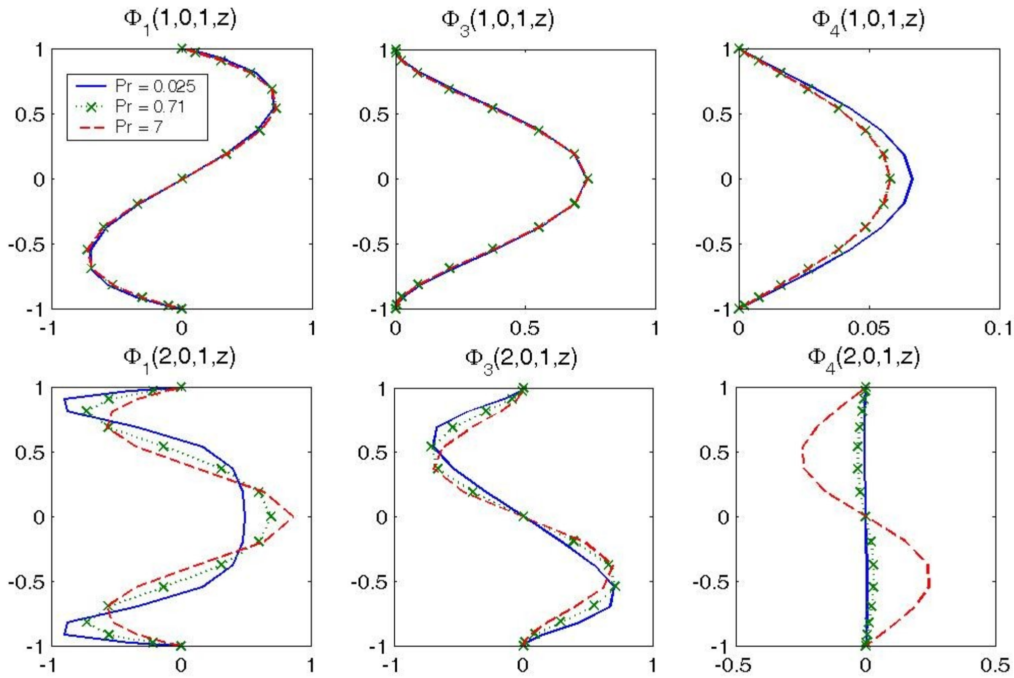

Figure 3.5: Vertical profiles of most energetic first two mode for three different Pr numbers, 0.025, 0.71, 7

In another numerical experiment, the periodic regime is explored. The corresponding energy distribution among the first five KL modes are shown in Table 3.4. The regime is characterized by traveling waves moving along the rolls as shown in Figure 3.6. The traveling waves are in the form superimposed onto the earlier roll motion as it is evident in the time evolution of the modal coefficients $a(m, n, q; t)$ in Figure 3.7 corresponding to the first four modes in Table 3.4.

It is shown in Figure 3.7, the coefficient $a(1, 0, 1; t)$ shows no time variation while $a(1, 1, 1; t)$ and $a(1, 1, 2; t)$ are periodically varying in time and only in phase. The phase differences in $a(1, \mp 1, 1; t)$ and $a(1, \mp 1, 2; t)$ are facilitating the traveling of the wave along the roll direction.

Table 3.4: KL energy distribution in periodic regime (Ra=15000), 24x24x24 resolution

	$Pr = 0.71$	
	mnq	λ
1	101	6.44e+1
2	111	9.43e+0
3	102	4.67e+0
4	112	2.73e+0
5	211	4.62e-1

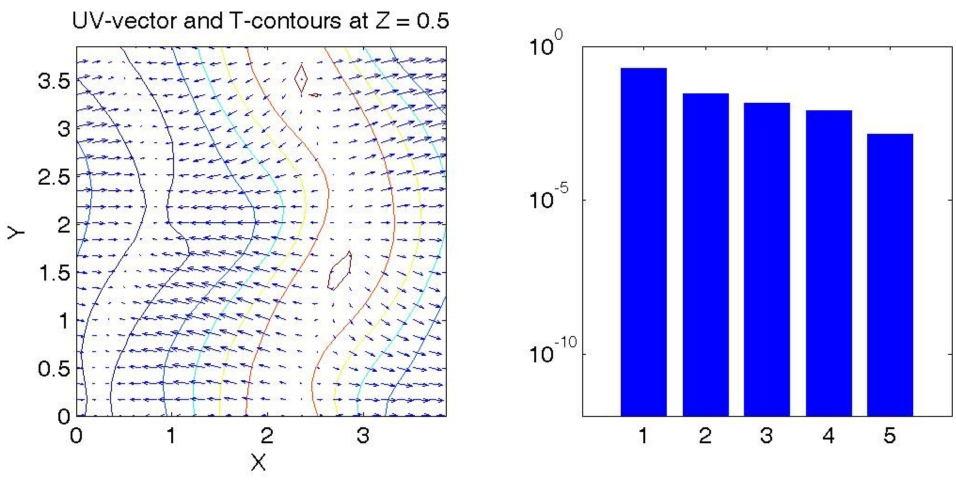

Figure 3.6: Perodic regime and its KL energy spectrum. The KL modes in the spectrum are labeled as in Table 3.4

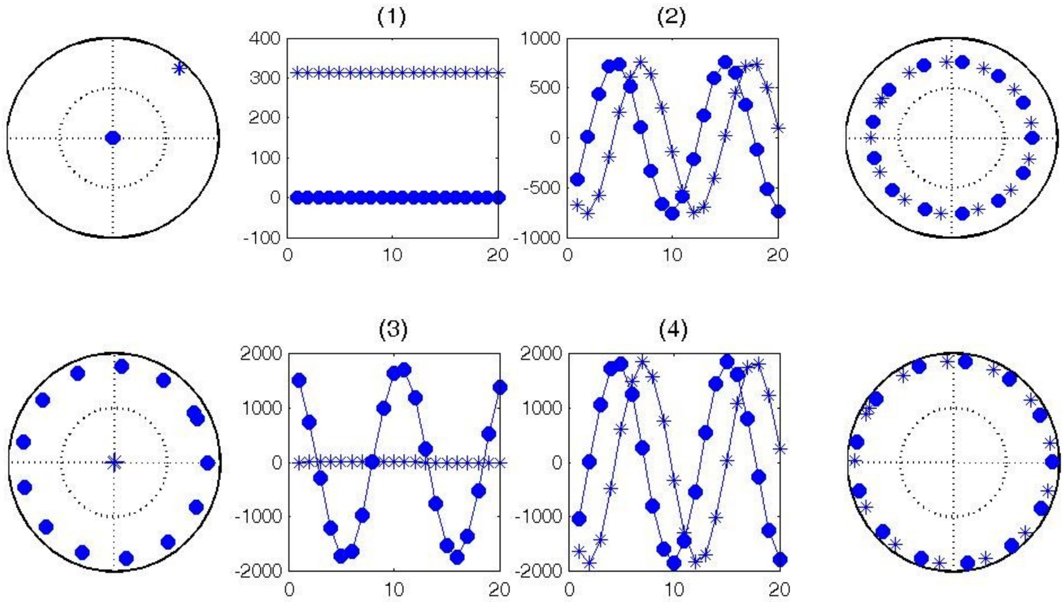

Figure 3.7: Time evolution and polar decomposition of the complex modal coefficients corresponding to (1) (1,0,1) (star) and (0,1,1) (circle), (2) (1,1,1) (star) and (1,-1,1) (circle), (3) (1,0,2) (star) and (0,1,2) (circle), (4) (1,1,2) (star) and (1,-1,2) (circle)

The appearance of the third KL mode is interesting in that it has all its components vanishing except the v-component (see Figure 3.8) and that this mode is the first energetic mode with nonvanishing vertical vorticity component (see Figure 3.9). This points to two important character of the underlying dynamics of this regime. First, the apperance of the oscillatory instability is shown to be associated with the appearance of the vertical vorticity component [23]. Second, due to vanishing w-component, this mode does not contribute to energy production, which is related to $\langle wT \rangle$, thus it is parasitic. When activeted, the parasitic nature of this mode caused a drop in the heat transfer rate which is observed as the first kink in the Nu versus Ra curve in the literature [73]. Thus in order to effect heat transfer efficiency, this mode is to be controled [57].

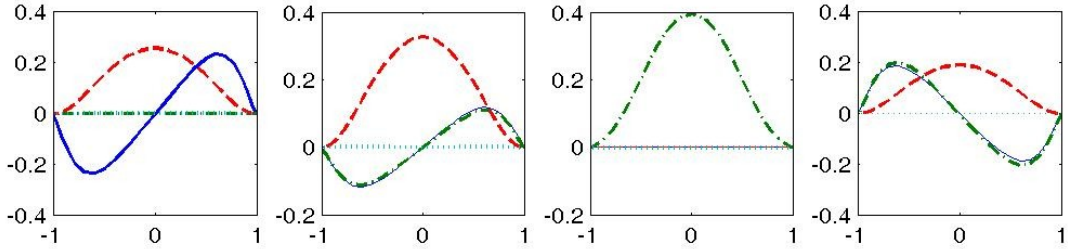

Figure 3.8: The vertical profiles of the first four KL modes as labeled in Table 3.4. Here, u-, v-, w-, and T-components of each KL eigenvector are denoted by solid, dash-dotted, dashed and dotted lines, respectively

A revealing characterization of the modes can be achieved by the following representation of the divergence-free velocity field

$$\mathbf{u} = \delta v + \varepsilon\eta, \tag{3.18}$$

where the operators δ and ε are defined by

$$\delta v \equiv \nabla \times (\nabla \times v e_z), \qquad \varepsilon\eta \equiv \nabla \times e_z. \tag{3.19}$$

In this representation, the mechanical components $\mathbf{u}^k$ of the KL eigenfunctions $\mathbf{\Psi}^k = \left\{\mathbf{u}^k, \theta^k\right\}$ take the form of

$$\mathbf{u}^k(\mathbf{x}) = \delta v^k(\mathbf{x}) + \varepsilon\eta^k(\mathbf{x}), \tag{3.20}$$

where

$$v^k(\mathbf{x}) = v^k(z)exp(2\pi imx/s_x + 2\pi iny/s_y), \quad \eta^k(\mathbf{x}) = \eta^k(z)exp(2\pi imx/s_x + 2\pi iny/s_y), \tag{3.21}$$

in which

$$v^k(z) = \frac{\Phi_3^k(z)}{\left(\frac{2\pi}{s_x}\right)^2(m^2+n^2)}, \quad \eta^k(z) = \frac{\left(\nabla \times \mathbf{u}^k\right)_3(z)}{.}\left(\frac{2\pi}{s_y}\right)^2(m^2+n^2) \tag{3.22}$$

The functions $v^k(z)$ and $\eta^k(z)$ are associated with the vertical velocity and the vertical vorticity components, respectively, and plotted in Figure. 3.9

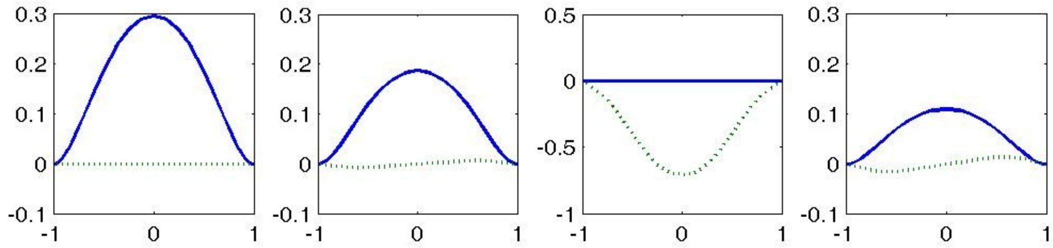

Figure 3.9: The vertical profiles of $v^k(z)$ (solid line) and $\eta^k(z)$ (dotted line) corresponding to the first four KL modes as labeled in Table 3.4

The double periodic regime is investigated for low and high Prandtl regions, as well. In this regime, two concurrent periodic motions are present. The one with larger period contains more energy. This represents the traveling wave motion observed earlier. Smaller period is caused by the thermals released from the thermal boundary layers [56]. It is seen from Figure 3.10 and Figure 3.11 Nusselt number variation and energy variation of the first (convective) mode are same for low Prandtl number fluid. The same result can be observed for the high Prandtl number fluid (see Figure 3.13 and 3.14).

Table 3.5: KL energy distribution in double periodic regime (Ra=3700)

	$Pr = 0.025$	
	mnq	λ
1	111	0.2410
2	011	0.1958
3	012	0.1745
4	013	0.1744
5	112	0.0695
6	121	0.0309
7	031	0.0142
8	131	0.0099
9	021	0.0098
10	014	0.0068

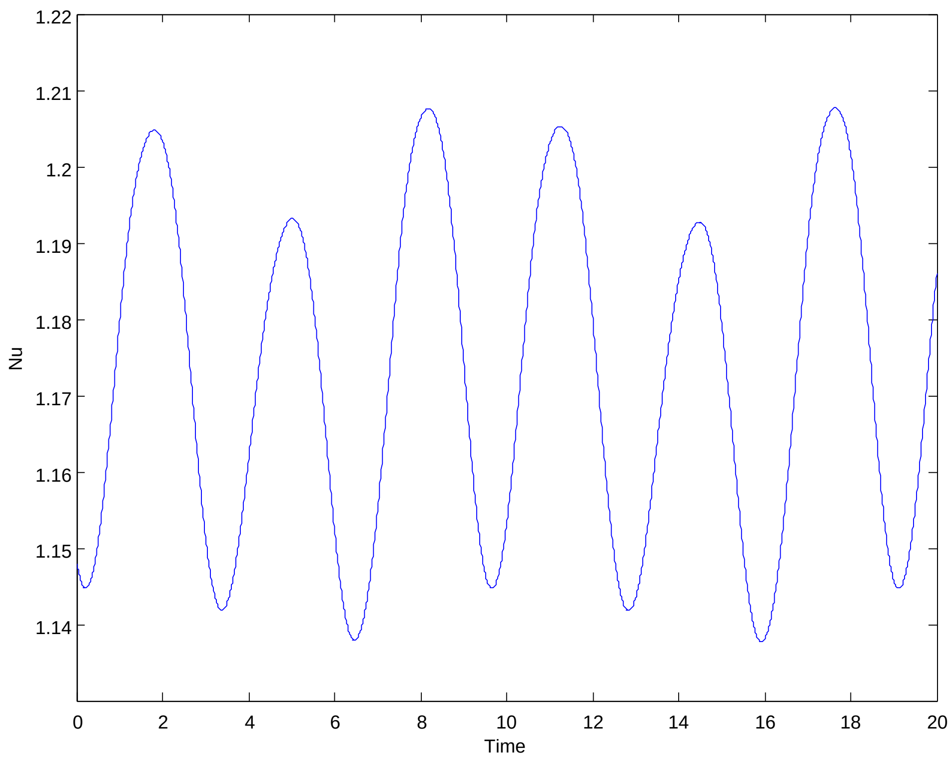

Figure 3.10: Nusselt number variation with time for Pr=0.025, Ra=3700, at 24x24x24 resolution

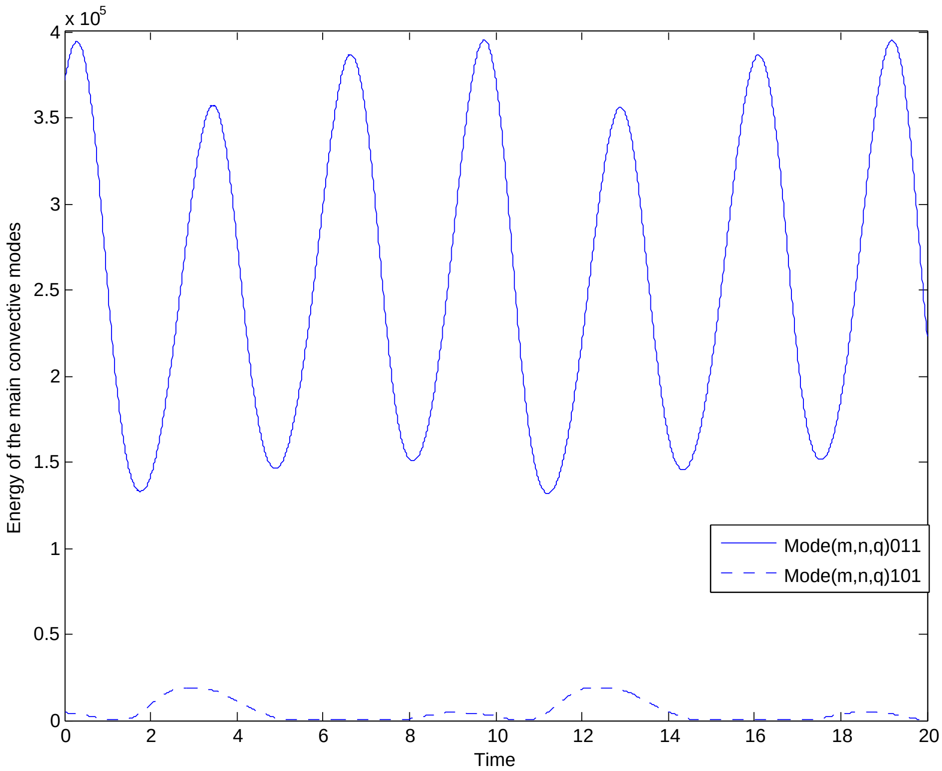

Figure 3.11: Main convective energy of the most energetic horizontal modes for Pr=0.025, Ra=3700, at 24x24x24 resolution

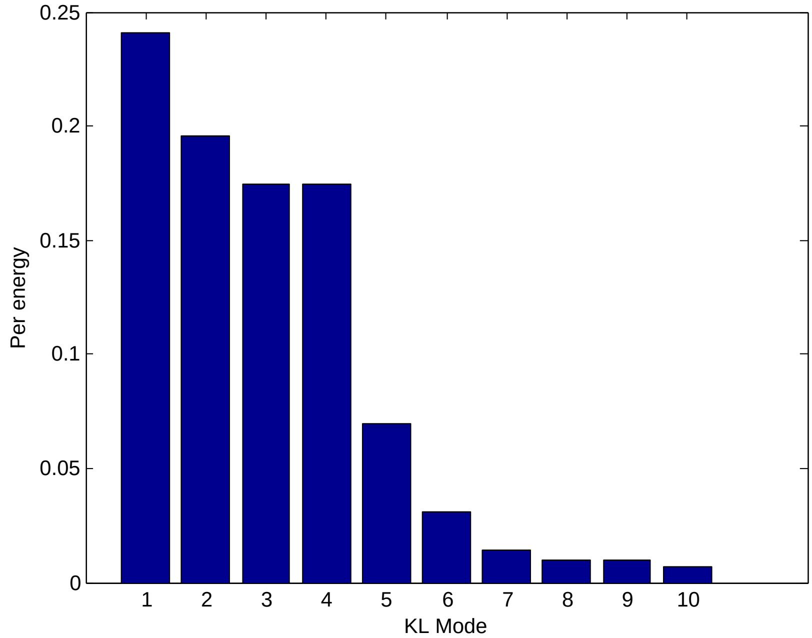

Figure 3.12: Most energetic 10 KL modes of double periodic regime for Pr=0.025, Ra=3700, at 24x24x24 resolution

Table 3.6: KL energy distribution in double periodic regime (Ra=70000)

	$Pr = 7$	
	mnq	λ
1	011	0.4560
2	012	0.3892
3	021	0.0496
4	031	0.0404
5	013	0.0188
6	022	0.0140
7	032	0.0048
8	014	0.0040
9	051	0.0039
10	111	0.0033

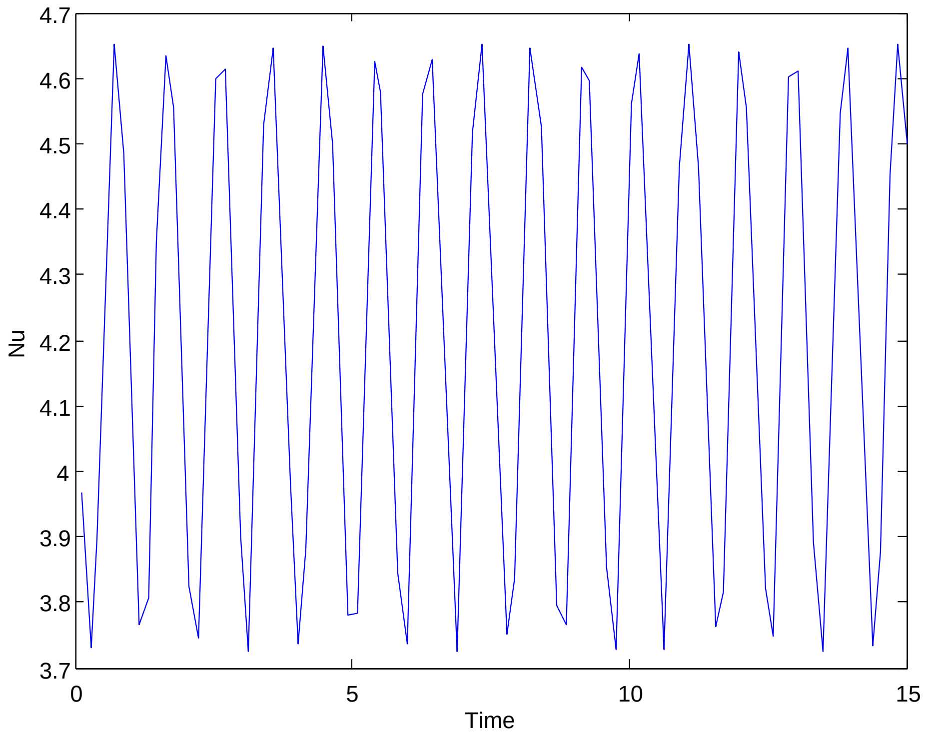

Figure 3.13: Nusselt number variation with time for double periodic regime, Pr=7, Ra=70000, at 32x32x32 resolution

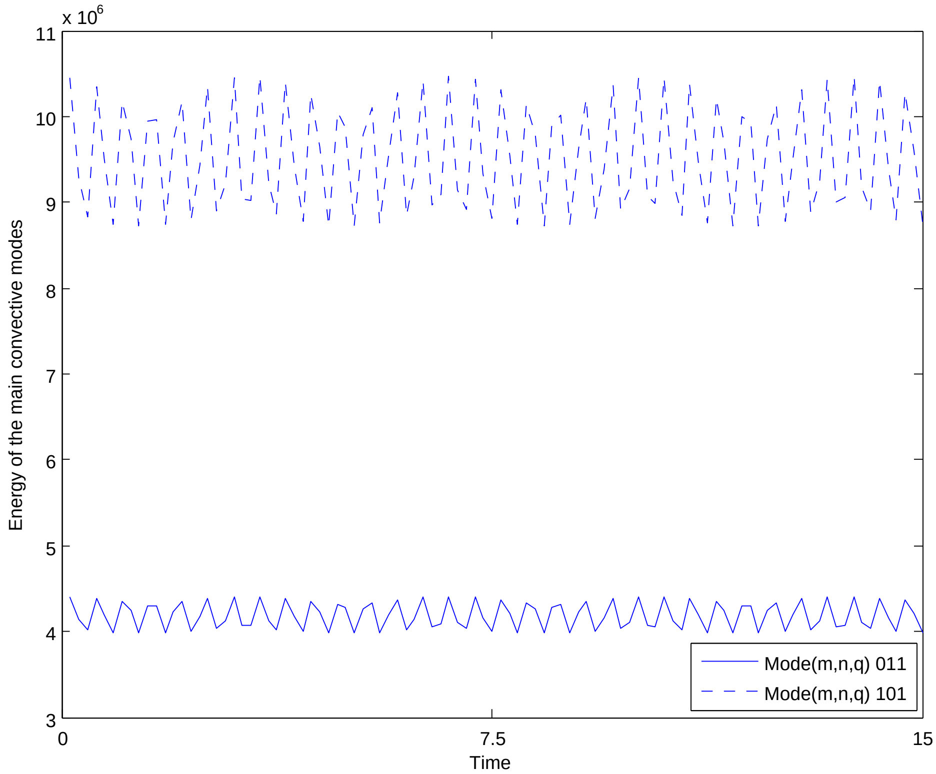

Figure 3.14: Main convective energy of the most energetic horizontal modes for double periodic regime, Pr=7, Ra=70000, at 32x32x32 resolution

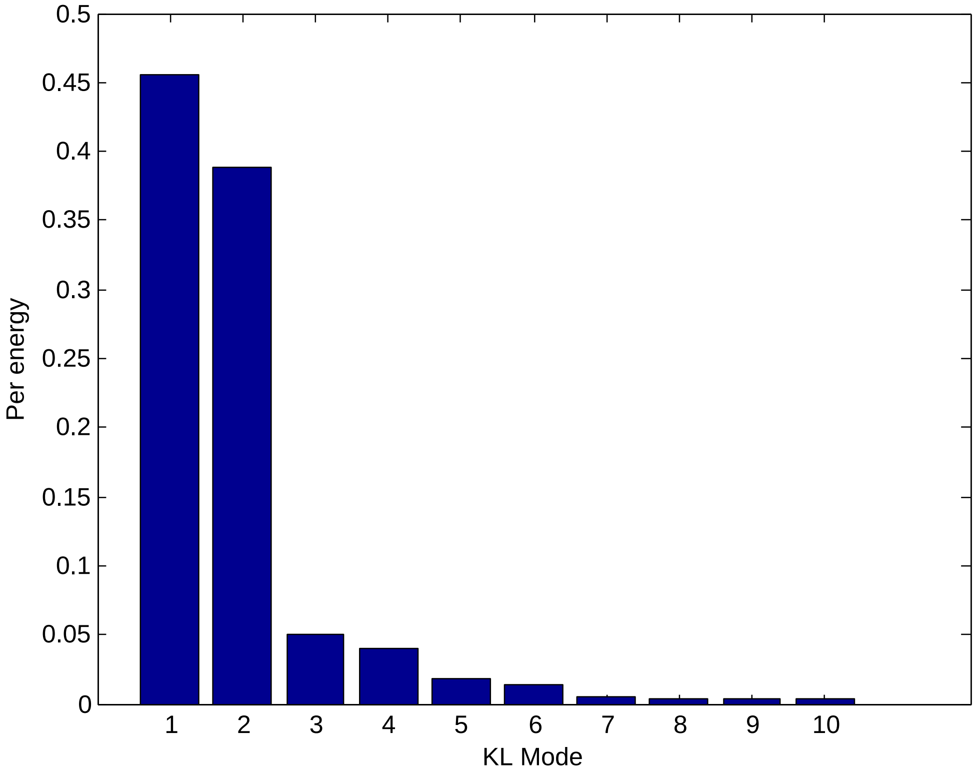

Figure 3.15: Most energetic 10 KL modes of double periodic regime for Pr=7, Ra=70000, at 32x32x32 resolution

Weakly turbulent regime is also explored. KL energy distributions in weakly turbulent regime for two different Prandtl numbers are indicated at the Table 3.7.

Table 3.7: KL energy distribution in weakly turbulent regime, 32x32x32 resolution

	Pr = 0.025		Pr = 7	
	mnq	λ	mnq	λ
1	011	0.2588	011	0.4240
2	111	0.2076	012	0.3512
3	012	0.1292	021	0.0444
4	013	0.1048	031	0.0248
5	112	0.0648	013	0.0244
6	121	0.0328	111	0.0172
7	122	0.0160	121	0.0144
8	031	0.0100	022	0.0124
9	113	0.0088	112	0.0088
10	022	0.0084	014	0.0052

It is shown in the Figures 3.16 and 3.17 that convection is mainly governed by the first two modes for the high Prandtl flow while many more modes are involved in the representation of the dynamics in the low Prandtl case. A specific feature in this regime is that there is an energy exchange between rolls in x- and y-directions occuring at random times as shown in Figure 3.18 and Figure 3.19. In the previous regimes, the rolls aligned in parallel rows in one direction. This exchange of energy is much more rapid and random for the lower Prandtl value case. This is expected due to the more active dynamics in this case as observed earlier. It can be seen that many more harmonic structures are involved in the reconstruction of the flow for a given target energy resolution in the case of low Prandtl number in comparison to the larger Prandtl number case in the Figure 3.20 .

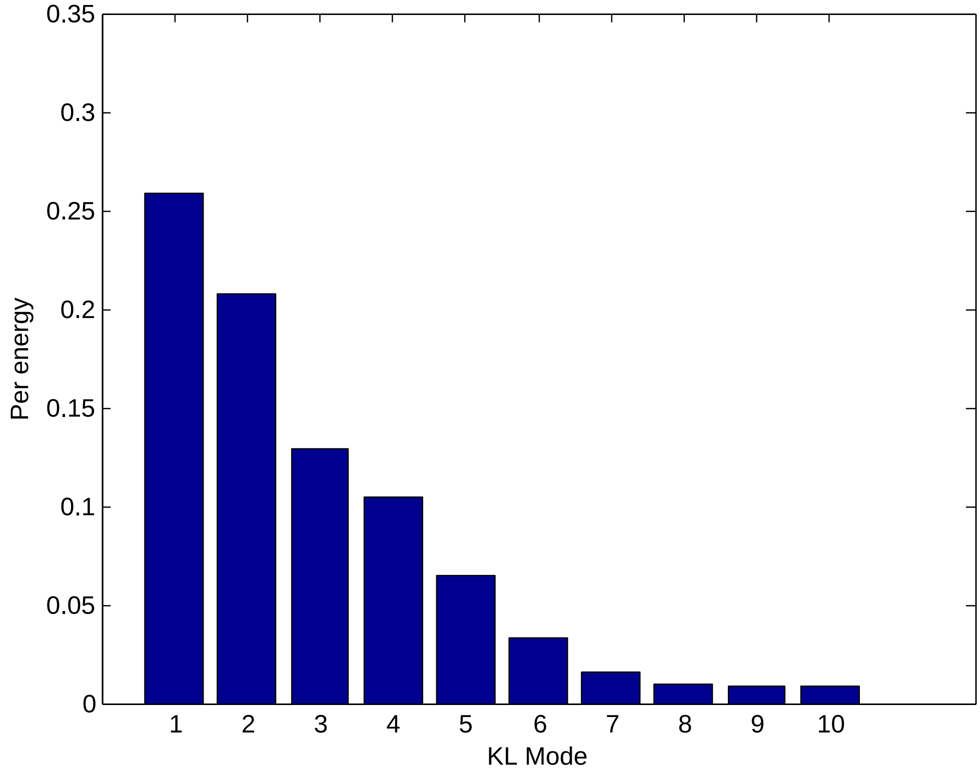

Figure 3.16: Most energetic 10 KL modes for weakly turbulent regime at Pr=0.025, Ra=6000, at 32x32x32 resolution

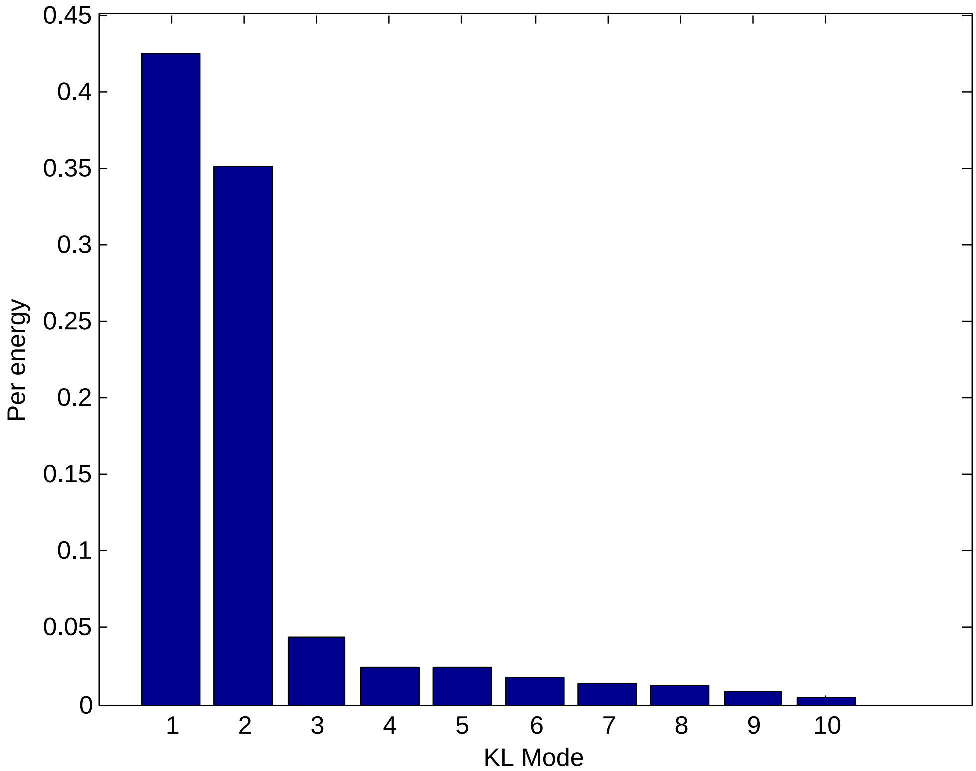

Figure 3.17: Most energetic 10 KL modes for weakly turbulent regime at Pr=7, Ra=140000, at 32x32x32 resolution

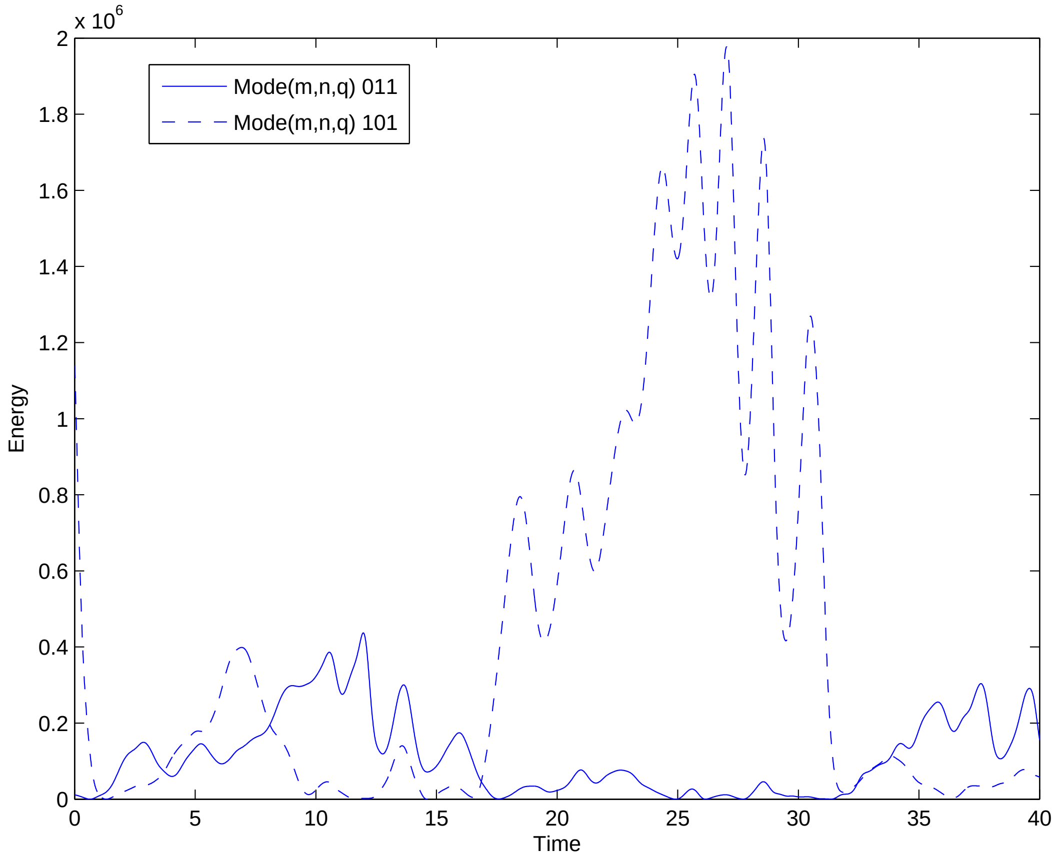

Figure 3.18: Main convective energy of the most energetic horizontal modes for weakly turbulent regime for Pr=0.025, Ra=6000, at 32x32x32 resolution

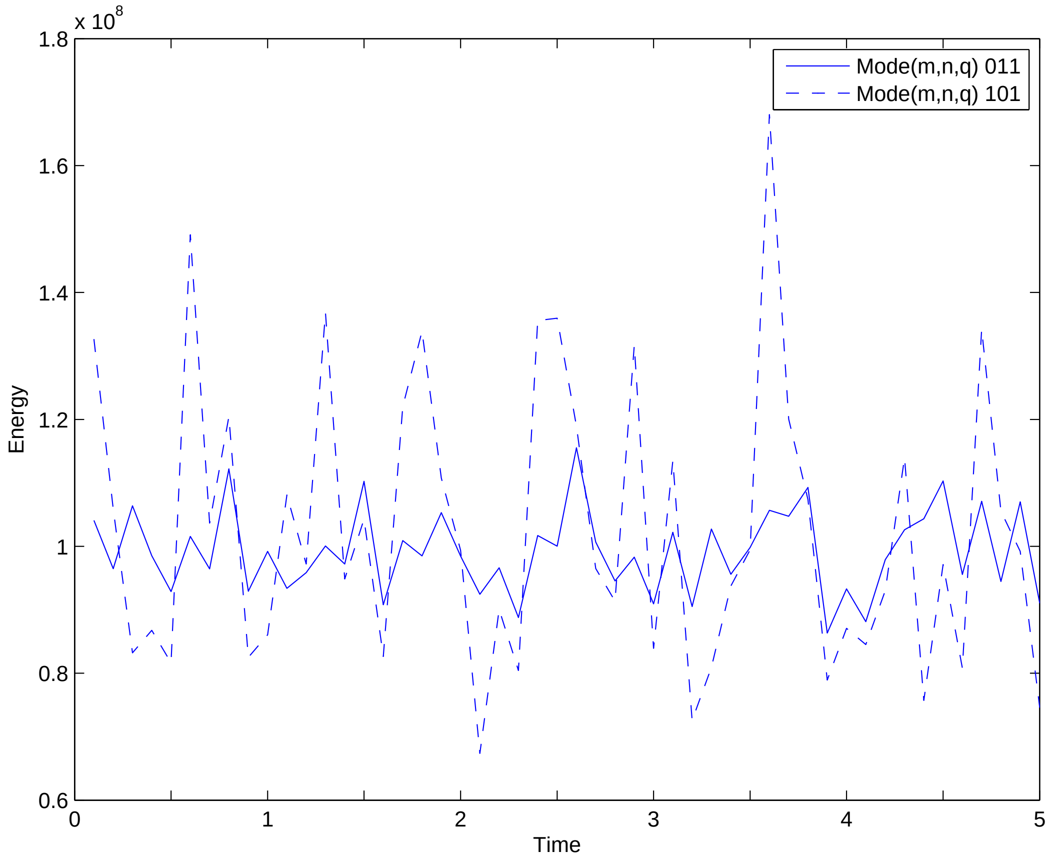

Figure 3.19: Main convective energy of the most energetic horizontal modes for weakly turbulent regime for Pr=7, Ra=140000, at 32x32x32 resolution

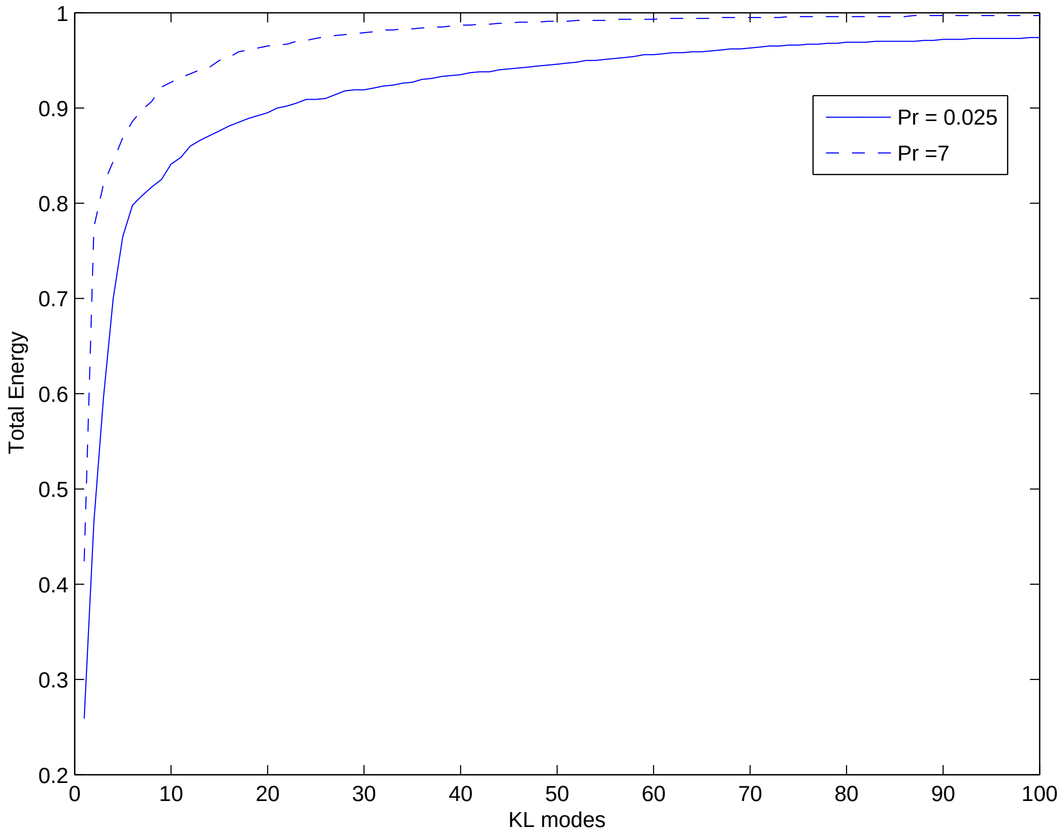

Figure 3.20: Energy contribution of the modes for weakly turbulent regime

When various regimes, i.e periodic, double periodic and weakly turbulent, are compared for fixed Prandtl (see Figure 3.21), it is observed that the first two modes are dominant in the periodic regime. There is a sharp decrease in the energy content after the second mode. First and second modes contain almost all of the energy. On the other hand there is no sharp decrease in the energy content for double periodic and weakly turbulent regimes due to complexity of the flow. It also shows the reliability of the KL parameterization.

The above considerations constitute a static use of KL bases in the sense that they are used to extract useful and hidden information in a simulation database representing the flow dynamics. However, KL bases can also be used to construct a suitable space onto which the governing PDE can be Galerkin projected to obtain a system of ODEs which provide a low dimensional representation of the evolution of the flow dynamics in energy optimal sense. Since KL bases are generated from a database representing the flow dynamics at some reference values of the flow parameters, the optimal representation is only possible within a neighborhood of these reference values. Furthermore, the divergence-free nature of the KL bases is only limited to the extent that it is satisfied by the flow database. As it is true for the most incompressible flow solving strategies, the present numerical technique can only provide a certain degree of resolution to divergence-free constraints. This carries over to the generated KL bases and gets worse towards relatively less energetic modes in the bases hierarchy. Thus, as an alternative, we set out to use parameter independent analytic solenoidal bases to explore the time evolution of the flow dynamics in a sector of the parameter space in the next chapters.

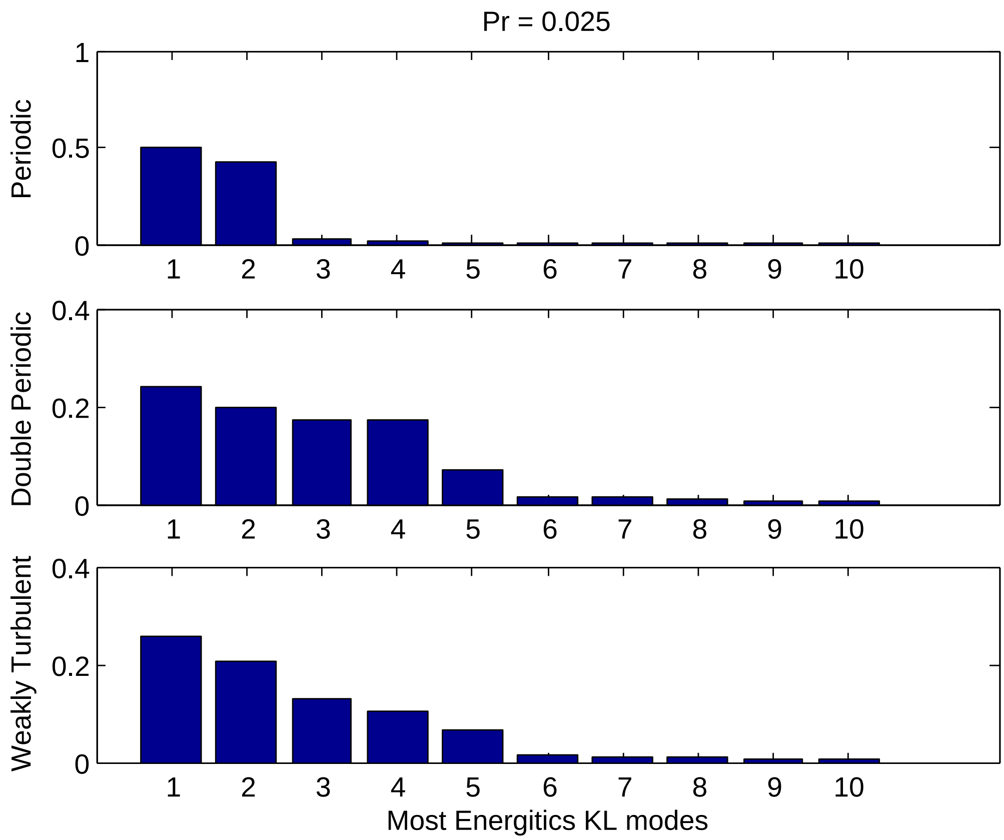

Figure 3.21: Comparison of most energetic 10 KL modes for different regimes, Pr=0.025, Ra=2000 (Periodic), Ra=3700 (Double periodic), Ra=6000 (Weakly turbulent)

CHAPTER 4

SOLENOIDAL BASIS

The flow takes place in a doubly periodic 3D rectangular box of aspect ratio $S_x/2 \times S_y/2 \times 1$, (see Figure 2.1) where $0 \le x \le L_x/h = S_x$, $0 \le x \le L_y/h = S_y$ and $-1 \le z \le 1$. L_x and L_y are the dimensional lenghts at the rectangular region in the horizontal "x" and "y" directions, respectively. Let $\xi = 2\pi/S_x$ and $\eta = 2\pi/S_y$ be the corresponding fundamental wavenumbers, then periodicity with periods $S_x = 2\pi/\xi$ and $S_y = 2\pi/\eta$ implies that:

$$\mathbf{u}\left(x + \frac{2\pi m}{\xi}, y + \frac{2\pi n}{\eta}, z, t\right) = \mathbf{u}\left(x, y, z, t\right),$$
$$\theta\left(x + \frac{2\pi m}{\xi}, y + \frac{2\pi n}{\eta}, z, t\right) = \theta\left(x, y, z, t\right),$$

for all integers m and n. This allows to use Fourier expansion in x and y directions:

$$\mathbf{u} = \sum_{|m| \le N_x/2} \sum_{|n| \le N_y/2} \hat{\mathbf{u}}\left(m, n, z, t\right) exp\left[i\left(k_x x + k_y y\right)\right], \tag{4.1}$$

$$\theta = \sum_{|m| \le N_x/2} \sum_{|n| \le N_y/2} \hat{\theta}\left(m, n, z, t\right) exp\left[i\left(k_x x + k_y y\right)\right], \tag{4.2}$$

where $k_x = 2\pi m/S_x$ and $k_y = 2\pi n/S_y$. The horizontal directions are discretized by $x_i = S_x i/N_x = 2\pi i/\xi N_x$, $y_j = S_y j/N_y = 2\pi j/\eta N_y$ for $0 \le i \le N_x$ and $0 \le j \le N_y$.

4.1 CONSTRUCTION OF BASIS

Continuity equation $\nabla \cdot \mathbf{u} = 0$ give the relation between the velocity components

$$ik_x \hat{u}\left(m, n, z, t\right) + ik_y \hat{v}\left(m, n, z, t\right) + \mathbb{D}\hat{w}\left(m, n, z, t\right) = 0, \tag{4.3}$$

in Fourier space, where $\mathbb{D} = d/dz$ and time t is frozen. The Dirichlet type boundary conditions become:

$$\hat{u}\,(m, n, \pm 1) = \hat{v}\,(m, n, \pm 1) = \hat{w}\,(m, n, \pm 1) = 0. \tag{4.4}$$

The equation (4.3) can be used to construct the solenoidal basis functions. There are four cases with respect to wavenumbers:

CASE 1:

$$k_x \neq 0 \quad \text{and} \quad k_y = 0 \quad \rightarrow \quad ik_x\hat{u} + \mathbb{D}\hat{w} = 0,$$

$$\begin{bmatrix} \hat{u} \\ \hat{v} \\ \hat{w} \end{bmatrix} = \begin{bmatrix} -\mathbb{D}\hat{w}/ik_x \\ \hat{v} \\ \hat{w} \end{bmatrix} = a^{(1)} \begin{bmatrix} 0 \\ g(z) \\ 0 \end{bmatrix} + a^{(2)} \begin{bmatrix} (i/k_x)\mathbb{D}h(z) \\ 0 \\ h(z) \end{bmatrix}, \tag{4.5}$$

CASE 2:

$$k_x = 0 \quad \text{and} \quad k_y \neq 0 \quad \rightarrow \quad ik_y\hat{v} + \mathbb{D}\hat{w} = 0,$$

$$\begin{bmatrix} \hat{u} \\ \hat{v} \\ \hat{w} \end{bmatrix} = \begin{bmatrix} \hat{u} \\ -\mathbb{D}\hat{w}/ik_y \\ \hat{w} \end{bmatrix} = a^{(1)} \begin{bmatrix} g(z) \\ 0 \\ 0 \end{bmatrix} + a^{(2)} \begin{bmatrix} 0 \\ (i/k_y)\mathbb{D}h(z) \\ h(z) \end{bmatrix}, \tag{4.6}$$

CASE 3:

$$k_x = 0 \quad \text{and} \quad k_y = 0 \quad \rightarrow \quad \mathbb{D}\hat{w} = 0,$$

$$\begin{bmatrix} \hat{u} \\ \hat{v} \\ \hat{w} \end{bmatrix} = a^{(1)} \begin{bmatrix} -g(z) \\ 0 \\ 0 \end{bmatrix} + a^{(2)} \begin{bmatrix} 0 \\ g(z) \\ 0 \end{bmatrix}, \tag{4.7}$$

CASE 4:

$$k_x \neq 0 \quad \text{and} \quad k_y \neq 0 \quad \rightarrow \quad ik_x\hat{u} + ik_y\hat{v} + \mathbb{D}\hat{w} = 0,$$

$$\begin{bmatrix} \hat{u} \\ \hat{v} \\ \hat{w} \end{bmatrix} = \begin{bmatrix} -(ik_y\hat{v} + \mathbb{D}\hat{w})/ik_x \\ \hat{v} \\ \hat{w} \end{bmatrix} = a^{(1)} \begin{bmatrix} -(k_y/k_x)g(z) \\ g(z) \\ 0 \end{bmatrix} + a^{(2)} \begin{bmatrix} (i/k_x)\mathbb{D}h(z) \\ 0 \\ h(z) \end{bmatrix}. \tag{4.8}$$

The solenoidal bases are required to satisfy the boundary conditions, thus $g(\pm 1) = h(\pm 1) = \mathbb{D}h(\pm 1) = 0$, and so the polynomials $g(z) = (1 - z^2)L_p(z)$ and $h(z) = (1 - z^2)^2 L_p(z)$ are formed and written in terms of pth order Legendre polynomials, L_p. The choice of the Legendre polynomials is motivated by the upcoming considerations.

The solenoidal flow field can now be expanded in terms of solenoidal basis functions

$$\hat{\mathbf{u}}(m, n, z) = \sum_{p=0}^{Q} \left(a_p^{(1)} \hat{V}_p^{(1)}(z) + a_p^{(2)} \hat{V}_p^{(2)}(z) \right), \tag{4.9}$$

$$\hat{\theta}(m, n, z) = \sum_{p=0}^{Q} \left(b_p \hat{T}_p(z) \right), \tag{4.10}$$

where there is no restriction except boundary conditions for temperature, i.e., $\hat{T}_p(z) = g(z)$.

The solenodial basis functions come in pairs, $\hat{V}_p^{(1,2)}$, and so provide a representation of the velocity field in two degrees of freedom. This is of course expected because the continuity equation provides the connection between three components of the velocity vector and thus reducing the degree of freedom in characterizing the velocity field from three to two. It should be noted that the first bases, $\hat{V}_p^{(1)}$, are lacking in their vertical velocity components, while a little algebra can show that the second bases, $\hat{V}_p^{(2)}$, lack the vertical vorticity component. This is very much similar to the toroidal and poroidal decomposition of the divergence-free velocity field introduced earlier in equation (3.18). According to this classification, the expansion coefficient $a^{(1)}$ is associated with the toroidal component and $a^{(2)}$ is with the poloidal component of the velocity field.

The expansion coefficients may be obtained by an inner product, defined as,

$$\left(\bar{V}, V\right) = \iiint\limits_{\Omega} \bar{V} \cdot V \, d\Omega = \int_{-1}^{+1} \hat{\bar{V}}^{*} \cdot \hat{V} \, dz,$$

for each wave number pair (k_x, k_y) due to the orthogonality of the Fourier bases where (*) denotes complex conjugation. This will be used to project the governing equations onto a projector (dual) space in a Galerkin procedure as well. In order to construct the projector space and the corresponding bases $\bar{V}$ (dual bases), impose the condition of the elimination of the pressure term in the Galerkin projection i.e.

$$\begin{aligned}\left(\bar{V}, \nabla p\right) = \iiint\limits_{\Omega} \bar{V} \cdot \nabla p \, d\Omega &= \iiint\limits_{\Omega} \nabla \cdot \left(p\bar{V}\right) \, d\Omega - \iiint\limits_{\Omega} p\nabla \cdot \bar{V} \, d\Omega \\ &= \iint\limits_{S} p\bar{V} \cdot n \, dS - \iiint\limits_{\Omega} p\nabla \cdot \bar{V} \, d\Omega,\end{aligned}$$

Thus $\bar{V}$ is required to be solenoidal and to satisfy the condition $\bar{V} \cdot \mathbf{n} = 0$ on the bounding surface S with normal n in order to eliminate the pressure term in the Galerkin projection. In the geometry between rigid plates with infinite horizontal extent, this implies that

$$\bar{V} \cdot \mathbf{e_z} \,|_{z=\pm 1} = 0.$$

This can be satisfied by properly selected dual basis as:

CASE 1:

$$k_x \neq 0 \quad \text{and} \quad k_y = 0 \quad \rightarrow \quad ik_x\hat{u} + \mathbb{D}\hat{w} = 0,$$

$$\begin{bmatrix} \hat{u} \\ \hat{v} \\ \hat{w} \end{bmatrix} = \begin{bmatrix} -\mathbb{D}\hat{w}/ik_x \\ \hat{v} \\ \hat{w} \end{bmatrix} = \alpha \begin{bmatrix} 0 \\ f(z) \\ 0 \end{bmatrix} + \beta \begin{bmatrix} (i/k_x)\mathbb{D}g(z) \\ 0 \\ g(z) \end{bmatrix}. \tag{4.11}$$

CASE 2:

$$k_x = 0 \quad \text{and} \quad k_y \neq 0 \quad \rightarrow \quad ik_y\hat{v} + \mathbb{D}\hat{w} = 0,$$

$$\begin{bmatrix} \hat{u} \\ \hat{v} \\ \hat{w} \end{bmatrix} = \begin{bmatrix} \hat{u} \\ -\mathbb{D}\hat{w}/ik_y \\ \hat{w} \end{bmatrix} = \alpha \begin{bmatrix} f(z) \\ 0 \\ 0 \end{bmatrix} + \beta \begin{bmatrix} 0 \\ (i/k_y)\mathbb{D}g(z) \\ g(z) \end{bmatrix}. \tag{4.12}$$

<u>**CASE 3:**</u>

$$k_x = 0 \quad \text{and} \quad k_y = 0 \quad \rightarrow \quad \mathbb{D}\hat{w} = 0,$$

$$\begin{bmatrix} \hat{u} \\ \hat{v} \\ \hat{w} \end{bmatrix} = \alpha \begin{bmatrix} -f(z) \\ 0 \\ 0 \end{bmatrix} + \beta \begin{bmatrix} 0 \\ f(z) \\ 0 \end{bmatrix}. \tag{4.13}$$

<u>**CASE 4:**</u>

$$k_x \neq 0 \quad \text{and} \quad k_y \neq 0 \quad \rightarrow \quad ik_x\hat{u} + ik_y\hat{v} + \mathbb{D}\hat{w} = 0,$$

$$\begin{bmatrix} \hat{u} \\ \hat{v} \\ \hat{w} \end{bmatrix} = \begin{bmatrix} -(ik_y\hat{v} + \mathbb{D}\hat{w})/ik_x \\ \hat{v} \\ \hat{w} \end{bmatrix} = \alpha \begin{bmatrix} -(k_y/k_x)f(z) \\ f(z) \\ 0 \end{bmatrix} + \beta \begin{bmatrix} (i/k_x)\mathbb{D}g(z) \\ 0 \\ g(z) \end{bmatrix}. \tag{4.14}$$

The selection of the polynomials $f(z) = L_p(z)$ and $g(z) = (1 - z^2)L_p(z)$ ensure the satisfaction of the wall surface condition by the dual bases.

Two further considerations in the construction of the bases may facilitate the numerical implementation of the bases. First, Gram-Schmidt process can be used to introduce orthogonality between basis pairs in the ordinary vector sense that amounts to rearrangement of the components without loss of solenoidal property as shown in the representative Case 4 for the basis

$$\hat{V}^{(1)}(z) = \begin{bmatrix} -(k_y/k_x)g(z) \\ g(z) \\ 0 \end{bmatrix}, \quad \hat{V}^{(2)}(z) = \begin{bmatrix} ik_x\mathbb{D}h(z) \\ ik_y\mathbb{D}h(z) \\ (k_x^2 + k_y^2)h(z) \end{bmatrix}, \tag{4.15}$$

and its dual

$$\hat{\bar{V}}^{(1)}(z) = \begin{bmatrix} -(k_y/k_x)f(z) \\ f(z) \\ 0 \end{bmatrix}, \quad \hat{\bar{V}}^{(2)}(z) = \begin{bmatrix} ik_x\mathbb{D}g(z) \\ ik_y\mathbb{D}g(z) \\ (k_x^2+k_y^2)g(z) \end{bmatrix}. \tag{4.16}$$

It can be shown that this rearrangement results in the added convenient property that

$$\left(\bar{V}^{(i)}, V^{(j)}\right) = \gamma_{ij}\delta_{ij} \quad \text{and} \quad \left(\bar{V}^{(i)}, \nabla^2 V^{(j)}\right) = \Gamma_{ij}\delta_{ij},$$

where δ_{ij} is the Kronecker delta.

Table 4.1: Rotational symmetries and their actions in Fourier space

	Symmetry group element	Its action
Identity	I	$\left\{\hat{u}, \hat{v}, \hat{w}, \hat{\theta}, k_x, k_y, z\right\}$
Rotation 90°	R	$\left\{-\hat{v}, \hat{u}, \hat{w}, \hat{\theta}, -k_y, k_x, z\right\}$
Rotation 180°	R^2	$\left\{-\hat{u}, -\hat{v}, \hat{w}, \hat{\theta}, -k_x, -k_y, z\right\}$
Rotation 270°	R^3	$\left\{\hat{v}, -\hat{u}, \hat{w}, \hat{\theta}, k_y, -k_x, z\right\}$
Reflection in x	F	$\left\{-\hat{u}, \hat{v}, \hat{w}, \hat{\theta}, -k_x, k_y, z\right\}$
Diagonal flip	FR	$\left\{\hat{v}, \hat{u}, \hat{w}, \hat{\theta}, k_y, k_x, z\right\}$
Reflection in y	FR^2	$\left\{\hat{u}, -\hat{v}, \hat{w}, \hat{\theta}, k_x, -k_y, z\right\}$
Diagonal flip	FR^3	$\left\{-\hat{v}, -\hat{u}, \hat{w}, \hat{\theta}, -k_y, -k_x, z\right\}$

Second, the rotational symmetries in Table 4.1 can be incorporated into the solenoidal bases with some manipulation of the components without loss of solenoidal property as shown in the representative Case 4.

$$\hat{V}^{(1)}(z) = \begin{bmatrix} -c\ sign(k_xk_y)\ ik_yg(z)/K \\ c\ sign(k_xk_y)\ ik_xg(z)/K \\ 0 \end{bmatrix}, \quad \hat{V}^{(2)}(z) = \begin{bmatrix} ik_x\mathbb{D}h(z)/K \\ ik_y\mathbb{D}h(z)/K \\ Kh(z) \end{bmatrix} \tag{4.17}$$

where *sign* is the sign function, $K = \sqrt{k_x^2+k_y^2}$ and $c = 1$ for $|k_x| < |k_y|$, while $c = -1$ otherwise. Further, the bases satisfy the conjugate property, namely, $\hat{V}(-k_x, -k_y, z) = \hat{V}^*(k_x, k_y, z)$.

Another issue for the implementation is the accurate evaluation of the inner product integrals. This can be achieved by the use of Gaussian quadrature that involves evaluation at the Gauss-Legendre-Lobatto grid z_k and weights ω_k

$$\left(\bar{V}, V\right) = \int_{-1}^{+1} \hat{\bar{V}}^* \cdot \hat{V}\, dz = \sum_{k=0}^{N_z} \hat{\bar{V}}^*(z_k) \cdot \hat{V}(z_k)\, \omega_k,$$

that produces exact results for the integrand a polynomial of degree $\leq 2N_z - 1$, or in space $\mathbb{P}_{2N_z-1}$. Since $V_p^{(1,2)}(z) \in \mathbb{P}_{p+4}$ and $\bar{V}_p^{(1,2)}(z) \in \mathbb{P}_{p+2}$, the Gaussian quadrature gives the exact results in the Galerkin projection of the nonlinear terms as the most demanding term if

$$2N_z - 1 \geq (Q+3) + (Q+4) + (Q+2) = 3Q + 9 \rightarrow N_z \geq (3Q+10)/2,$$

where Q is the highest degree Legendre polynomial used in the representation.

When a representation of the soleniodal flow field in the form

$$\mathbf{u} = \sum_{|m|\leq N_x/2} \sum_{|n|\leq N_y/2} e^{ik_x x + ik_y y} \sum_{p=0}^{Q} \left(a_p^{(1)} \hat{V}_p^{(1)}(z) + a_p^{(2)} \hat{V}_p^{(2)}(z)\right), \tag{4.18}$$

with

$$\theta = \sum_{|m|\leq N_x/2} \sum_{|n|\leq N_y/2} e^{ik_x x + ik_y y} \sum_{p=0}^{Q} b_p \hat{T}_p(z), \tag{4.19}$$

are substituted into the governing equations (2.15) and (2.16), the residuals arise

$$\begin{aligned} R_{\mathbf{u}} &= -\frac{\partial \mathbf{u}}{\partial t} - (\mathbf{u}\cdot\nabla)\,\mathbf{u} - \nabla p + PrRa_h\theta e_z + Pr\nabla^2\mathbf{u}, \\ R_\theta &= -\frac{\partial\theta}{\partial t} - (\mathbf{u}\cdot\nabla)\,\theta - \frac{\mathbf{u}\cdot e_z}{2} + \nabla^2\theta. \end{aligned}$$

The projection of these residuals onto the dual space spanned by $\bar{V}_p^{(1)}$, $\bar{V}_p^{(2)}$ and $\bar{T}_p$ ($= \hat{T}_p$) is annuled

$$\left(\bar{V}, R_{\mathbf{u}}\right) = 0, \quad \left(\bar{T}, R_\theta\right) = 0,$$

to get

$$\begin{pmatrix} \left(\bar{V}^{(1)}, \hat{V}^{(1)}\right) & \left(\bar{V}^{(1)}, \hat{V}^{(2)}\right) \\ \left(\bar{V}^{(2)}, \hat{V}^{(1)}\right) & \left(\bar{V}^{(2)}, \hat{V}^{(2)}\right) \end{pmatrix} \begin{pmatrix} \dot{a}^{(1)} \\ \dot{a}^{(2)} \end{pmatrix} + \begin{pmatrix} c^{(1)} \\ c^{(2)} \end{pmatrix} =$$
$$PrRa_h \begin{pmatrix} \left(\bar{V}^{(1)}, \hat{T} e_z\right) \\ \left(\bar{V}^{(2)}, \hat{T} e_z\right) \end{pmatrix} \begin{pmatrix} b \\ b \end{pmatrix} + Pr \begin{pmatrix} \left(\bar{V}^{(1)}, \nabla^2 \hat{V}^{(1)}\right) & \left(\bar{V}^{(1)}, \nabla^2 \hat{V}^{(2)}\right) \\ \left(\bar{V}^{(2)}, \nabla^2 \hat{V}^{(1)}\right) & \left(\bar{V}^{(2)}, \nabla^2 \hat{V}^{(2)}\right) \end{pmatrix} \begin{pmatrix} a^{(1)} \\ a^{(2)} \end{pmatrix},$$

$$\left(\bar{T},\hat{T}\right)\dot{b}+d=\left(\bar{T},\hat{V}^{(1)}\cdot e_z\right)a^{(1)}+\left(\bar{T},\hat{V}^{(2)}\cdot e_z\right)a^{(2)}+\left(\bar{T},\nabla^2\hat{T}\right)b,$$

under Galerkin procedure where $c^{(1)}$, $c^{(2)}$ and d are nonlinear terms. At this point, it is important to note that by the construction of the solenoidal basis and its dual, the pressure term vanishes in the resulting system.

Products of cross components of basis and dual basis vanish by construction and system reduces to:

$$\begin{pmatrix}\left(\bar{V}^{(1)},\hat{V}^{(1)}\right) & 0\\ 0 & \left(\bar{V}^{(2)},\hat{V}^{(2)}\right)\end{pmatrix}\begin{pmatrix}\dot{a}^{(1)}\\ \dot{a}^{(2)}\end{pmatrix}+\begin{pmatrix}c^{(1)}\\ c^{(2)}\end{pmatrix}=$$

$$PrRa_h\begin{pmatrix}0\\ \left(\bar{V}^{(2)},\hat{T}e_z\right)\end{pmatrix}\begin{pmatrix}b\\ b\end{pmatrix}+Pr\begin{pmatrix}\left(\bar{V}^{(1)},\nabla^2\hat{V}^{(1)}\right) & 0\\ 0 & \left(\bar{V}^{(2)},\nabla^2\hat{V}^{(2)}\right)\end{pmatrix}\begin{pmatrix}a^{(1)}\\ a^{(2)}\end{pmatrix},$$

$$\left(\bar{T},\hat{T}\right)\dot{b}+d=\left(\bar{T},\hat{V}^{(2)}\cdot e_z\right)a^{(2)}+\left(\bar{T},\nabla^2\hat{T}\right)b.$$

Then have a system governing the time evolution of the time dependent expansion coefficients $a^{(1,2)}, b$ with the mass (M) and stiffness (S) matrices:

$$\underbrace{\begin{pmatrix}\left(\bar{V}^{(1)},\hat{V}^{(1)}\right) & 0 & 0\\ 0 & \left(\bar{V}^{(2)},\hat{V}^{(2)}\right) & 0\\ 0 & 0 & \left(\bar{T},\hat{T}\right)\end{pmatrix}}_{M}\begin{pmatrix}\dot{a}^{(1)}\\ \dot{a}^{(2)}\\ \dot{b}\end{pmatrix}+\begin{pmatrix}c^{(1)}\\ c^{(2)}\\ d\end{pmatrix}=$$

$$\underbrace{Pr\begin{pmatrix}\left(\bar{V}^{(1)},\nabla^2\hat{V}^{(1)}\right) & 0 & 0\\ 0 & \left(\bar{V}^{(2)},\nabla^2\hat{V}^{(2)}\right) & Ra_h\left(\bar{V}^{(2)},\hat{T}e_z\right)\\ 0 & \left(\bar{T},\hat{V}^{(2)}\cdot e_z\right)/2Pr & \left(\bar{T},\nabla^2\hat{T}\right)/Pr\end{pmatrix}}_{S}\begin{pmatrix}a^{(1)}\\ a^{(2)}\\ b\end{pmatrix}. \tag{4.20}$$

4.2 LINEAR STABILITY ANALYSIS

Linear stability of Boussinesq hydrodynamic equations is investigated by Chandrasekhar [2]. Chandrasekhar found that critical wavenumber and critical Rayleigh number are independent of the Prandtl number. Reid and Harris [74] found the stability curve has one minima at critical wavenumber equal to 3.117 and critical Rayleigh number at 1707.8 for viscous fluids confined between rigid plates. Below the critical point, the fluid layer has no motion and heat is transfered by conduction throughout the fluid layer. Any perturbation is damped by the system in this stable region. When the Rayleigh number is increased over the critical value buoyancy forces overcome the viscous forces and two dimensional steady rolls are formed. Rayleigh number is the main control parameter in the convective regime. Periodic, double periodic and weakly turbulent regimes are developed as the Rayleigh number is increased.

At the onset of convective motions, the velocity and temperature perturbations over the conductive state are small, so that the nonlinear terms in the governing equations (2.15) and (2.16) can be neglected to get the residuals

$$\begin{aligned} R_{\mathbf{u}} &= -\frac{\partial \mathbf{u}}{\partial t} - \nabla p + PrRa_h \theta e_z + Pr\nabla^2 \mathbf{u}, \\ R_\theta &= -\frac{\partial \theta}{\partial t} - \frac{\mathbf{u}\cdot e_z}{2} + \nabla^2\theta, \end{aligned}$$

after the truncated representations in terms of the bases 6.1 and 6.2 are substituted. The annuling of the projected residuals results in the linear system of ODEs;

$$\begin{pmatrix} \left(\bar V^{(1)}, \hat V^{(1)}\right) & \left(\bar V^{(1)}, \hat V^{(2)}\right) \\ \left(\bar V^{(2)}, \hat V^{(1)}\right) & \left(\bar V^{(2)}, \hat V^{(2)}\right) \end{pmatrix} \begin{pmatrix} \dot a^{(1)} \\ \dot a^{(2)} \end{pmatrix} =$$

$$PrRa_h \begin{pmatrix} \left(\bar V^{(1)}, \hat T e_z\right) \\ \left(\bar V^{(2)}, \hat T e_z\right) \end{pmatrix} \begin{pmatrix} b \\ b \end{pmatrix} + Pr \begin{pmatrix} \left(\bar V^{(1)}, \nabla^2 \hat V^{(1)}\right) & \left(\bar V^{(1)}, \nabla^2 \hat V^{(2)}\right) \\ \left(\bar V^{(2)}, \nabla^2 \hat V^{(1)}\right) & \left(\bar V^{(2)}, \nabla^2 \hat V^{(2)}\right) \end{pmatrix} \begin{pmatrix} a^{(1)} \\ a^{(2)} \end{pmatrix},$$

$$\left(\bar T, \hat T\right) \dot b = \left(\bar T, \hat V^{(1)} \cdot e_z\right) a^{(1)} + \left(\bar T, \hat V^{(2)} \cdot e_z\right) a^{(2)} + \left(\bar T, \nabla^2 \hat T\right) b.$$

The two systems can be combined into one governing system after introducing the vanishing products of the cross components of basis and dual basis to get:

$$\underbrace{\begin{pmatrix} \left(\bar V^{(1)}, \hat V^{(1)}\right) & 0 & 0 \\ 0 & \left(\bar V^{(2)}, \hat V^{(2)}\right) & 0 \\ 0 & 0 & \left(\bar T, \hat T\right) \end{pmatrix}}_{M} \begin{pmatrix} \dot a^{(1)} \\ \dot a^{(2)} \\ \dot b \end{pmatrix} =$$

$$\underbrace{Pr \begin{pmatrix} \left(\bar V^{(1)}, \nabla^2 \hat V^{(1)}\right) & 0 & 0 \\ 0 & \left(\bar V^{(2)}, \nabla^2 \hat V^{(2)}\right) & Ra_h \left(\bar V^{(2)}, \hat T e_z\right) \\ 0 & \left(\bar T, \hat V^{(2)} \cdot e_z\right)/2Pr & \left(\bar T, \nabla^2 \hat T\right)/Pr \end{pmatrix}}_{S} \begin{pmatrix} a^{(1)} \\ a^{(2)} \\ b \end{pmatrix}, \tag{4.21}$$

where M and S refer to the mass and the stiffness matrices, respectively, as before. After introducing a time dependence of the expansion coefficients in the form of $a^{(1)}(t) = exp(\lambda t)a_0^{(1)}$, $a^{(2)}(t) = exp(\lambda t)a_0^{(2)}$ and $b(t) = exp(\lambda t)b_0$ into the above system, one gets the generalized eigenvalue problem

$$\lambda M \begin{pmatrix} a_0^{(1)} \\ a_0^{(2)} \\ b_0 \end{pmatrix} = S \begin{pmatrix} a_0^{(1)} \\ a_0^{(2)} \\ b_0 \end{pmatrix}.$$

The stability is determined by the eigenvalues of this problem. As the rightmost eigenvalue in the complex plane crosses the imaginary axis as Rayleigh number is varied for a given wavenumber $\xi = 2\pi/S_x$ (or $\eta = 2\pi/S_y$ for $S_x = S_y$) that corresponds to the wavenumber pair ($k_x = \xi, k_y = 0$), the system becomes unstable to infinitesimal perturbations. The resulting critical values of Rayleigh number and the wavenumber are shown in Table 4.2 and the corresponding marginal stability curve in Figure 4.1. These are in excellent agreement with literature [2].

Table 4.2: Linear stability points

k_c	1	2	3	3.117	4	5	6	7
Ra_c	5854.48	2177.41	1711.27	1707.76	1879.25	2439.32	3417.98	4918.54

The corresponding flow field can be visualized by constructing a stream function [65, 75] Ψ defined by

$$D\Psi = k_x \mathbf{u} \cdot e_x + k_y \mathbf{u} \cdot e_y = 2\Re \left\{ exp\left(i\left(k_x x + k_y y\right)\right) \sum_{p=0}^{Q} \left(a_p^{(1)} k_x V_p^{(1)} \cdot e_x + a_p^{(1)} k_y V_p^{(2)} \cdot e_y\right) \right\}$$

that gives

$$\Psi = 2k^2 \Re \left\{ iexp\left(i\left(k_x x + k_y y\right)\right) \left(1 - z^2\right)^2 \sum_{p=0}^{Q} a_p^{(2)} L_p(z) \right\}$$

as shown in Figure 4.2 in the form of two-dimensional steady rolls.

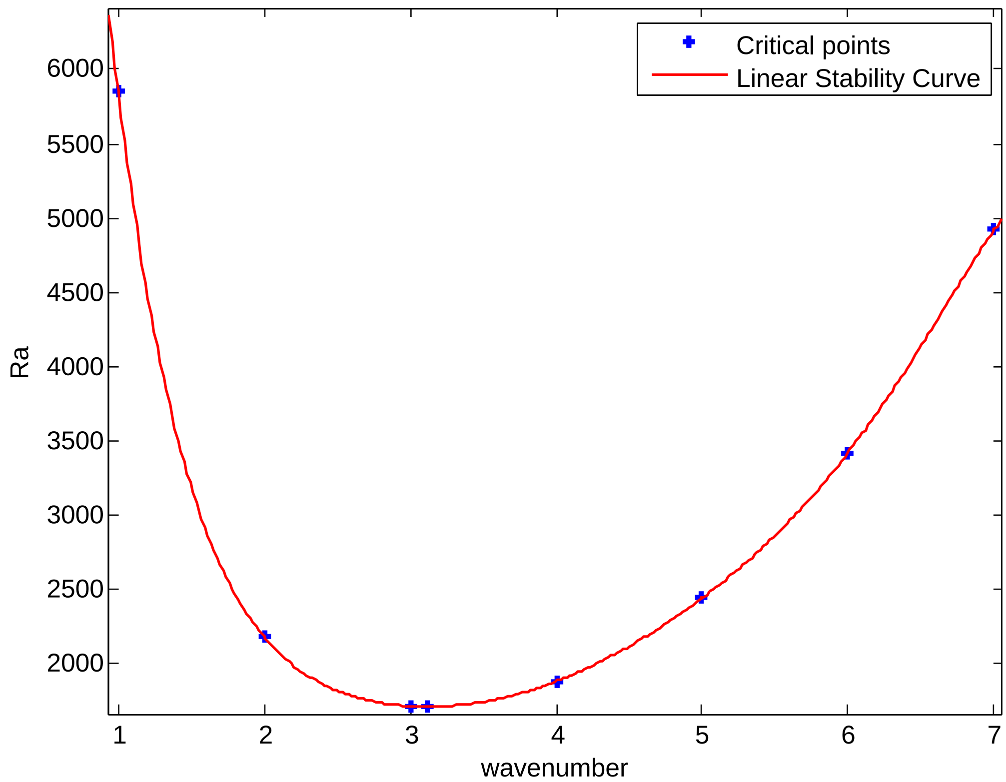

Figure 4.1: Linear stability curve

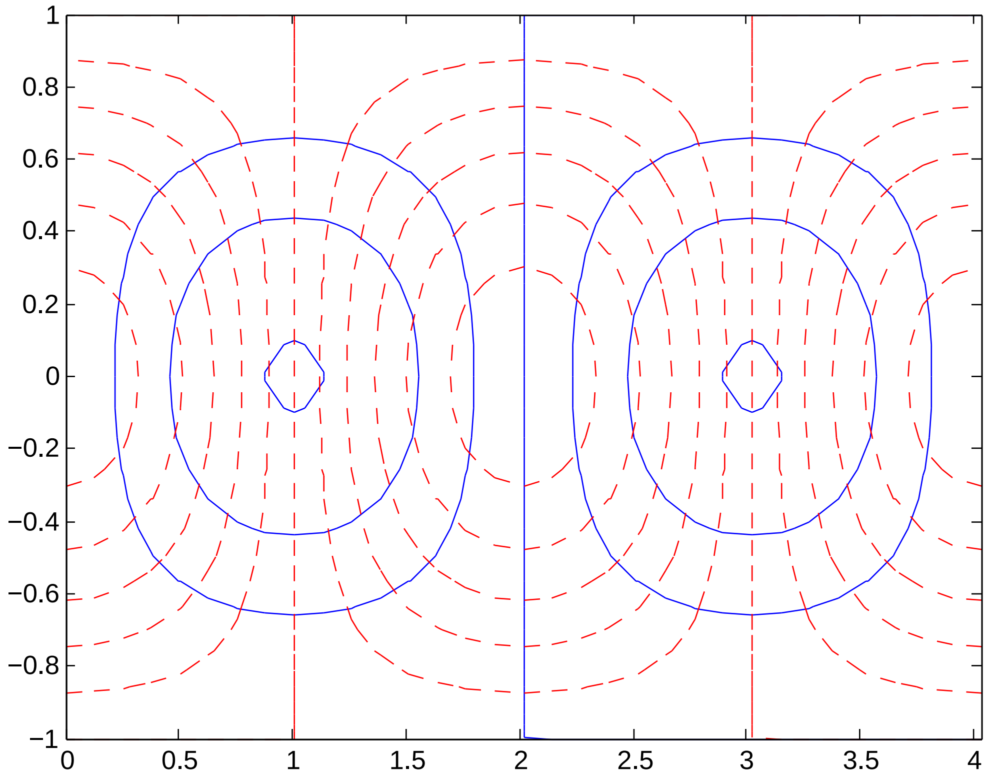

Figure 4.2: The contours of the streamfunction (solid line) and the isotherms (dash line) corresponding to the marginally stable eigenmode at $k_c = 3.117$ and $Ra_c = 1707.8$.

4.3 TIME DISCRETIZATION

For time discretization, semi-implicit numerical integration is used. The nonlinear and driving (buoyancy) terms are integrated explicitly using third order Adams-Bashforth, while diffusive terms are integrated implicitly by Adams-Moulton. Also second order Crank-Nicolson & Adam-Bashfort and fourth order Adam-Bashfort & Adams-Moultan schemes are tested but the third order scheme is selected because it gives acceptable accuracy with acceptable computational effort [72]. In this scheme, the governing equations (2.15) and (2.16) are discretized as follows:

$$\begin{aligned}\frac{\mathbf{u}^{n+1}-\mathbf{u}^{n}}{\Delta t} &= \frac{23}{12}\left(-\left(\mathbf{u}\cdot\nabla\right)\mathbf{u}+PrRa_{h}\theta e_{z}\right)^{n}-\frac{16}{12}\left(-\left(\mathbf{u}\cdot\nabla\right)\mathbf{u}+PrRa_{h}\theta e_{z}\right)^{n-1} \\ &\quad+\frac{5}{12}\left(-\left(\mathbf{u}\cdot\nabla\right)\mathbf{u}+PrRa_{h}\theta e_{z}\right)^{n-2}+Pr\nabla^{2}\left(\frac{5}{12}\mathbf{u}^{n+1}+\frac{8}{12}\mathbf{u}^{n}-\frac{1}{12}\mathbf{u}^{n-1}\right),\end{aligned} \tag{4.22}$$

$$\begin{aligned}\frac{\theta^{n+1}-\theta^{n}}{\Delta t} &= \frac{23}{12}\left(-\left(\mathbf{u}\cdot\nabla\right)\theta+\frac{\mathbf{u}\cdot e_{z}}{2}\right)^{n}-\frac{16}{12}\left(-\left(\mathbf{u}\cdot\nabla\right)\theta+\frac{\mathbf{u}\cdot e_{z}}{2}\right)^{n-1} \\ &\quad+\frac{5}{12}\left(-\left(\mathbf{u}\cdot\nabla\right)\theta+\frac{\mathbf{u}\cdot e_{z}}{2}\right)^{n-2}+\nabla^{2}\left(\frac{5}{12}\theta^{n+1}+\frac{8}{12}\theta^{n}-\frac{1}{12}\theta^{n-1}\right).\end{aligned} \tag{4.23}$$

The projection of the time discretized form of the governing equations after the substitution of the truncated expansions (6.1) and (6.2) results in

$$\begin{aligned}M(1,1)\frac{a^{(1)^{n+1}}-a^{(1)^{n}}}{\Delta t} &= \frac{1}{12}S(1,1)\left(5a^{(1)^{n+1}}+8a^{(1)^{n}}-a^{(1)^{n-1}}\right) \\ &\quad-\frac{1}{12}\left(23c^{(1)^{n}}-16c^{(1)^{n-1}}+5c^{(1)^{n-2}}\right), \\ M(2,2)\frac{a^{(2)^{n+1}}-a^{(2)^{n}}}{\Delta t} &= \frac{1}{12}S(2,2)\left(5a^{(2)^{n+1}}+8a^{(2)^{n}}-a^{(2)^{n-1}}\right) \\ &\quad-\frac{1}{12}\left(23c^{(2)^{n}}-16c^{(2)^{n-1}}+5c^{(2)^{n-2}}\right) \\ &\quad+\frac{1}{12}S(2,3)\left(23b^{n}-16b^{n-1}+5b^{n-2}\right), \\ M(3,3)\frac{b^{n+1}-b^{n}}{\Delta t} &= \frac{1}{12}S(3,3)\left(5b^{n+1}+8b^{n}-b^{n-1}\right) \\ &\quad-\frac{1}{12}\left(23d^{n}-16d^{n-1}+5d^{n-2}\right) \\ &\quad+\frac{1}{12}S(3,2)\left(23a^{(2)^{n}}-16a^{(2)^{n-1}}+5a^{(2)^{n-2}}\right),\end{aligned}$$

where $M(i,j)$ and $S(i,j)$ refer to the $(i,j)^{\text{th}}$ block matrices of the mass and stiffness matrices, respectively. It is obvious that temporal discretization requires three known steps to calculate the unknown step. Linear stability eigen-solution or known nonlinear solution from the previous run can be used as initial conditions.

4.4 NONLINEAR IMPLEMENTATION

The nonlinear advection terms in the momentum and energy equations have significant importance at high Rayleigh numbers. The computation of these terms consumes more time in Fourier-Legendre space than in real space. Thus all nonlinear terms are calculated in real space then projected onto Fourier-Legendre space to obtain the time dependent coefficients [66, 75]

$$c^{1,2} = \left(\bar{V}^{(1,2)}, (\mathbf{u} \cdot \nabla)\,\mathbf{u}\right) \quad \text{and} \quad d = \left(\bar{T}, (\mathbf{u} \cdot \nabla)\,\theta\right), \tag{4.24}$$

that denote the projection of the nonlinear terms onto the dual space. Forward and backward Fourier transforms are used in computing these terms by transforming between real and Fourier spaces.

Derivatives of velocity and temperature fields in horizontal directions are calculated basicaly by Fourier transforms (FFT), while Legendre differentiation matrix [76] is used for the vertical direction. The use of Fourier differentiation matrix [76] is tested for computing derivatives in horizontal directions, however, it is observed that FFT algorithm performs faster than matrix algorithm for horizontal resolutions used.

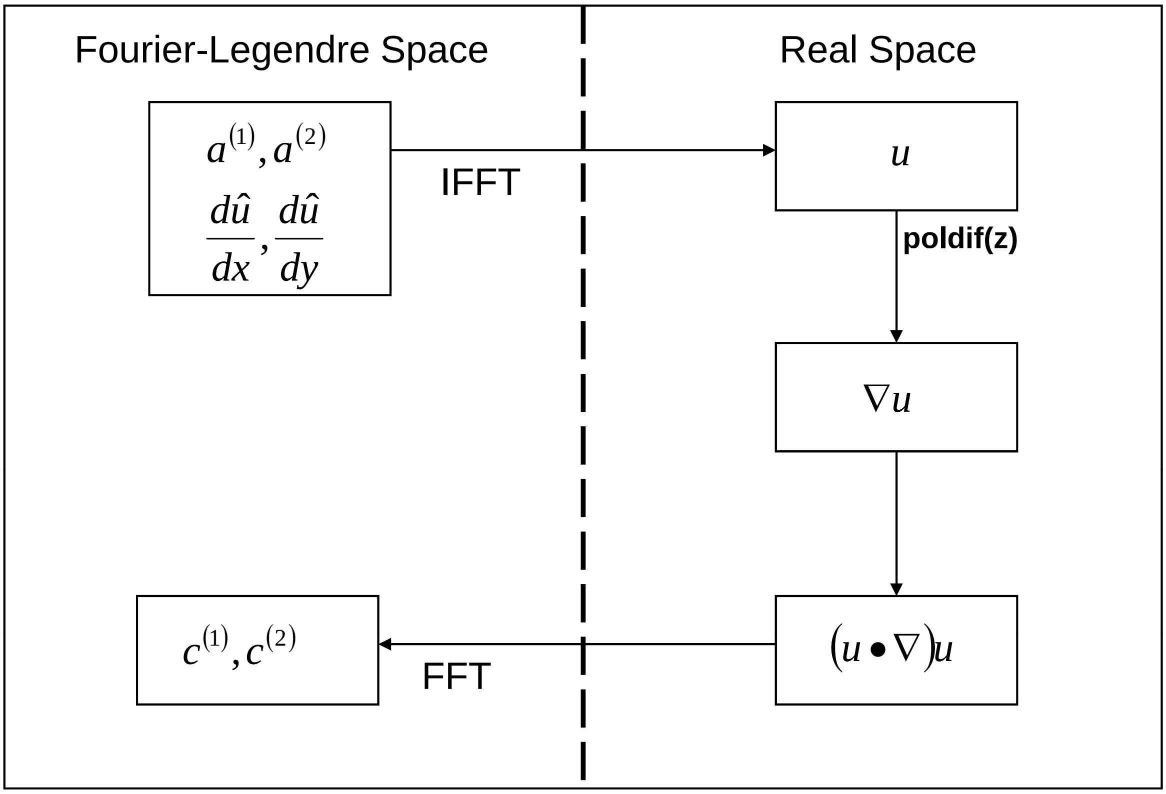

Figure 4.3: Time dependent coefficient of nonlinear velocity term

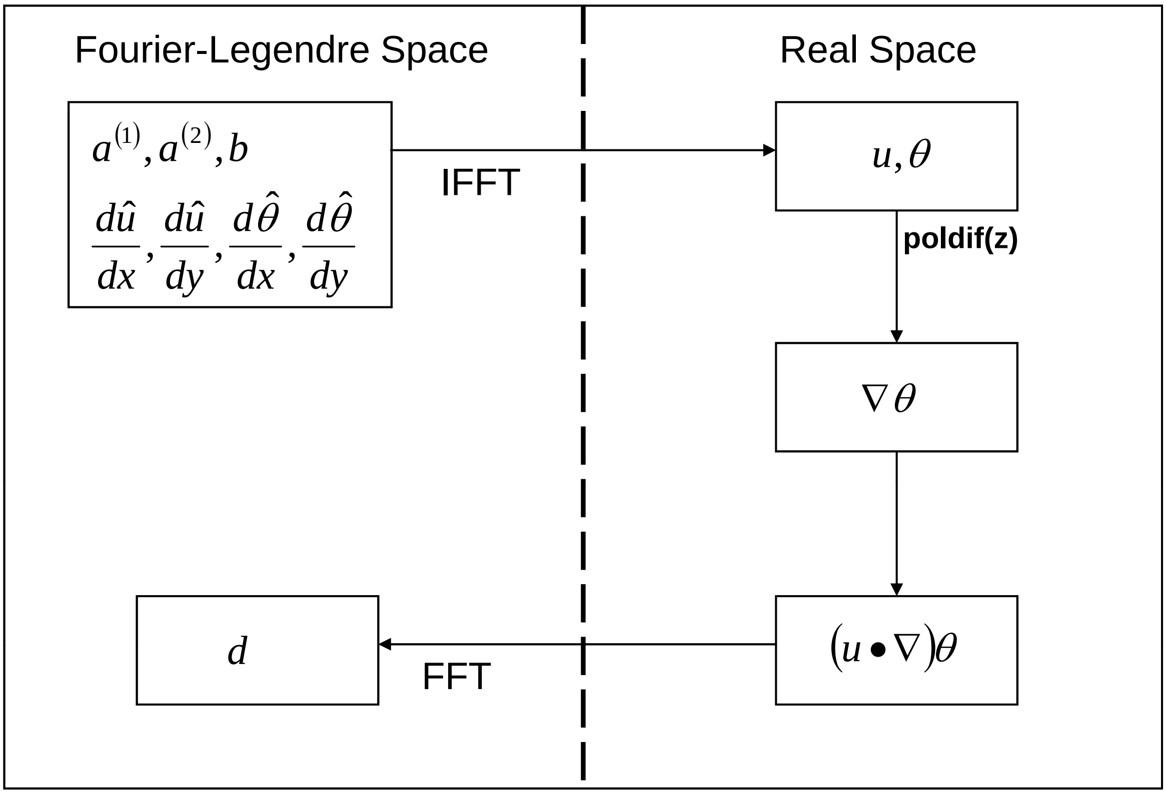

Figure 4.4: Time dependent coefficient of nonlinear temperature term

CHAPTER 5

DIRECT NUMERICAL SIMULATION OF RAYLEIGH BÉNARD CONVECTION

5.1 VERIFICATION

Direct numerical simulation (DNS) code is written using Fortran programing language and includes some numerical tools and schemes. Reliability of the code is tested in various numerical experiments. First of all, the divergence free condition is tested. Afterall, the expansion in terms of solenoidal bases are expected to satisfy the divergence free condition. The code is fully divergence free.

Sensivity to the resolution is tested using computed Nusselt number for various vertical and horizontal resolutions in Figures 5.1 and 5.2, respectively. Vertical resolution is important because thermal and viscous boundary layers must be resolved adequately. At least two nodes have to be located in the boundary layer to provide adequate resolution. Nusselt number involves the gradiant of temperature in the boundary layer, thus it may used to test for the adequacy of resolution. The vertical and horizontal resolution is increased until the relative change in the computed Nusselt number is less than 0.01. As expected, Nusselt number is much more sensitive to the resolution in the vertical direction. The runs in this thesis are also tested in the similar fashion.

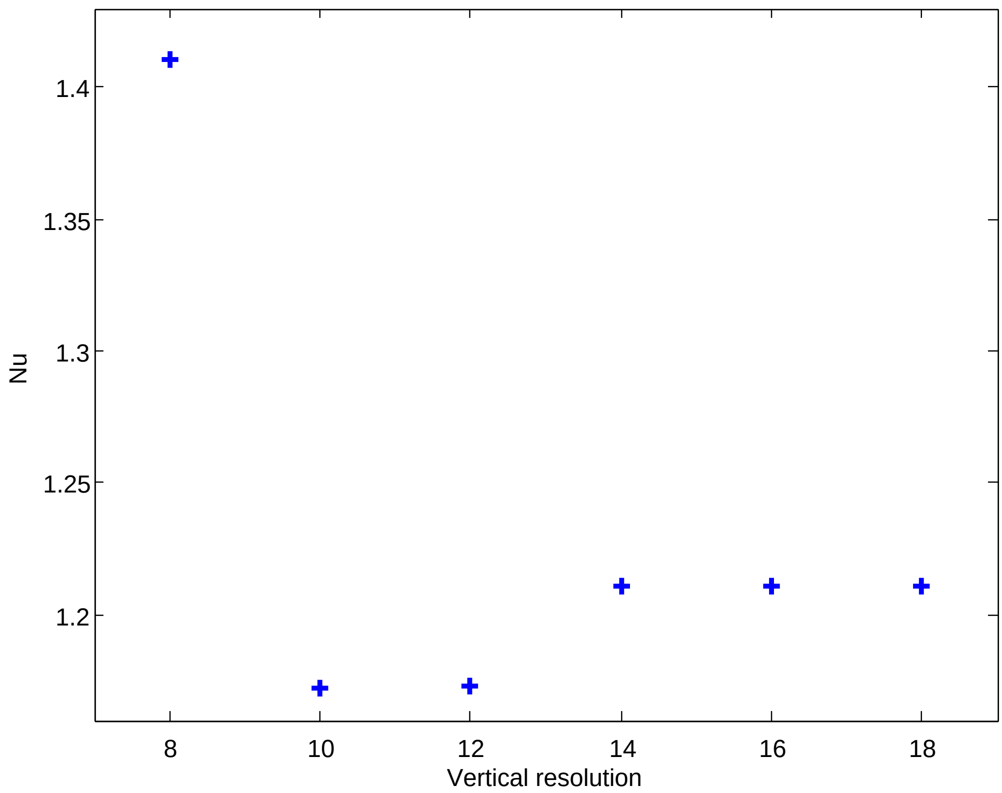

Figure 5.1: Vertical grid refinement for Pr=0.71, Ra=2000, horizontal resolution=16.

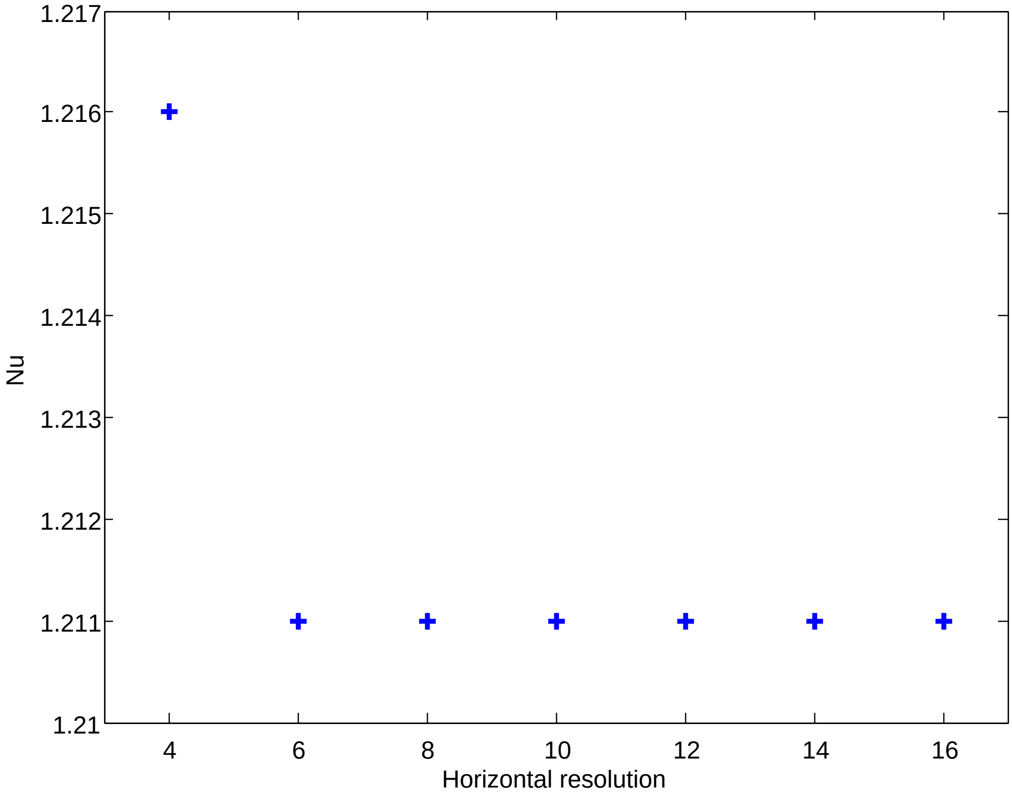

Figure 5.2: Horizontal grid refinement for Pr=0.71, Ra=2000, vertical resolution=16.

5.1.1 HEAT TRANSPORT

Nusselt number is one of the most reported value in literature either experimental or numerical. Convective motion sets in when the Rayleigh number exceeds the critical value, ie., $Ra_c = 1707.76$ [2]. In Figure 5.3, transient behavior of Nusselt number is shown for $Pr = 0.71$ on the 16x16x16 spatial grid. Starting from the linear stability eigensolution as the initial condition, Nusselt number rises from 1 until convergence is reached at its actual value. The speed of convergence is observed to increase with increasing Rayleigh number. For near critical Rayleigh numbers, $Ra > Ra_c$, as the conductive state has just lost its stability indicated by the eigenvalues crossing the imaginary axis, the time rate of change is dictated by the real parts of the eigenvalues that are very small (§4.2). Thus, transients take longer. As Rayleigh number increases, the nonlinear effects get stronger and play stronger role in the time rate of change. This translates into shorter transients and faster convergence.

Decay of kinetic energy is plotted for three cases of Prandtl number in Figure 5.4 when Rayleigh number is set at $Ra = 1700 < Ra_c$. Kinetic energy eventually decays to zero in this no motion state, however, with rates of decay depending on Prandtl number. In this process, where convergence to no motion state is underway, the nonlinear terms are loosing their effects, the viscous terms dominate. Thus, high Prandtl case is observed to loose its kinetic energy faster in comparison to low Prandtl number case as Pr is inversely proportional to viscosity. The linearity of decay also supports that linear terms are in effect in this process. This effect is also observed in the decay of Nusselt number to its conductive state value of unity in Figure 5.5 for $Ra = 0.99 * Ra_c$. For $Ra = 1.01 * Ra_c$ in Figure 5.6, on the other hand, the trend of change in Nusselt number is growth that is faster for higher Prandt number. In this case, the process discussed above is reversed and lower dissipative forces in the case of higher Prandtl numbers have less effect on growth.

Figures 5.7 and 5.8 show the evolution of three dimensional disturbances at $Ra = 2000$ for $Pr = 0.71$. As initial condition, random temperature field is added onto the linear stability eigensolution as perturbation. The flow eventually converges to two-dimensional roll solution as one of the horizontal velocity component decays to zero as expected. The eventual roll direction is selected randomly by convective processes because square planform of the convective box introduces degeneracy for the preference of horizontal directions. If rectangular box were selected instead, the rolls would be directed along the longer side.

Nusselt number is one of the main indicator quantity in thermal convection because heat transfer rate and heat transfer mechanism are important for practical applications in practice, for example; ventilation, cooling or heating, that is worth controlled by scientists and engineers. As further means of validation, numerically obtained Nusselt number values are compared with the literature [1] in Table 5.1. Our results are in agreement with the literature for the values up to $Nu \approx 3$ for moderate Prandtl numbers. The agreement is also good for high Prandtl number for some wavenumbers. These results show that code is capable to simulate the Rayleigh-Bénard convection accurately.

Table 5.1: Heat flux of the convection. *Italic* values refer to Clever&Busse [1]

	$Pr = 0.71$			$Pr = 7$		
Ra	$\alpha = 2.2$	$\alpha = 2.6$	$\alpha = 3.117$	$\alpha = 2.2$	$\alpha = 2.6$	$\alpha = 3.117$
2000	-	1.151	1.211	1.195	1.147	1.213
	-	*1.152*	*1.212*	-	*1.155*	*1.214*
2500	1.288	1.418	1.475	1.452	1.415	1.479
	1.289	*1.418*	*1.475*	*1.295*	*1.424*	*1.478*
3000	1.489	1.610	1.668	1.646	1.619	1.670
	1.489	*1.608*	*1.663*	*1.500*	*1.615*	*1.667*
5000	1.956	2.060	2.123	2.104	2.111	2.027
	1.948	*2.056*	*2.116*	*1.969*	*2.060*	*2.112*
10000	2.426	2.547	2.618	2.491	2.544	2.729
	2.468	*2.581*	*2.661*	*2.473*	*2.557*	*2.618*
20000	2.945	3.051	3.173	2.982	3.279	3.412
	2.995	*3.136*	*3.258*	*2.930*	*3.030*	*3.119*
30000	3.205	3.406	3.436	3.594	3.753	3.853
	3.346	*3.511*	*3.662*	*3.203*	*3.323*	*3.440*

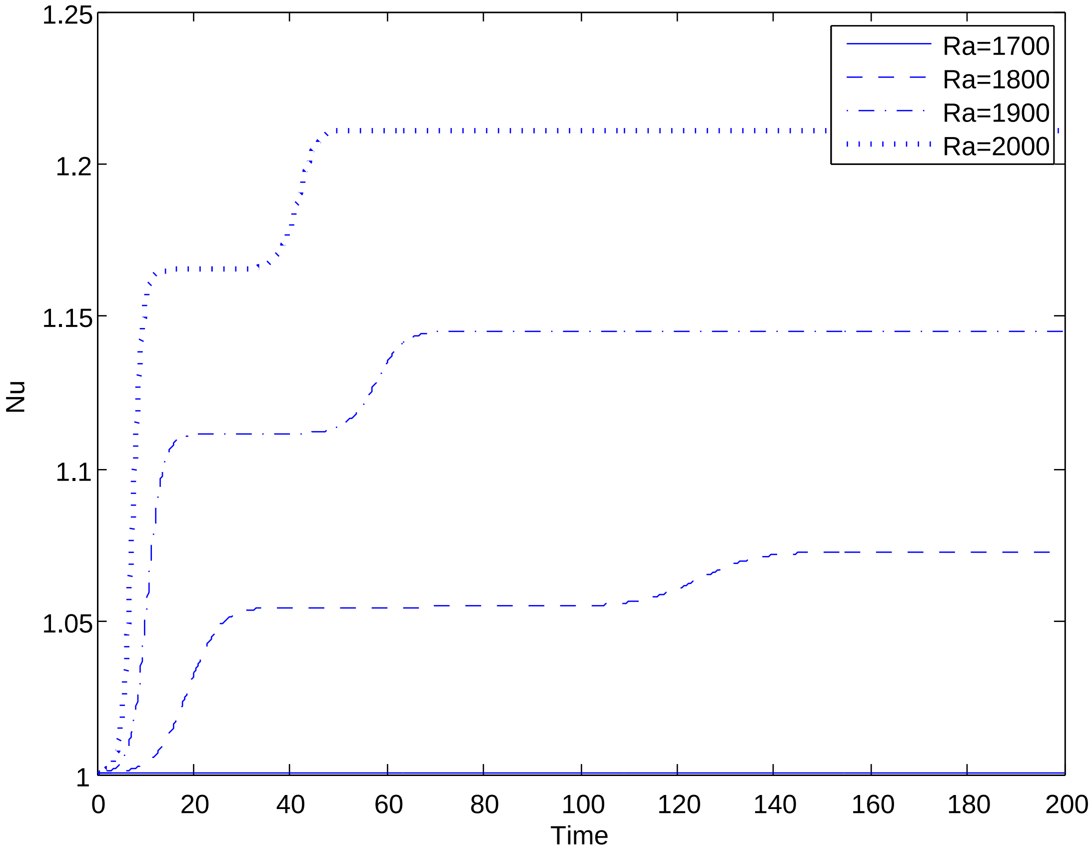

Figure 5.3: Heat transport for Pr=0.71 at 16x16x16 resolution

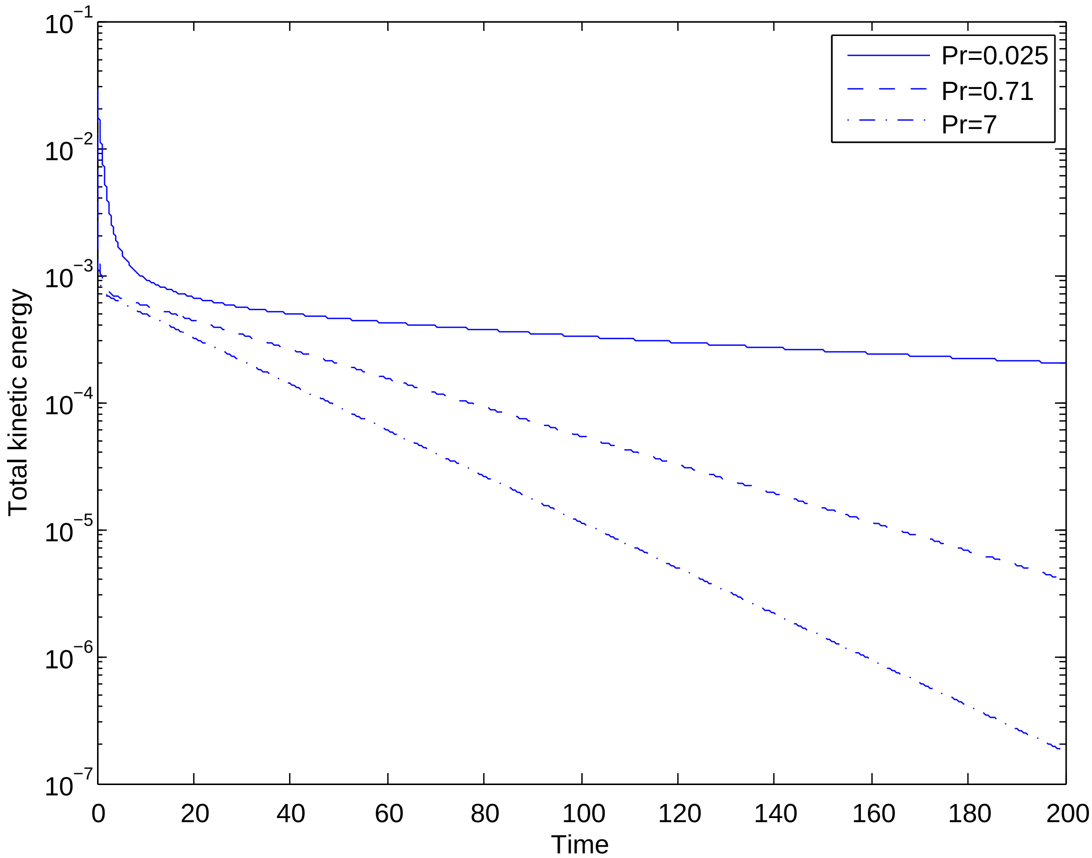

Figure 5.4: Total Kinetic Energy variation at conductive regime (Ra=1700)

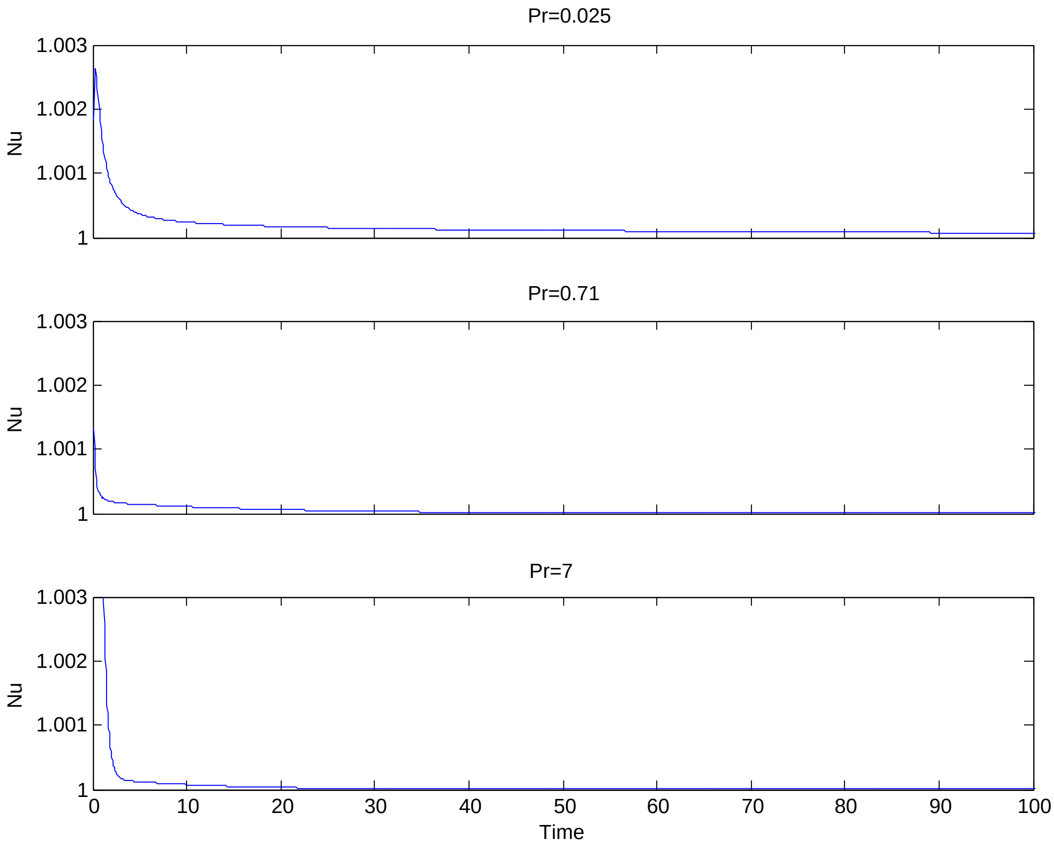

Figure 5.5: Heat flux variation with time below the marginal stability point ($Ra = 0.99Ra_c$)

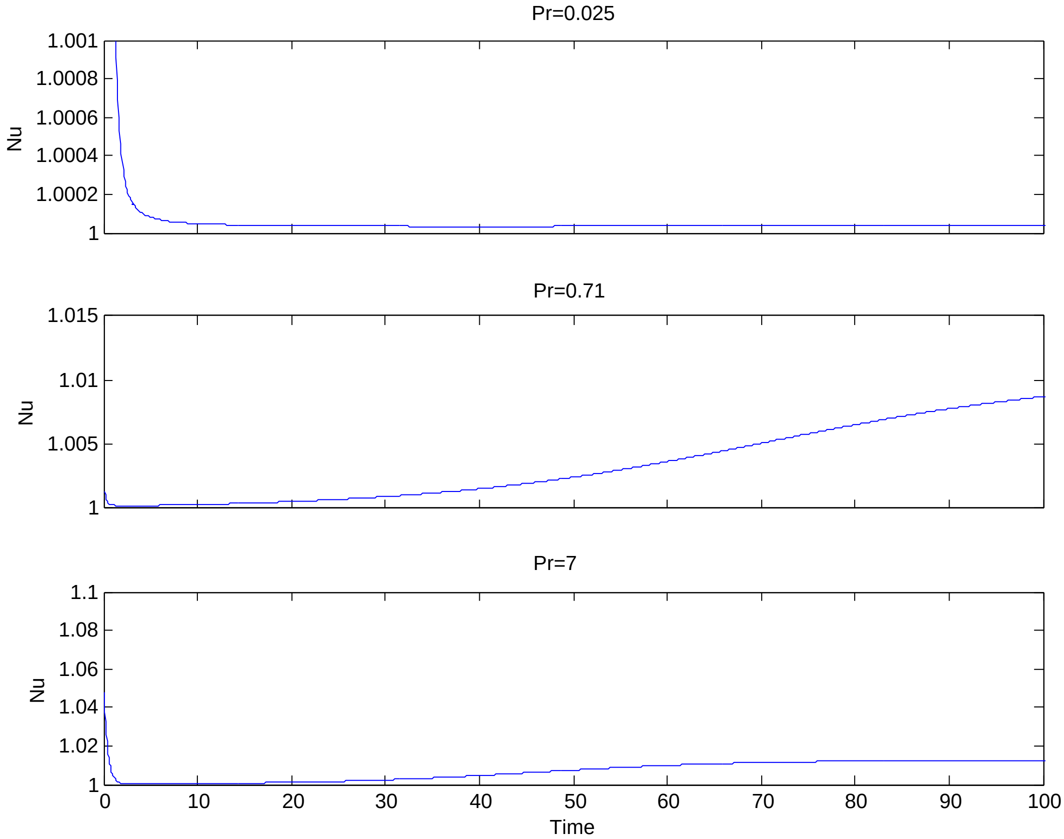

Figure 5.6: Heat flux variation with time above the marginal stability point ($Ra = 1.01Ra_c$)

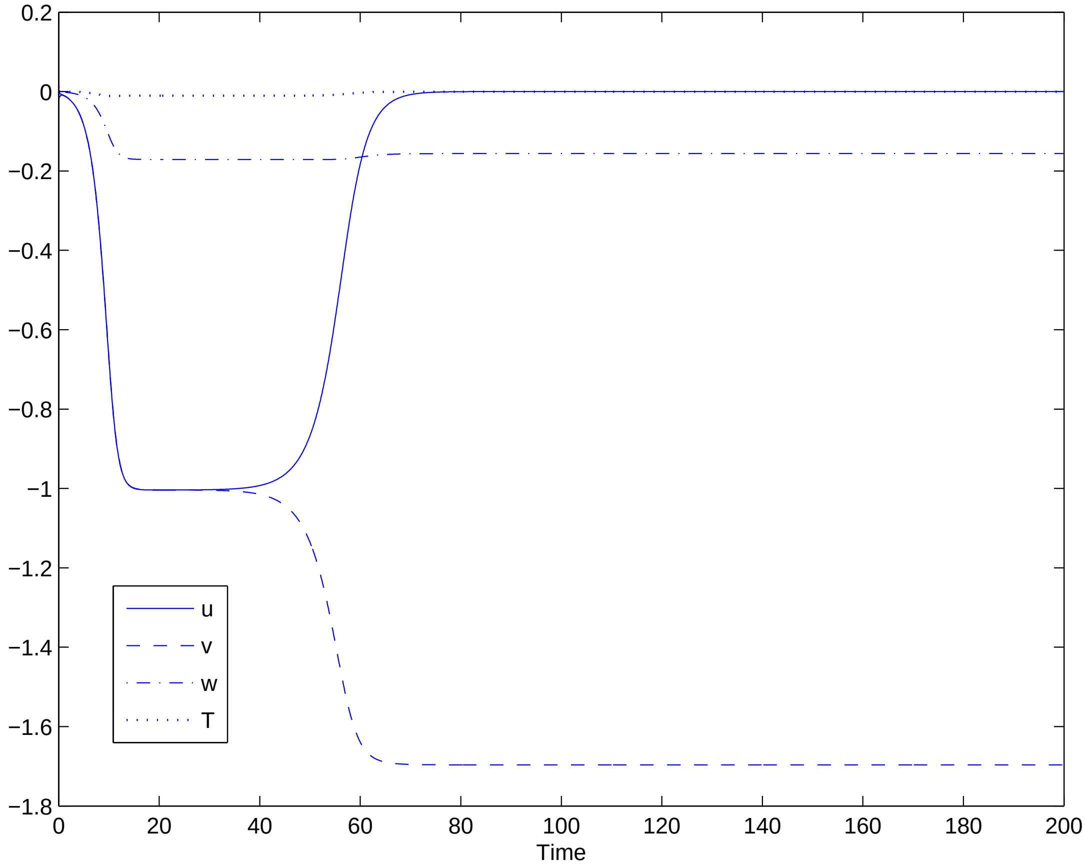

Figure 5.7: Velocity and temperature evolution with time for steady two dimensional roll regime, Pr=0.71, Ra=2000, 16x16x16 resolution at $x = L_x/4$, $y = L_y/4$, $z = -0.792$

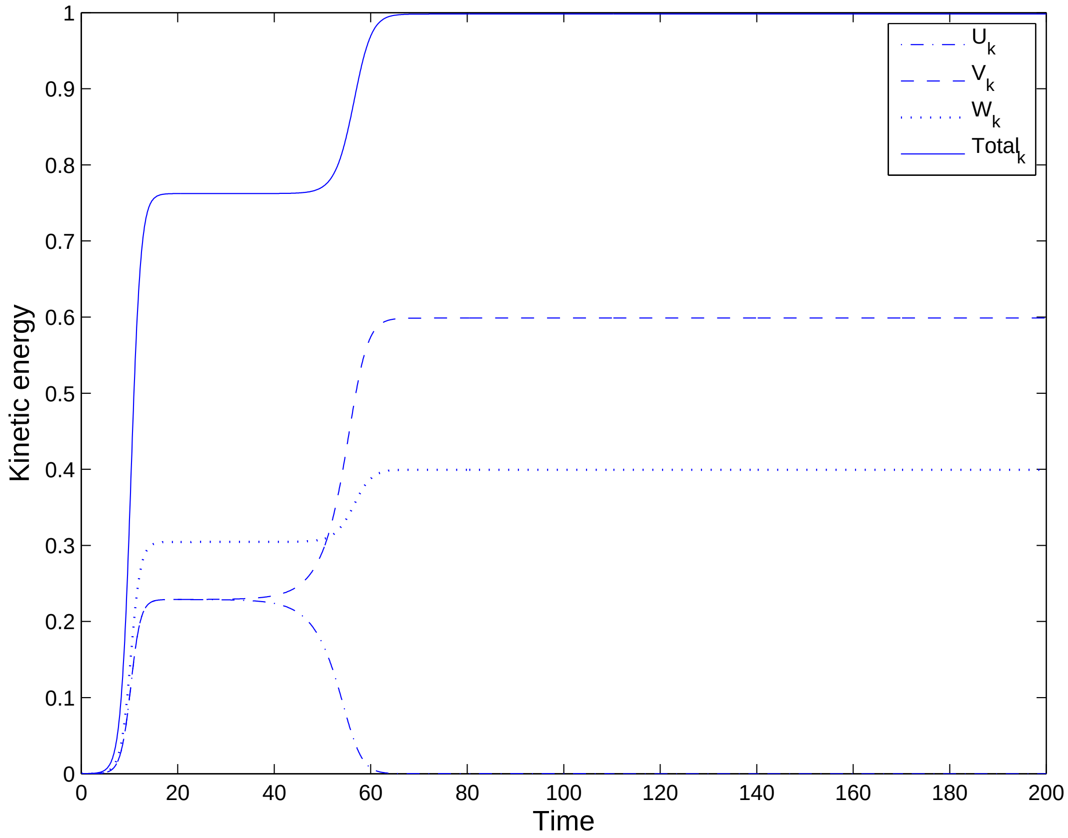

Figure 5.8: Kinetic energy evolution with time for steady two dimensional roll regime, Pr=0.71, Ra=2000, 16x16x16 resolution

5.1.2 TIME DEPENDENT EXPANSION COEFFICIENTS

Time dependent expansion coefficients $a^{(1,2)}$ represent the time evolution of the toroidal and poloidal components of the solenoidal convective motions, respectively. The first coefficient $a^{(1)}$ is absent in the steady two dimensional roll motion because it is associated with the basis $V^{(1)}$ that has no vertical velocity but contributes to the vertical vorticity. On the other hand $a^{(2)}$ is associated with the basis $V^{(2)}$ that has vertical velocity, but contributes none to vertical vorticity. Thus it is ever present in the convective motions because heat transport is associated with the correlations $< w\theta >$. That is why the motions associated with the first basis are parasitic in that they consume system energy but do not contribute to the heat transport.

The time evolution of the poloidal kinetic energy per modes are shown in 5.9 and in the steady roll motion regime (Figure 5.12) for $16x16x16$ resolution. After some initial transients, the energy in the toroidal modes all decays to zero . All the kinetic energy of the motion is carried by few of the poloidal modes in this regime 5.10 as indexed in Table 5.2. The horizontal wavenumber of the surviving modes vanishes $k_x = 0$ indicating the two dimensionality of the underlying motion. This decay for many orders of magnitude is an indication that the flow is well resolved. After the initial transients, the total kinetic energy in the toroidal and poloidal modes is shown to converge to their physically expected values in Figure 5.11 for steady two dimensional roll regime.

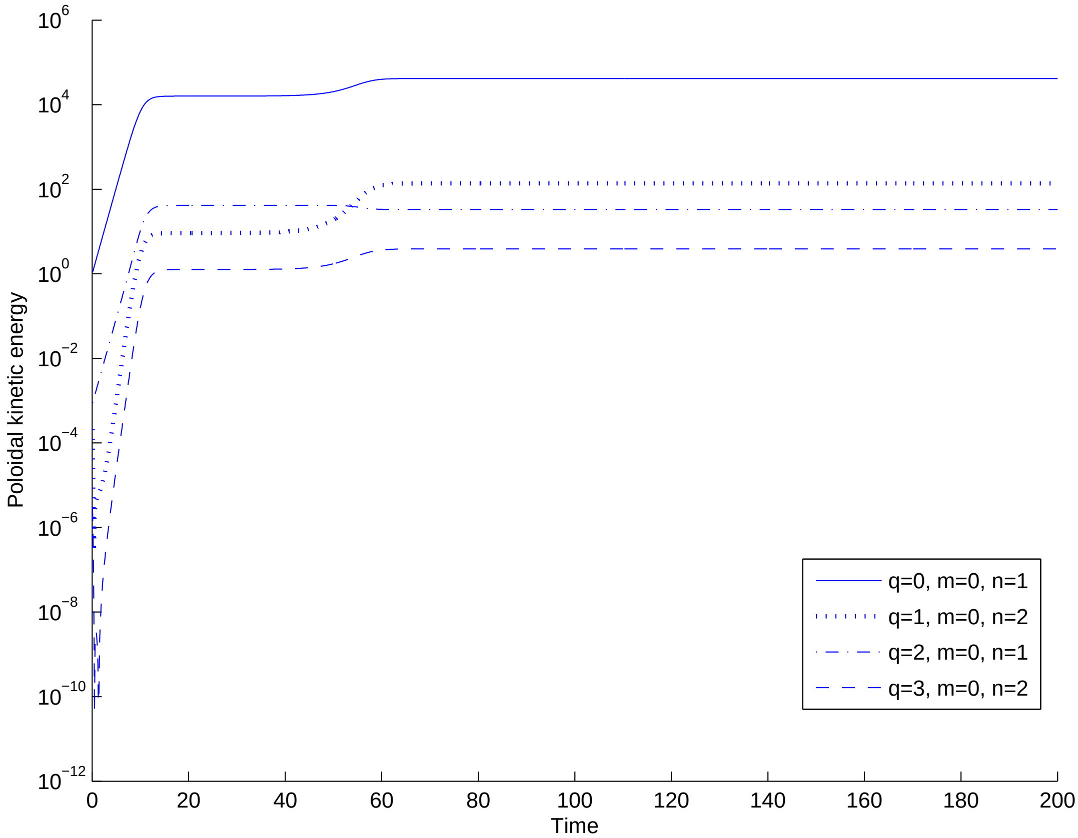

Figure 5.9: Most energetic four poloidal component for steady two dimensional roll regime, Pr=0.71, Ra=2000, 16x16x16 resolution.

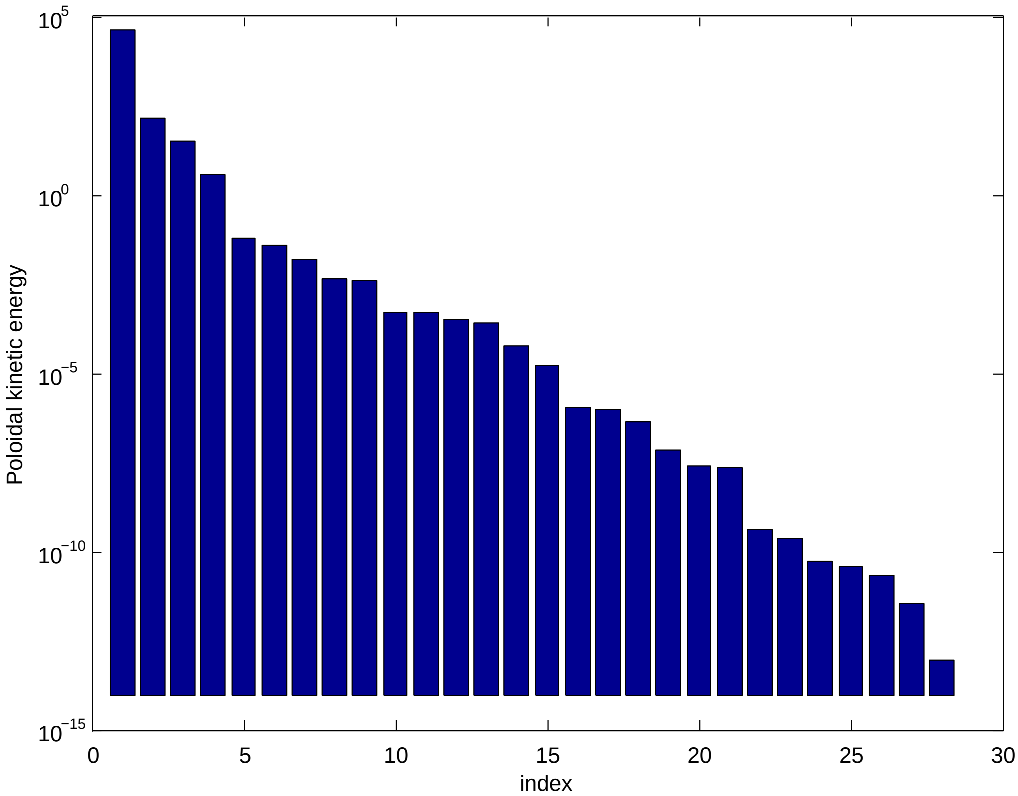

Figure 5.10: Poloidal kinetic energy of the surviving modes for steady two dimensional roll regime, Pr=0.71, Ra=2000, 16x16x16 resolution (table 5.2)

Table 5.2: Poloidal kinetic energy of the surviving modes for steady two dimensional roll regime, Pr=0.71, Ra=2000, 16x16x16 resolution. Here, the indices (p, m, n) are as appeared in equation (6.1)

Index	p	m	n
1	0	0	1
2	1	0	2
3	2	0	1
4	3	0	2
5	5	0	2
6	2	0	3
7	4	0	3
8	0	0	3
9	4	0	1
10	6	0	3
11	6	0	1
12	1	0	4
13	7	0	2
14	3	0	4
15	5	0	4
16	0	0	5
17	2	0	5
18	7	0	4
19	4	0	5
20	1	0	6
21	6	0	5
22	5	0	6
23	3	0	6
24	0	0	7
25	7	0	6
26	2	0	7
27	6	0	7
28	4	0	7

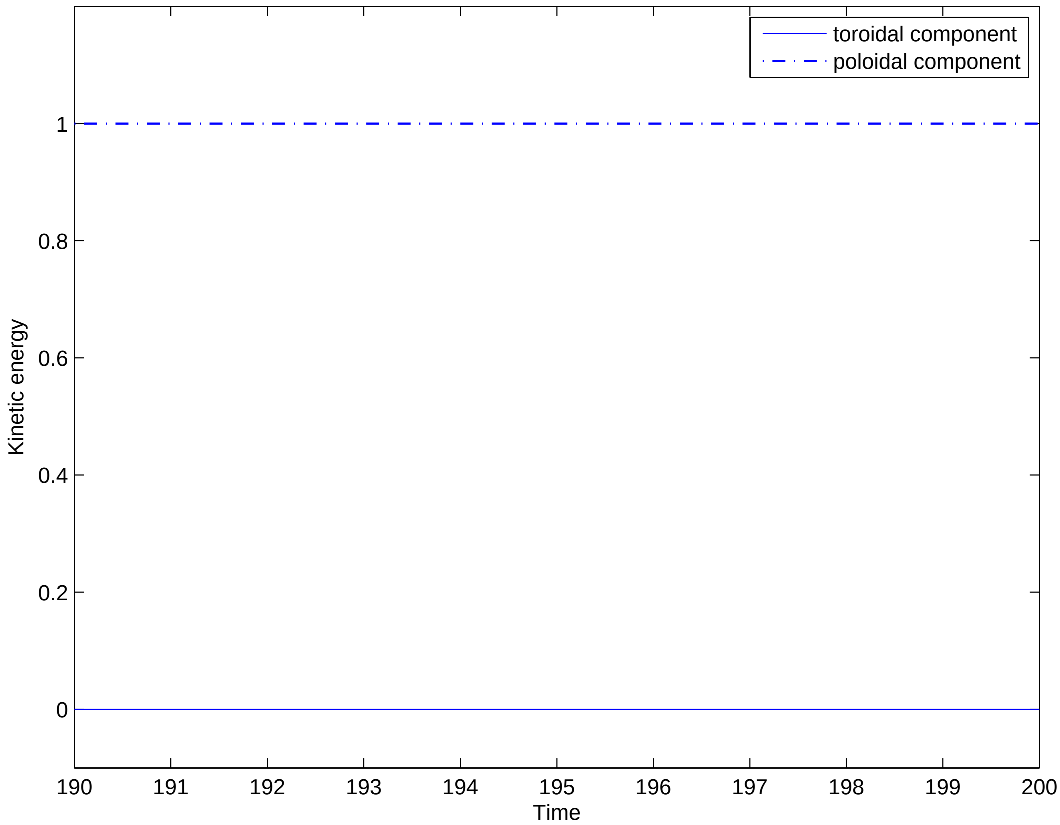

Figure 5.11: Energy variation of toroidal and poloidal kinetic energy for steady two dimensional roll regime, Pr=0.71, Ra=2000, 16x16x16 resolution

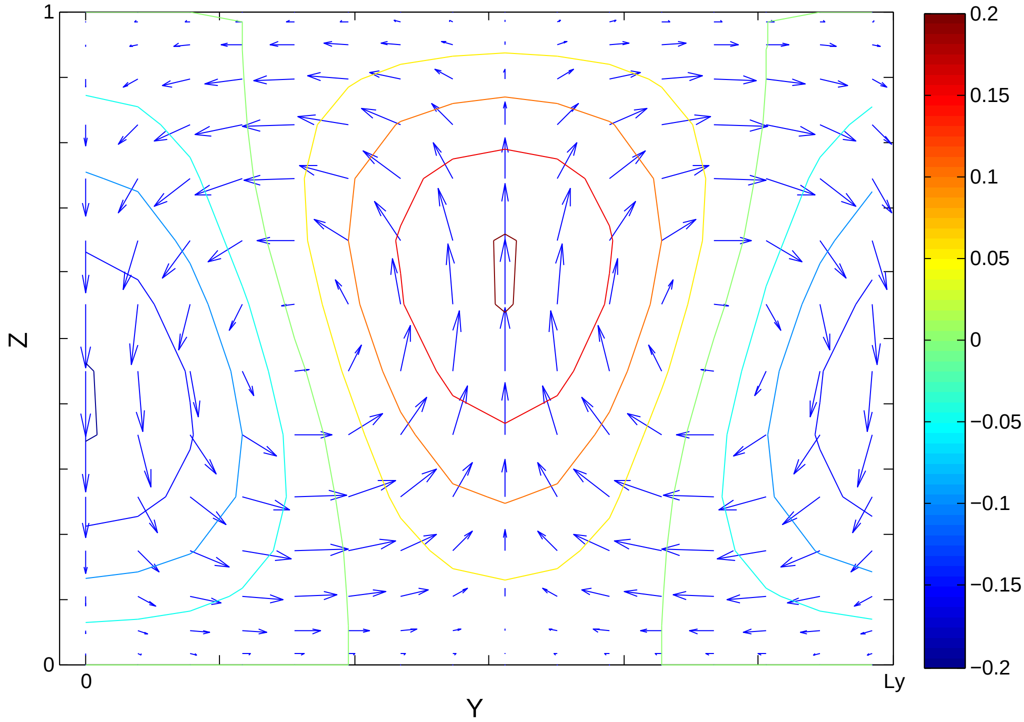

Figure 5.12: v-w velocity vector and temperature contour on Y-Z plane at steady two dimensional roll regime, Pr=0.71, Ra=2000, 16x16x16 resolution, $x = L_x/4$

As Rayleigh number is increased further, the flow goes through a Hopf bifurcation to a periodic regime. Periodic variation in the flow quantities of Nusselt number, velocity and temperature components are shown in Figures 5.13, 5.14, 5.15, 5.16 and 5.17 at various spatial locations in the convective box. While the motion in the boundary layer ($|z| = 0.98074$) is relatively slow, the activity increases as the boundary layer is exited towards the cell center. The discrete spikes in the power spectrum in Figures 5.18 and 5.19 are trademark of periodic motions. Nonlinear processes involved in the evolution of the motion cause the multiples of the fundamental frequency of oscillation to appear as many spikes in the spectrum.

Toroidal modes are activated in this regime. This is an indication of the three-dimensionality of the underlying motion as vertical vorticity appears in the flow as carried by the toroidal modes. This is in agreement with findings in literature that the start of periodic motions is observed to be associated with the appearance of vertical vorticity [1]. Even though many toroidal modes are activated in this regime, their total contribution to kinetic energy of motion is about %35 as shown in Figure 5.20. The kinetic energy content of the most energetic four toroidal and poloidal components are shown in Figures 5.21 and 5.22. The most energetic toroidal modes all appear to have $k_x \neq 0$, that is, they appear to be varying in the normal direction to the roll axis of the earlier steady regime. In the view of Figure 5.25, main roll motion is still present in this regime, thus, the motion associated with the energetic toroidal modes appear to represent the wave motion riding the rolls as observed in literature. The modal energy distribution in Figures 5.23 and 5.24 for the toroidal and poloidal modes show the sufficiency of the resolution by the drop of many order of magnitudes in energy content.

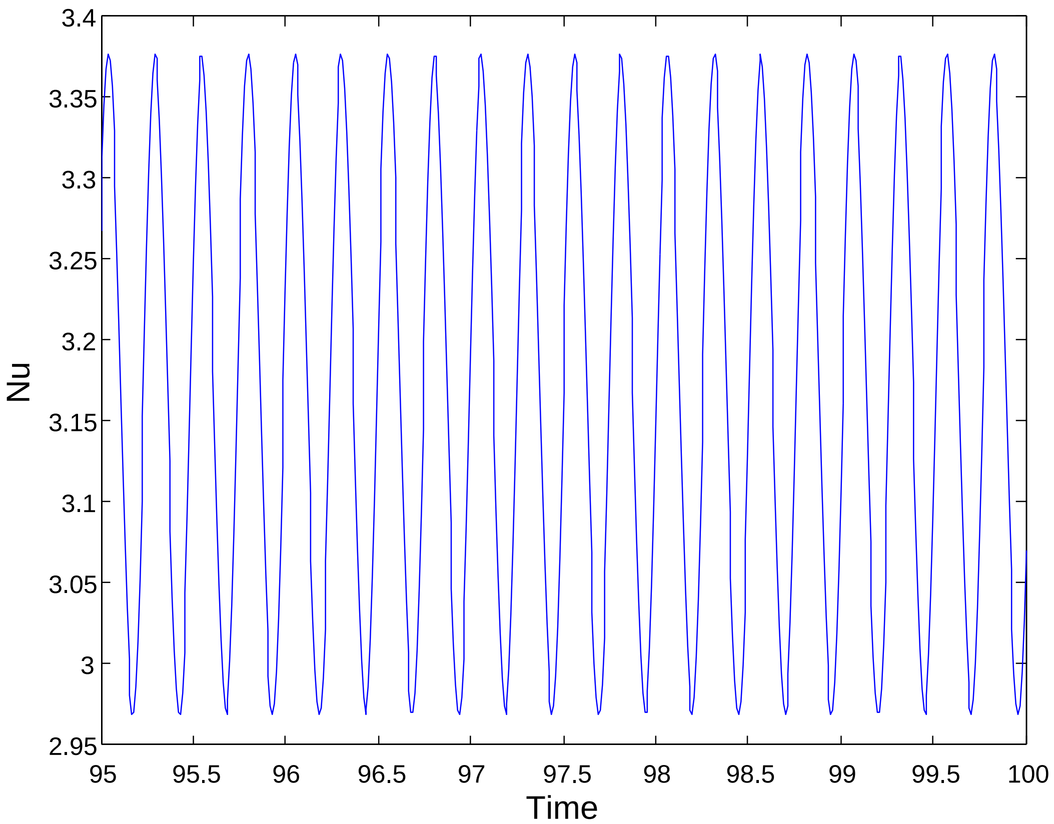

Figure 5.13: Nusselt variation at the periodic regime, Pr=0.71, Ra=20000, 16x16x20 resolution

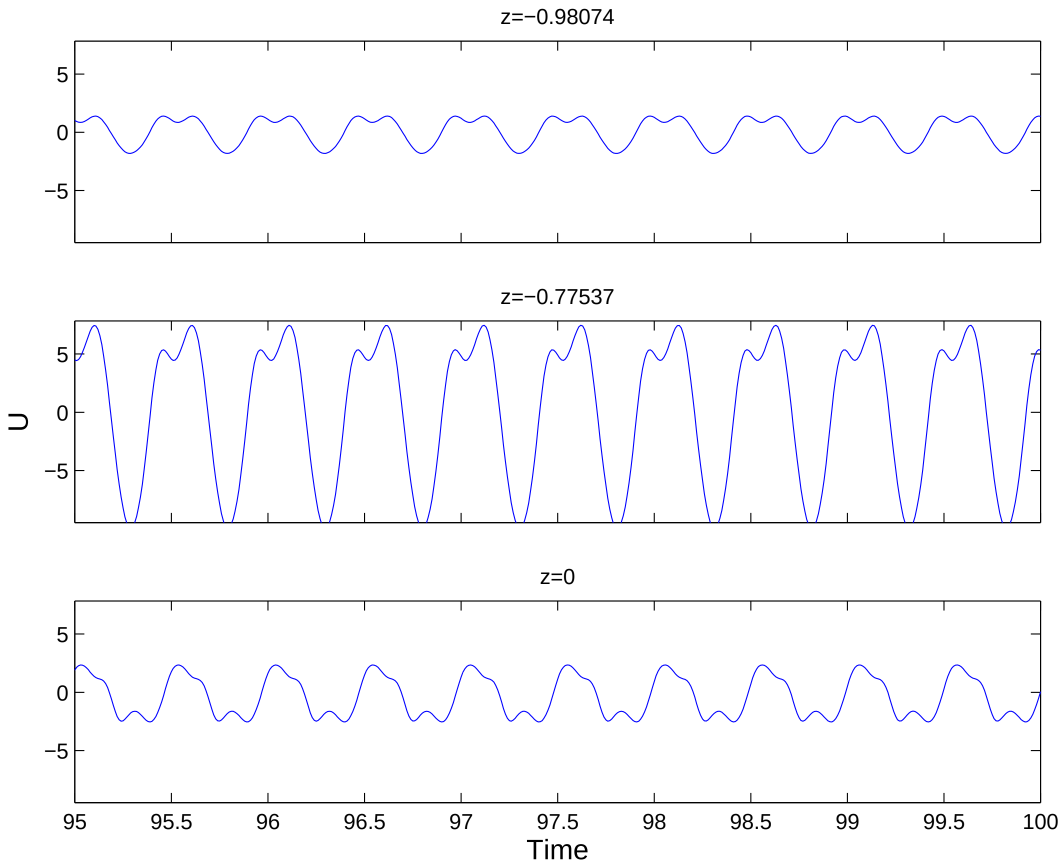

Figure 5.14: u component of velocity variation at the periodic regime, Pr=0.71, Ra=20000, 16x16x20 resolution, $x = L_x/4$, $y = L_y/4$

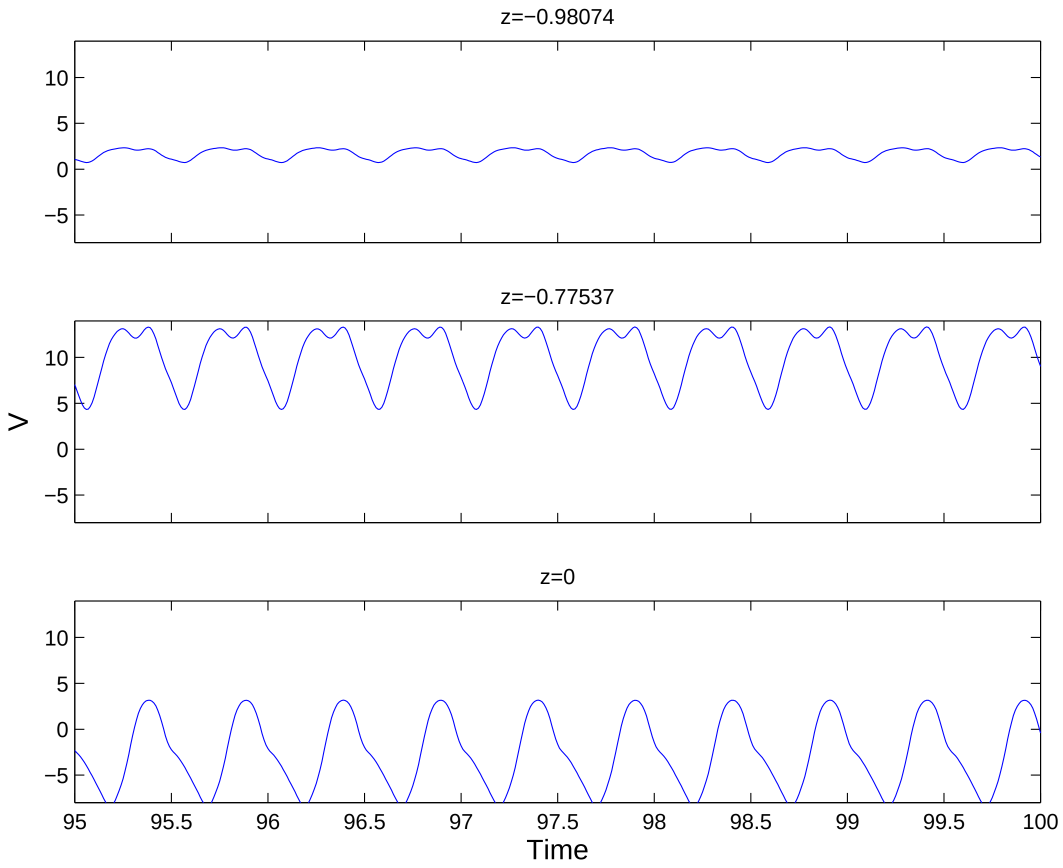

Figure 5.15: v component of velocity variation at the periodic regime, Pr=0.71, Ra=20000, 16x16x20 resolution, $x = L_x/4$, $y = L_y/4$

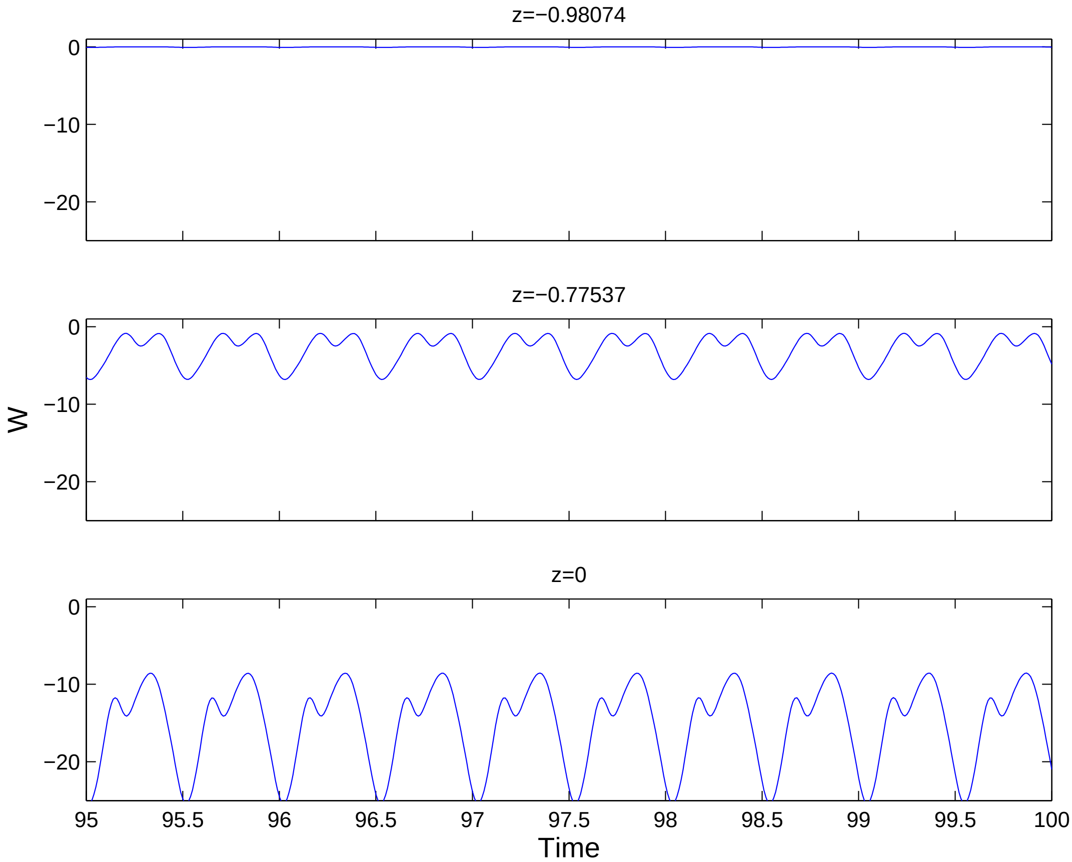

Figure 5.16: w component of velocity variation at the periodic regime, Pr=0.71, Ra=20000, 16x16x20 resolution, $x = L_x/4$, $y = L_y/4$

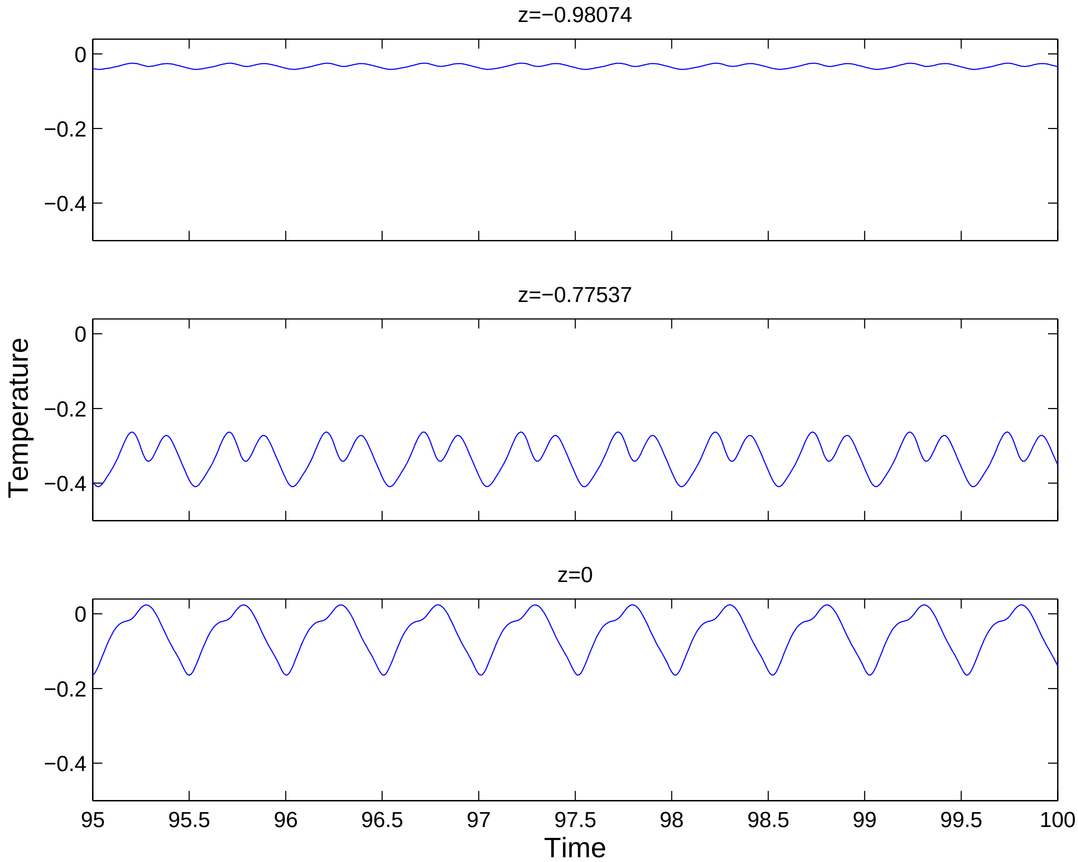

Figure 5.17: Temperature variation at the periodic regime, Pr=0.71, Ra=20000, 16x16x20 resolution, $x = L_x/4$, $y = L_y/4$

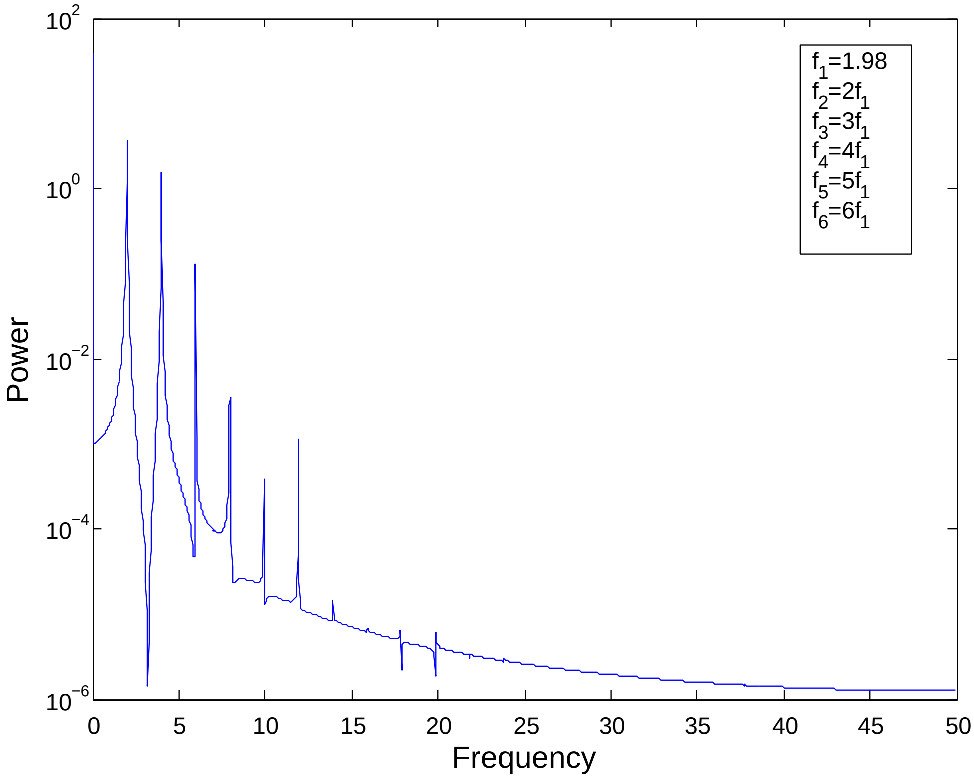

Figure 5.18: Power spectrum of w velocity at periodic regime, Pr=0.71, Ra=20000, 16x16x20 resolution, $z = -0.77537$, $x = L_x/4$, $y = L_y/4$

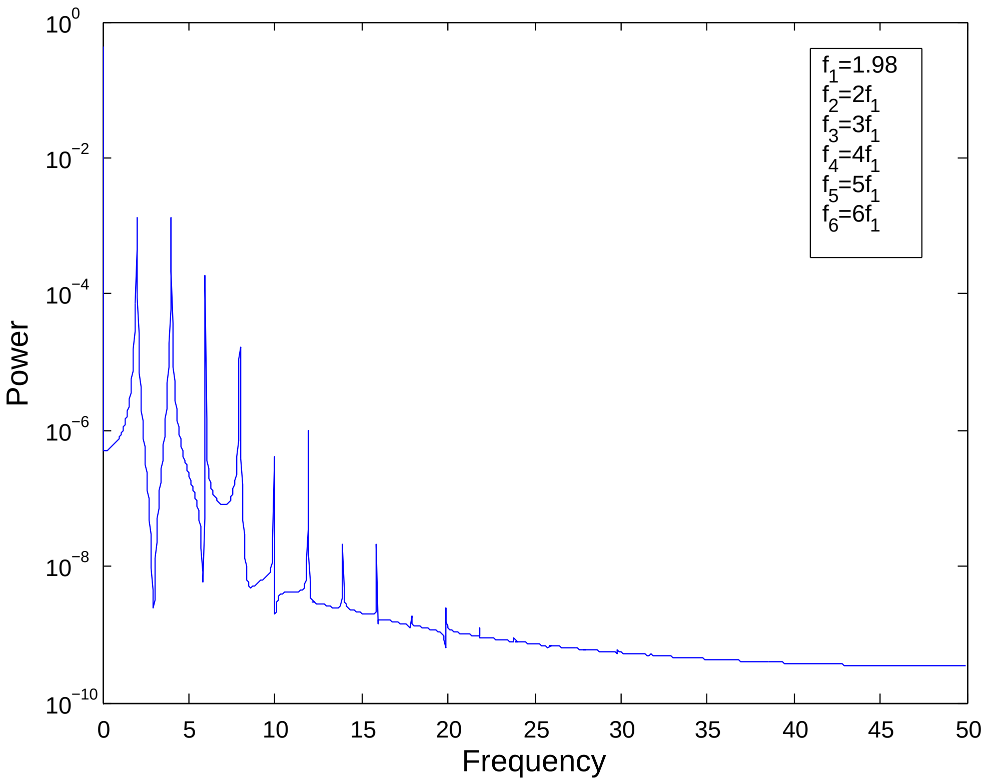

Figure 5.19: Power spectrum of temperature at periodic regime, Pr=0.71, Ra=20000, 16x16x20 resolution, $z = -0.77537$, $x = L_x/4$, $y = L_y/4$

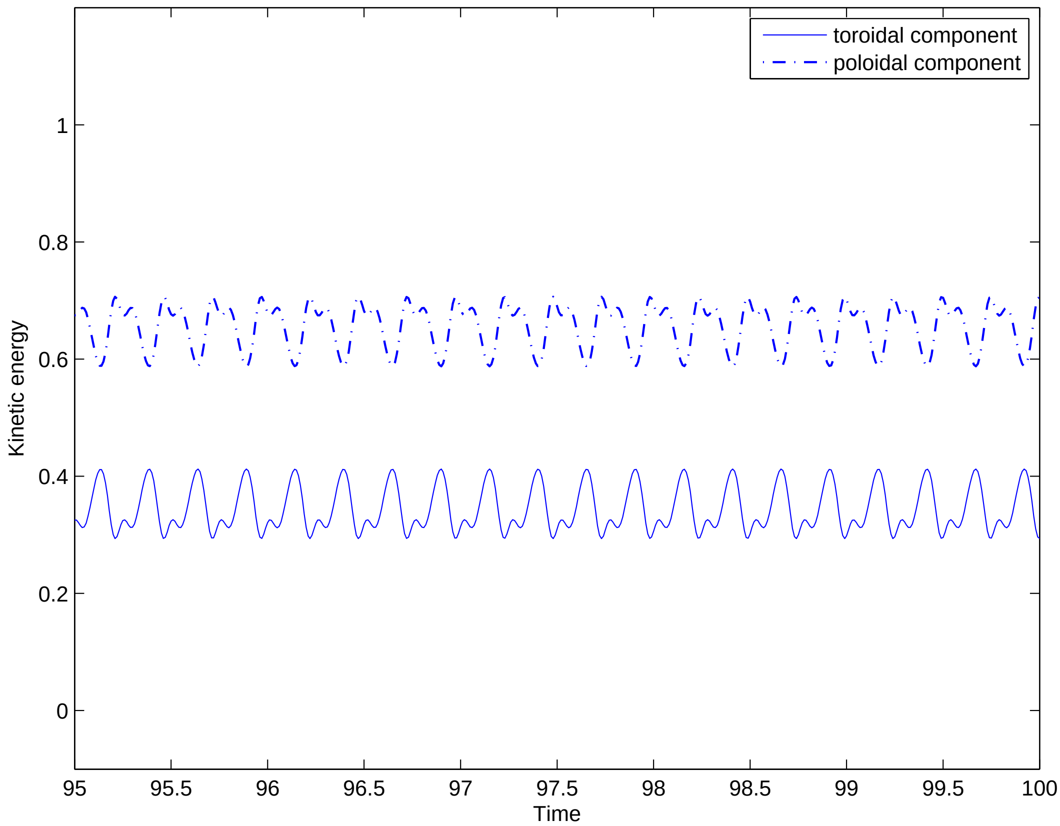

Figure 5.20: Kinetic energy variation of toroidal and poloidal components at the periodic regime, Pr=0.71, Ra=20000, 16x16x20 resolution

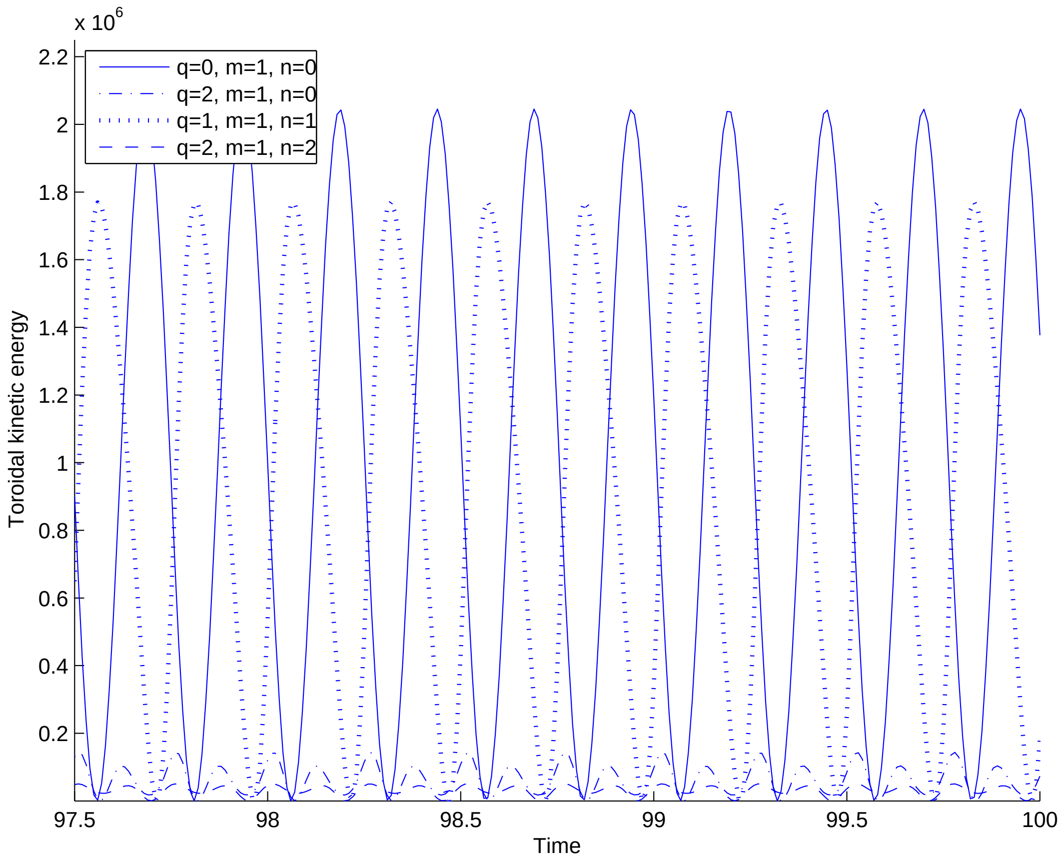

Figure 5.21: Most energetic four toroidal component for periodic regime, Pr=0.71, Ra=20000, 16x16x20 resolution

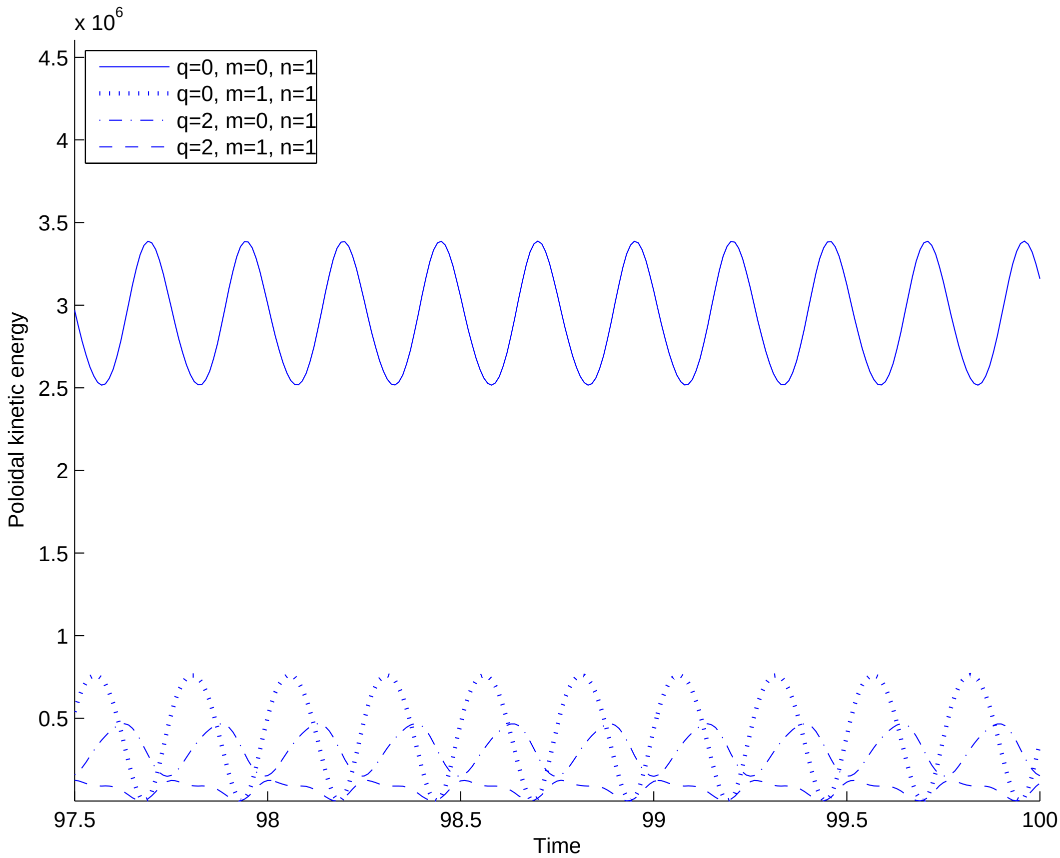

Figure 5.22: Most energetic four poloidal component for periodic regime, Pr=0.71, Ra=20000, 16x16x20 resolution

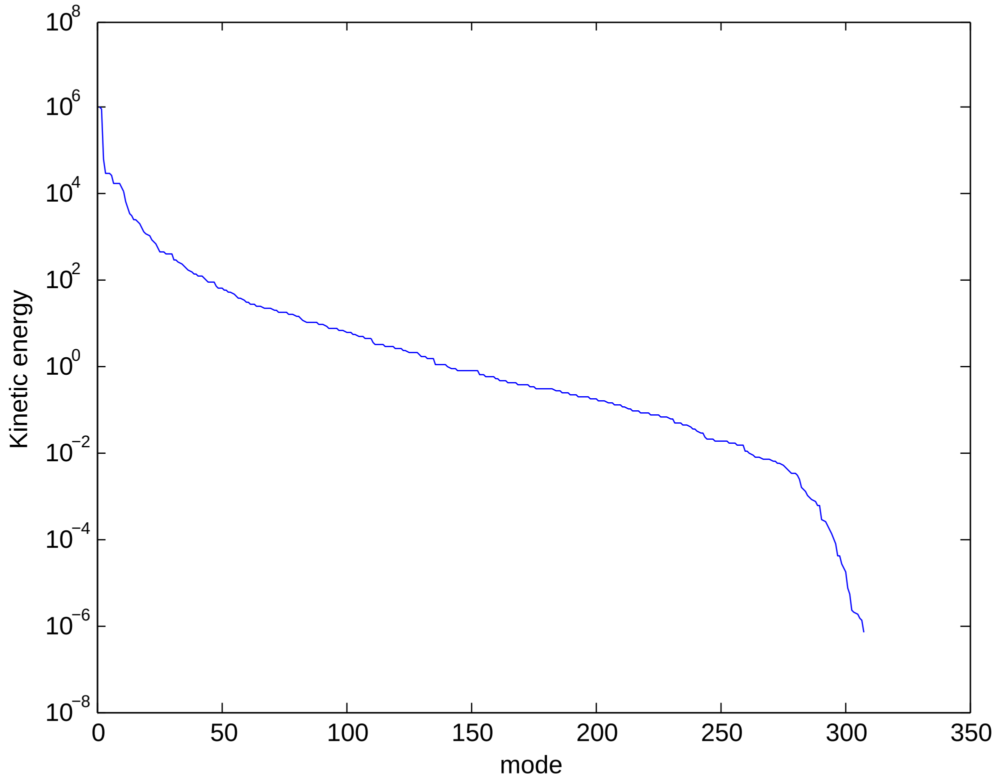

Figure 5.23: Toroidal kinetic energy distrubution for modes (q, m, n) of periodic regime, Pr=0.71, Ra=20000, 16x16x20 resolution

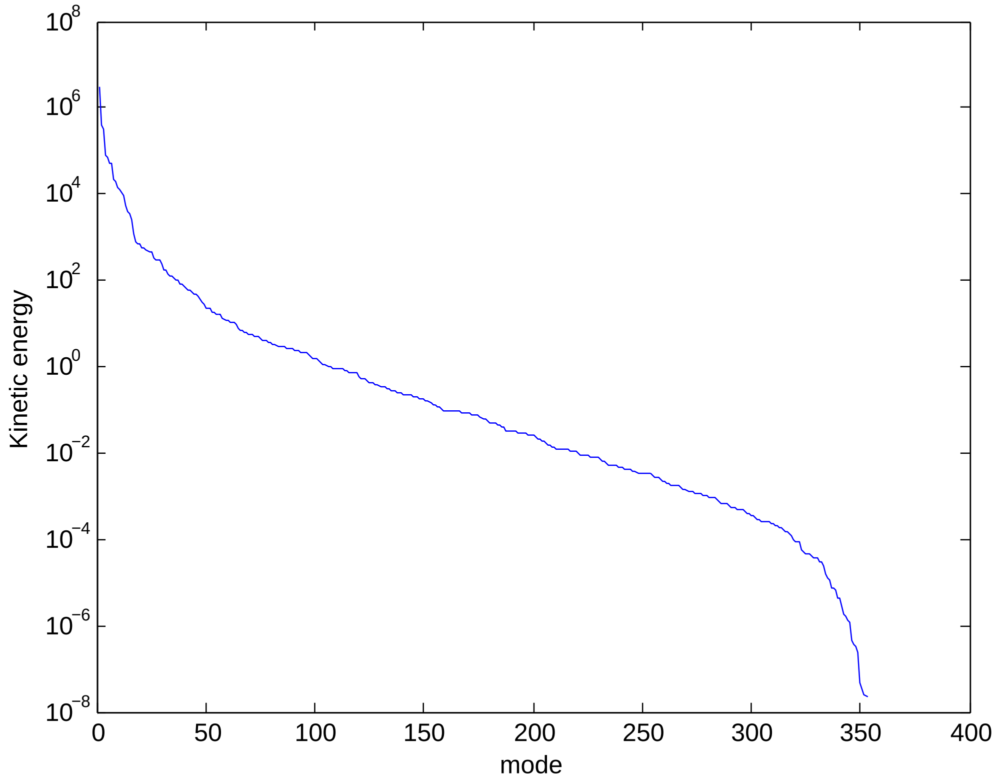

Figure 5.24: Poloidal kinetic energy distrubution for modes (q, m, n) of periodic regime, Pr=0.71, Ra=20000, 16x16x20 resolution

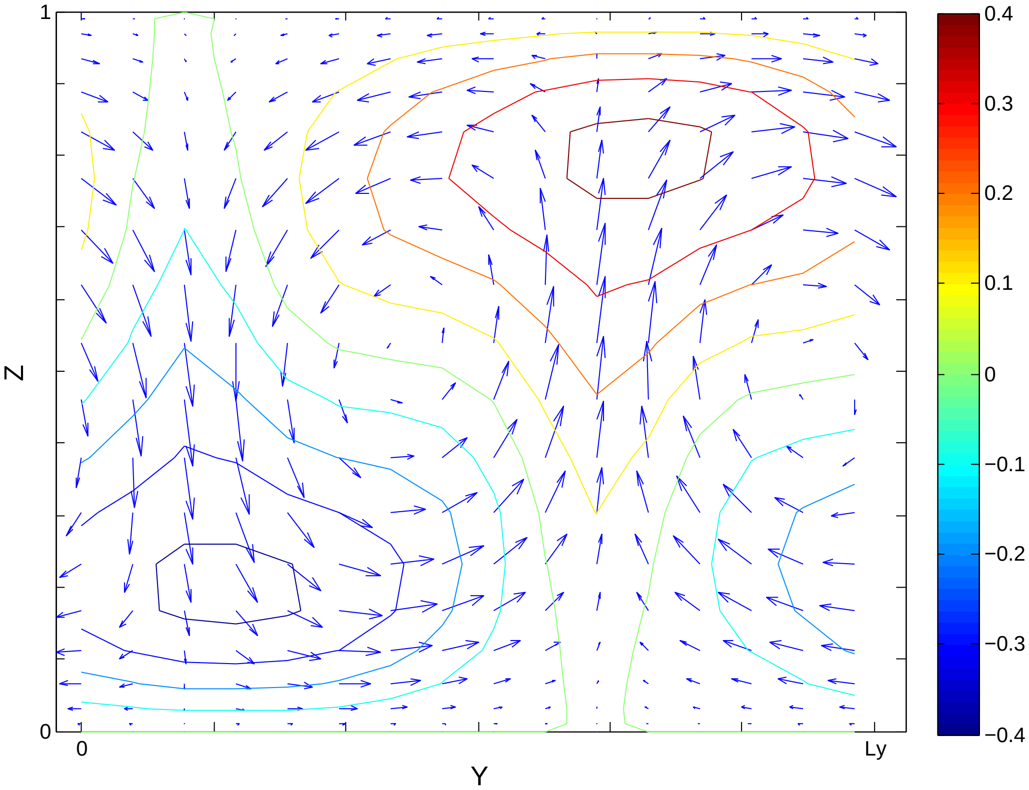

Figure 5.25: v-w velocity vector and temperature contour on Y-Z plane at periodic regime, Pr=0.71, Ra=20000, 16x16x20 resolution, $x = L_x/4$

Double periodic regime occurs as Rayleigh number is increased past the range corresponding to the periodic regime. It is characterized by two incommensurate oscillation frequencies present in the motion. This is shown in Figures 5.28 and 5.29. Double periodic oscillations can be seen in Figures 5.30, 5.31, 5.32, 5.33 and 5.34 depicting the time series evolution of various flow quantities at three spatial locations in the vertical. It is observed in [56] in the KL analysis of thermal convection between free surfaces that the second frequency is associated with the release of the thermals from the boundary layer. The thermal in the form of a local eddy may be identified in Figure 5.27 in the presence of the roll motion which is still present in this regime (see figure 5.26).

The modal kinetic energy distribution in Figures 5.35 and 5.36 for the toroidal and poloidal modes show the sufficiency of the resolution by the drop of many order of magnitudes in energy content. More modes are involved in carrying the kinetic energy in this regime. This indicates that the underlying dynamics in the double-periodic regime is more complicated and involves smaller scales. The appearance of small scales helps to dissipate the excess energy in the system. Poloidal kinetic energy seems to increase in this regime in comparison to the earlier periodic regime in the expense of a decrease in the toroidal kinetic energy as shown in Figure 5.37. Since toroidal components of the flow are parasitic with their vanishing vertical velocity, the transition to the double periodic regime acts towards an enhancement in the heat transport.

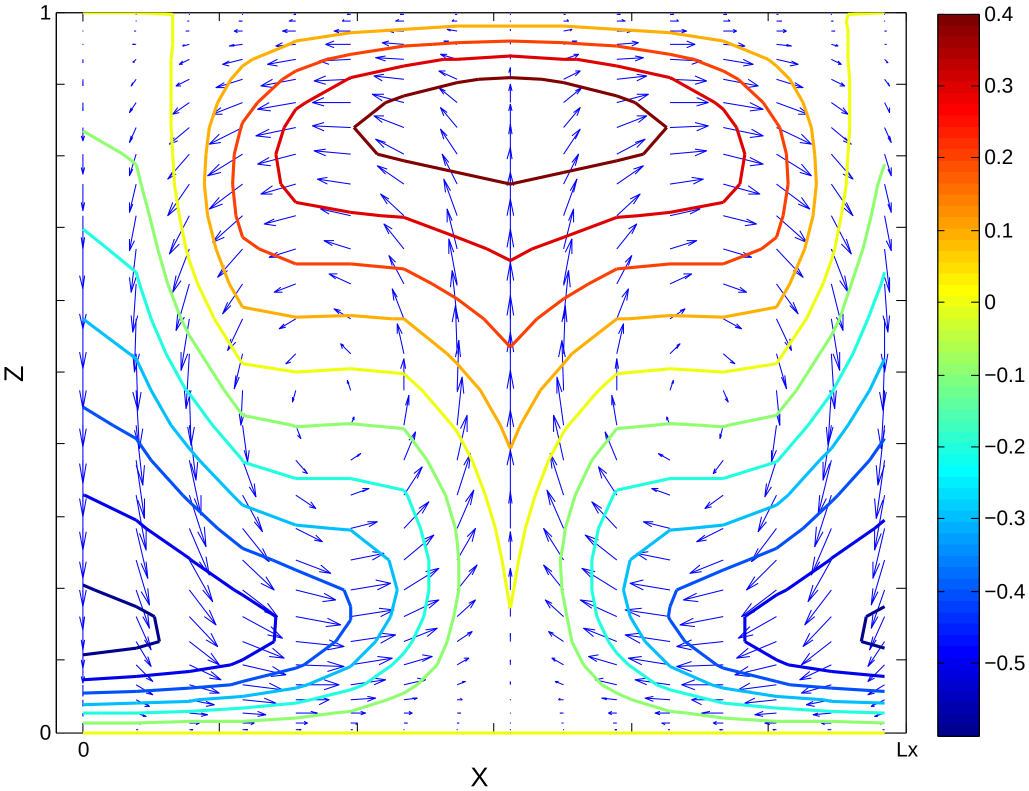

Figure 5.26: u-w velocity vector and temperature contour on X-Z plane at double periodic regime, Pr=0.71, Ra=50000, 16x16x32 resolution, $y = L_y/4$

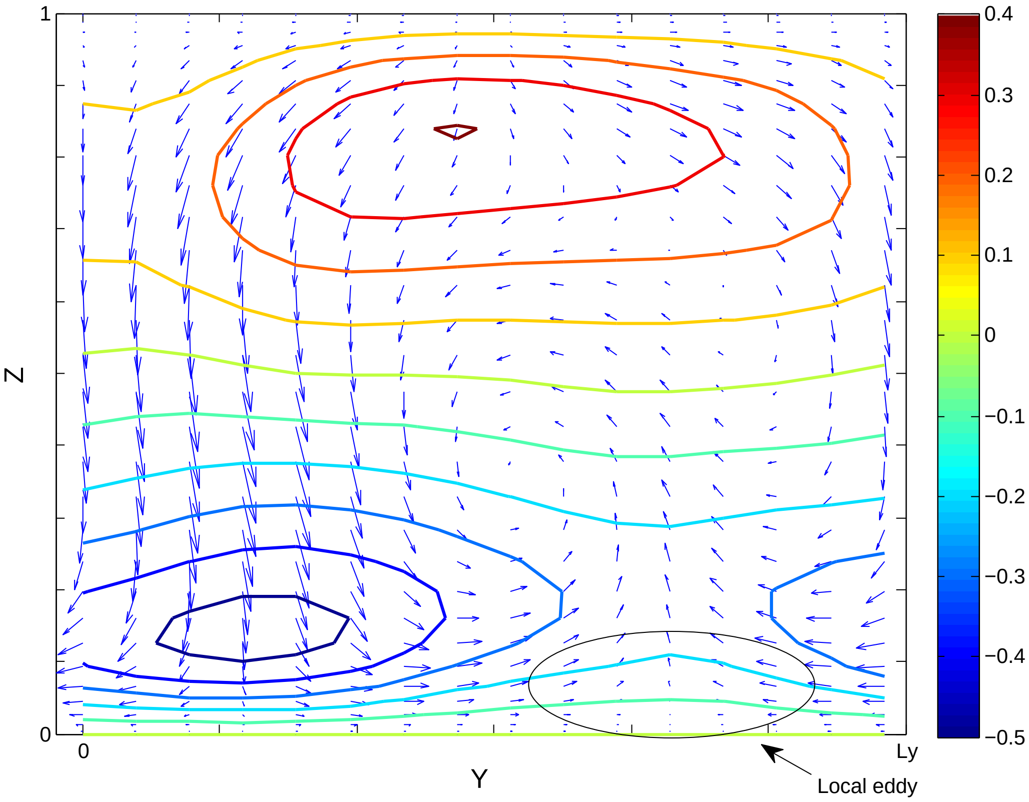

Figure 5.27: v-w velocity vector and temperature contour on Y-Z plane at double periodic regime, Pr=0.71, Ra=50000, 16x16x32 resolution, $x = L_x/4$

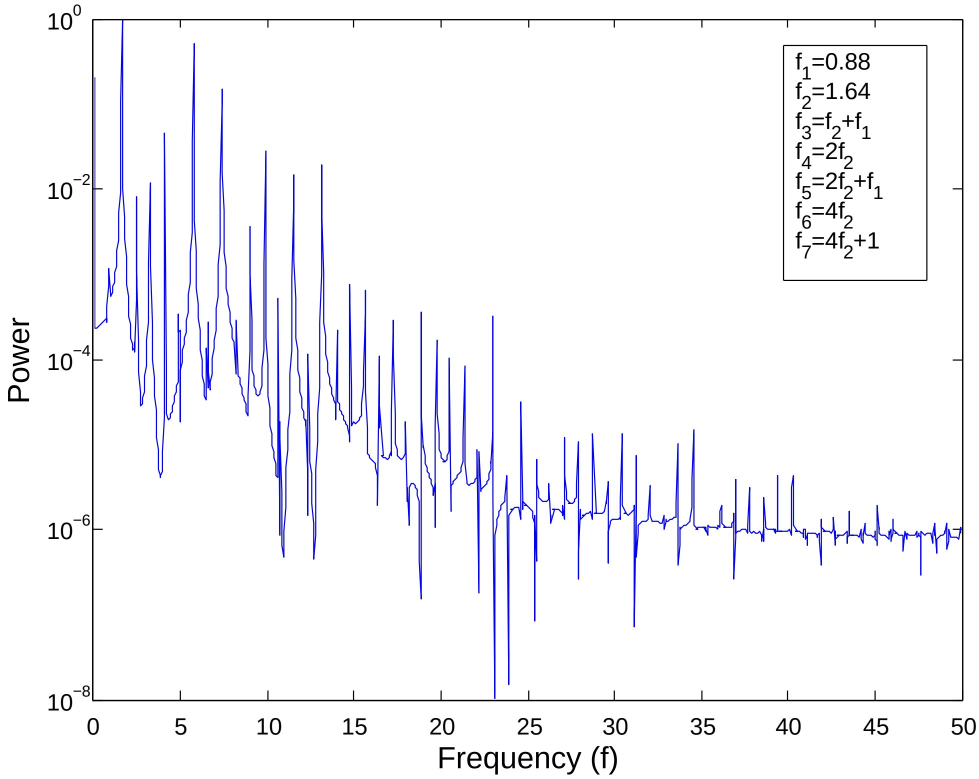

Figure 5.28: Power spectrum of w velocity at double periodic regime, Pr=0.71, Ra=50000, 16x16x32 resolution, $z = -0.91185$, $x = L_x/4$, $y = L_y/4$

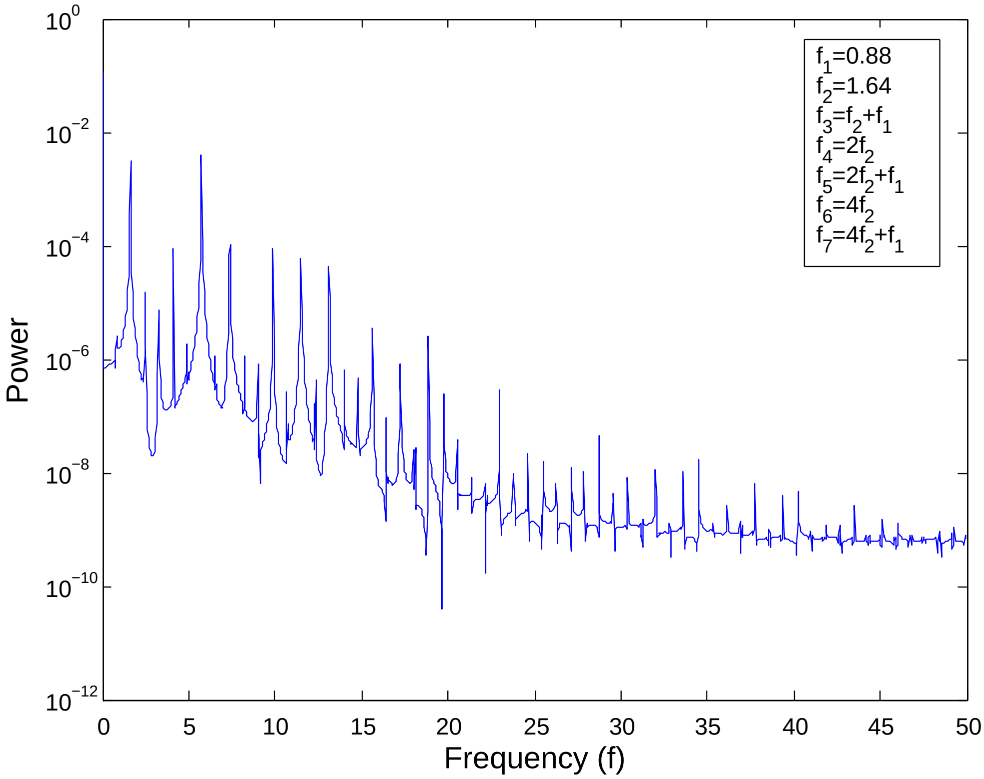

Figure 5.29: Power spectrum of temperature at double periodic regime, Pr=0.71, Ra=50000, 16x16x32 resolution, $z = -0.91185$, $x = L_x/4$, $y = L_y/4$

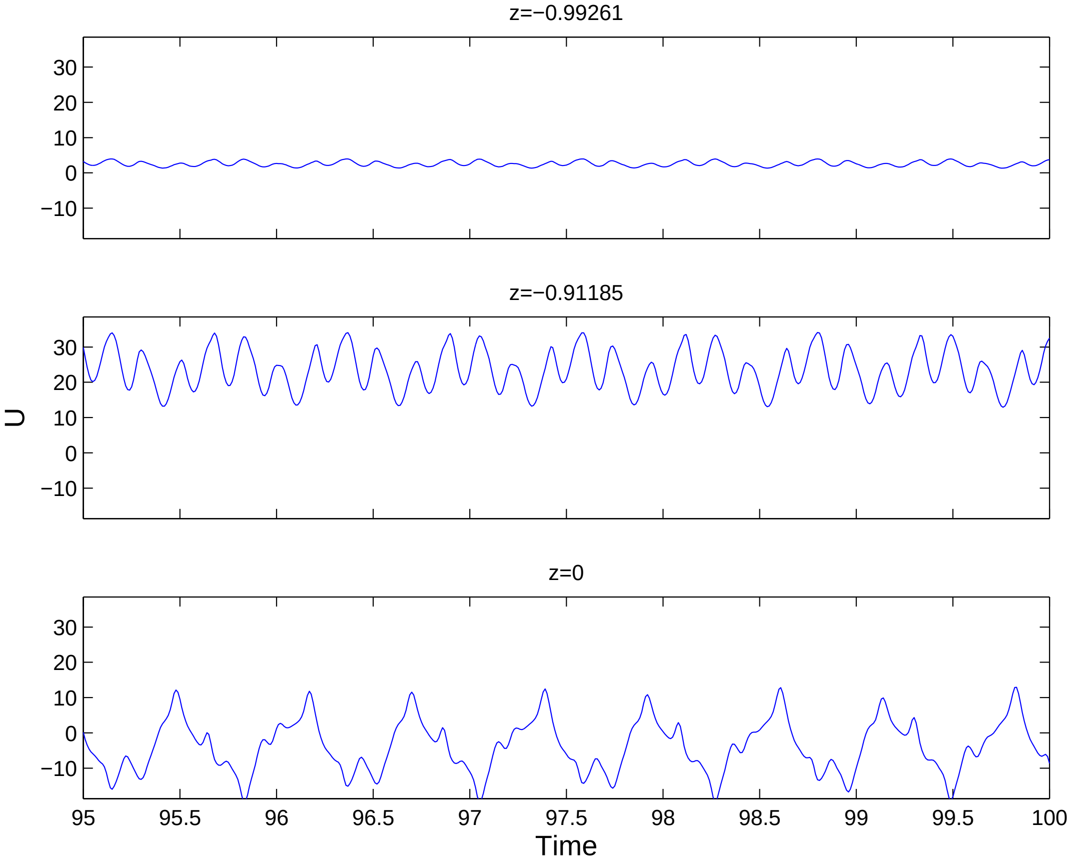

Figure 5.30: u component of velocity variation at the double periodic regime, Pr=0.71, Ra=50000, 16x16x32 resolution, $x = L_x/4$, $y = L_y/4$

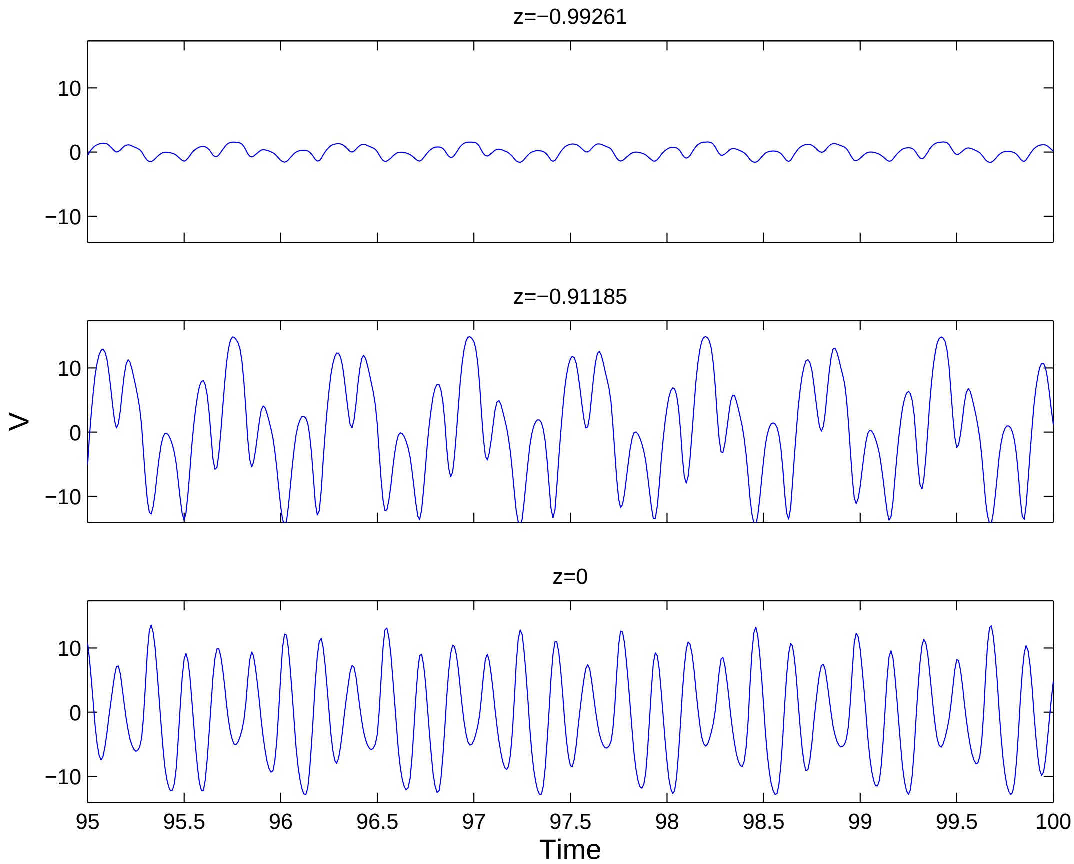

Figure 5.31: v component of velocity variation at the double periodic regime, Pr=0.71, Ra=50000, 16x16x32 resolution, $x = L_x/4$, $y = L_y/4$

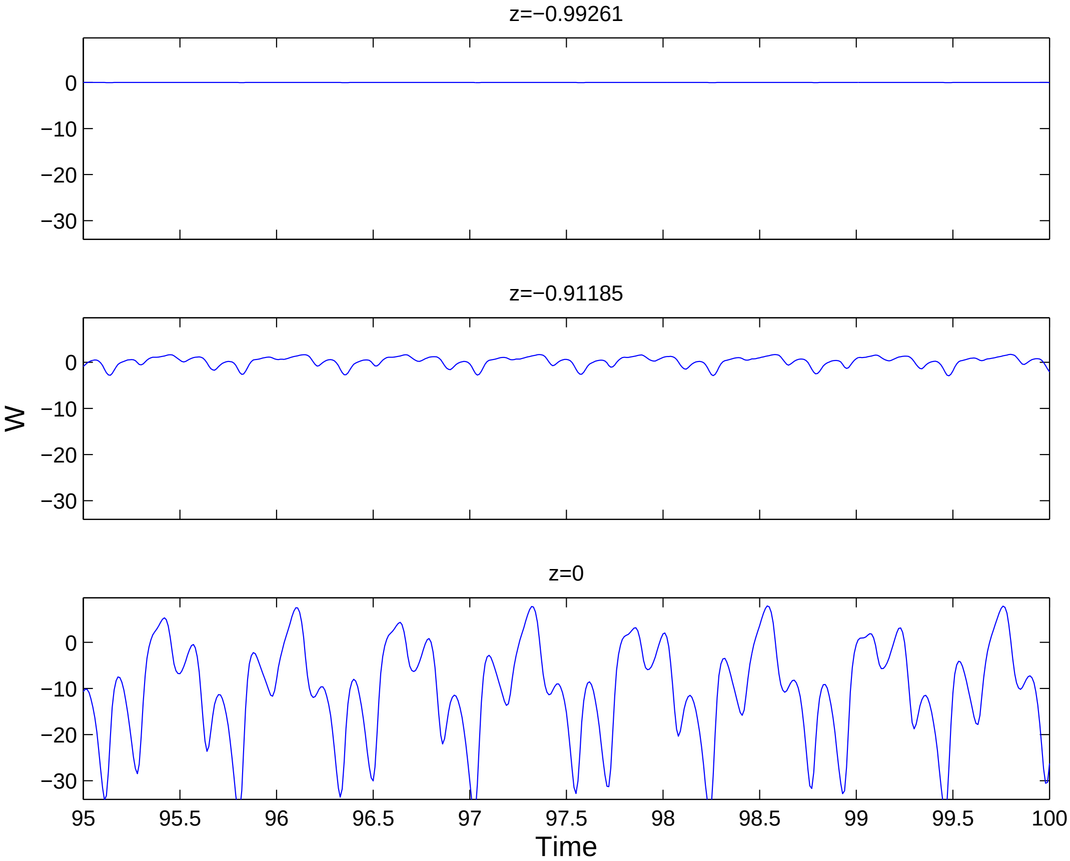

Figure 5.32: w component of velocity variation at the double periodic regime, Pr=0.71, Ra=50000, 16x16x32 resolution, $x = L_x/4$, $y = L_y/4$

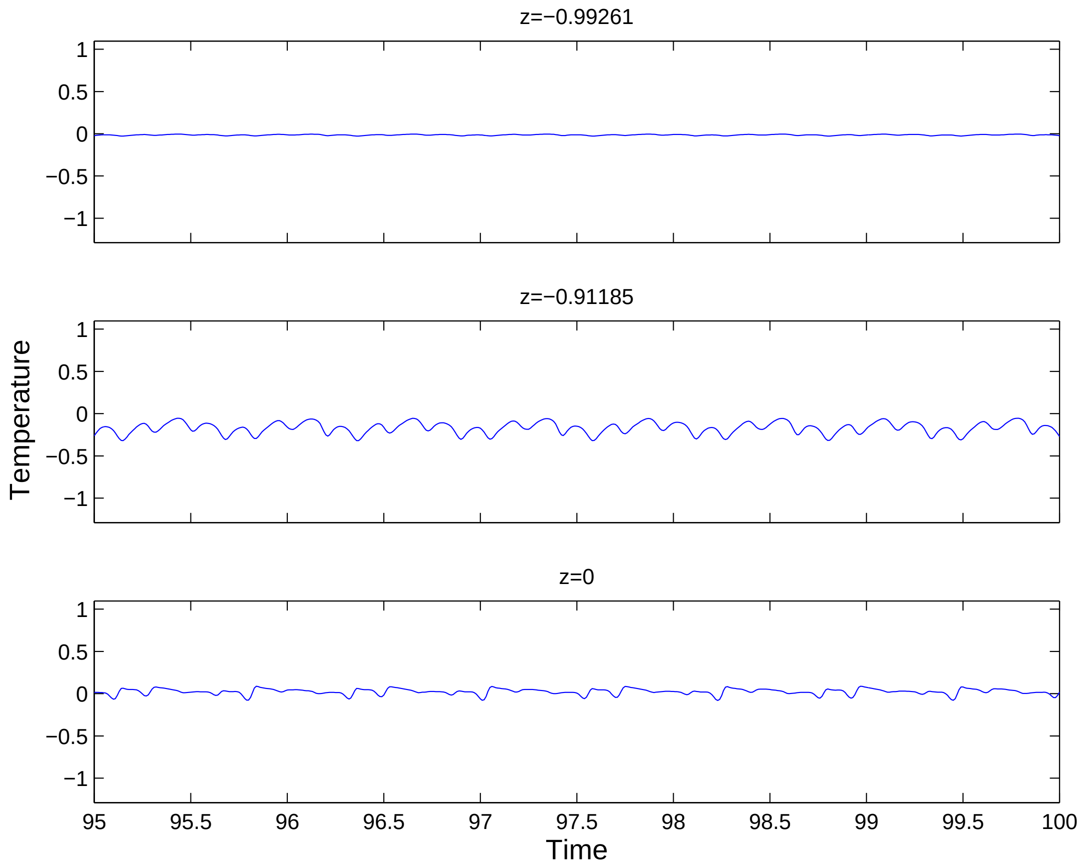

Figure 5.33: Temperature variation at the double periodic regime, Pr=0.71, Ra=50000, 16x16x32 resolution, $x = L_x/4$, $y = L_y/4$

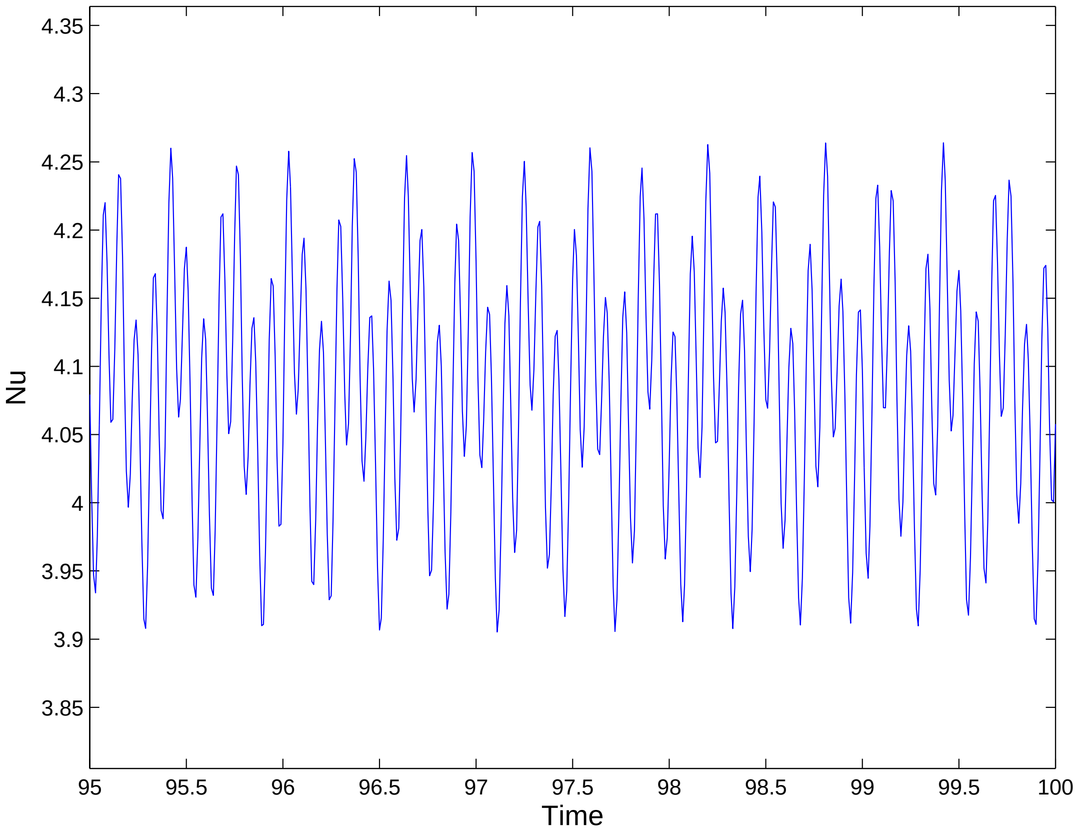

Figure 5.34: Nusselt variation at the double periodic regime, Pr=0.71, Ra=50000, 16x16x32 resolution

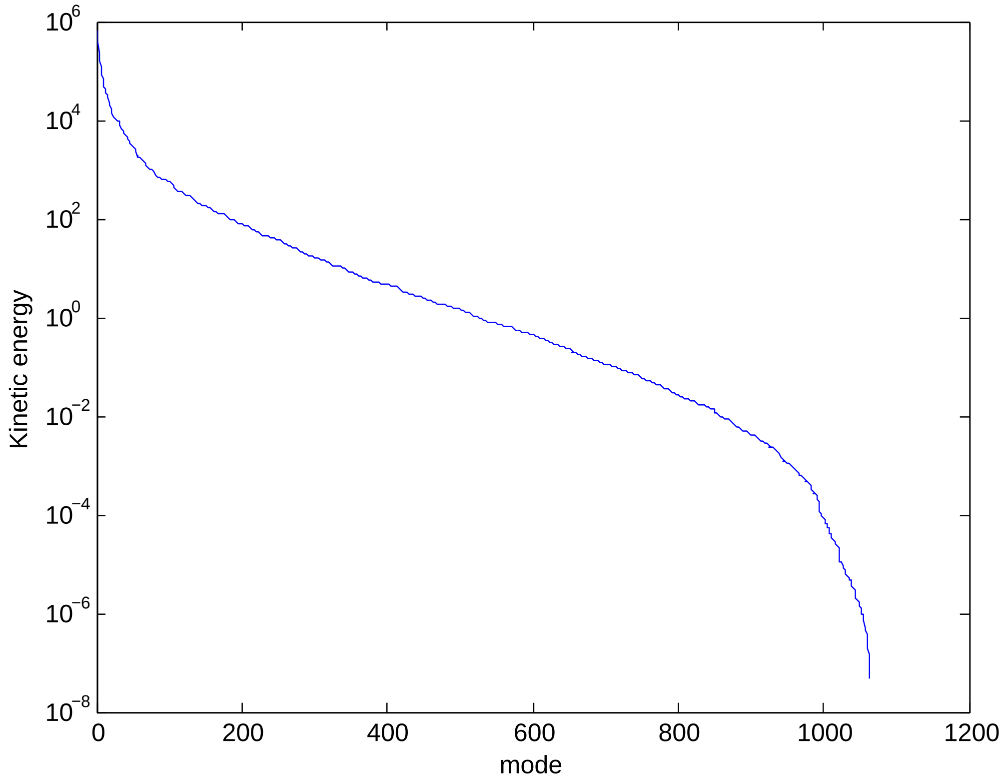

Figure 5.35: Toroidal kinetic energy distrubution for modes (q, m, n) of double periodic regime, Pr=0.71, Ra=50000, 16x16x32 resolution

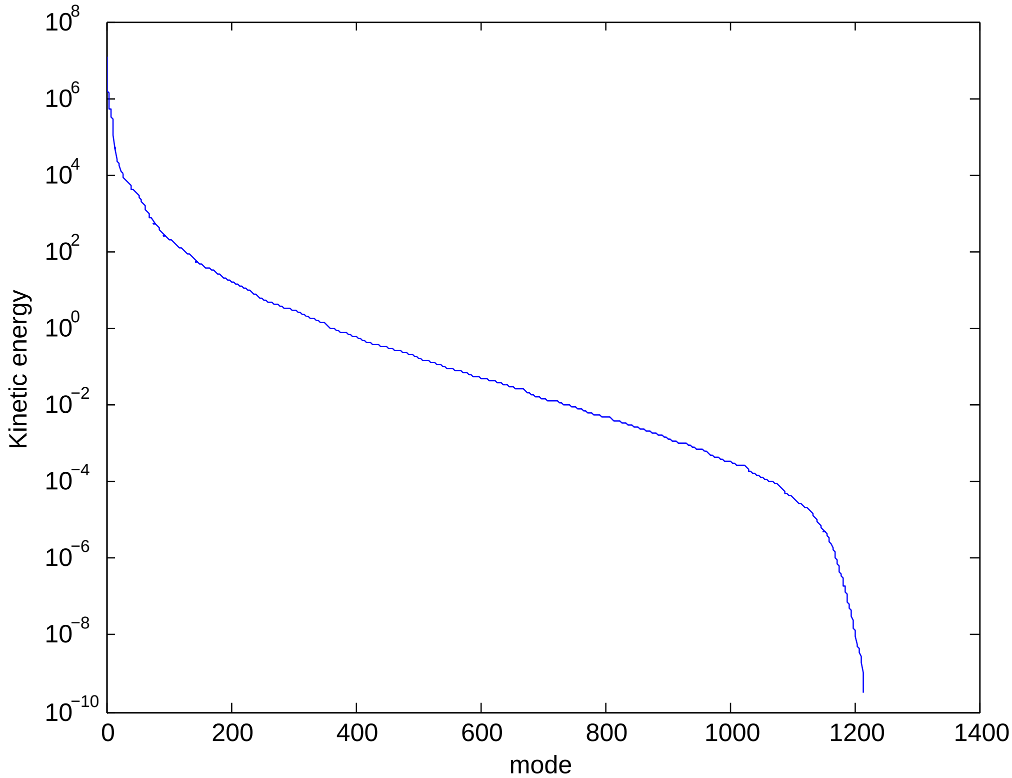

Figure 5.36: Poloidal kinetic energy distrubution for modes (q, m, n) of double periodic regime, Pr=0.71, Ra=50000, 16x16x32 resolution

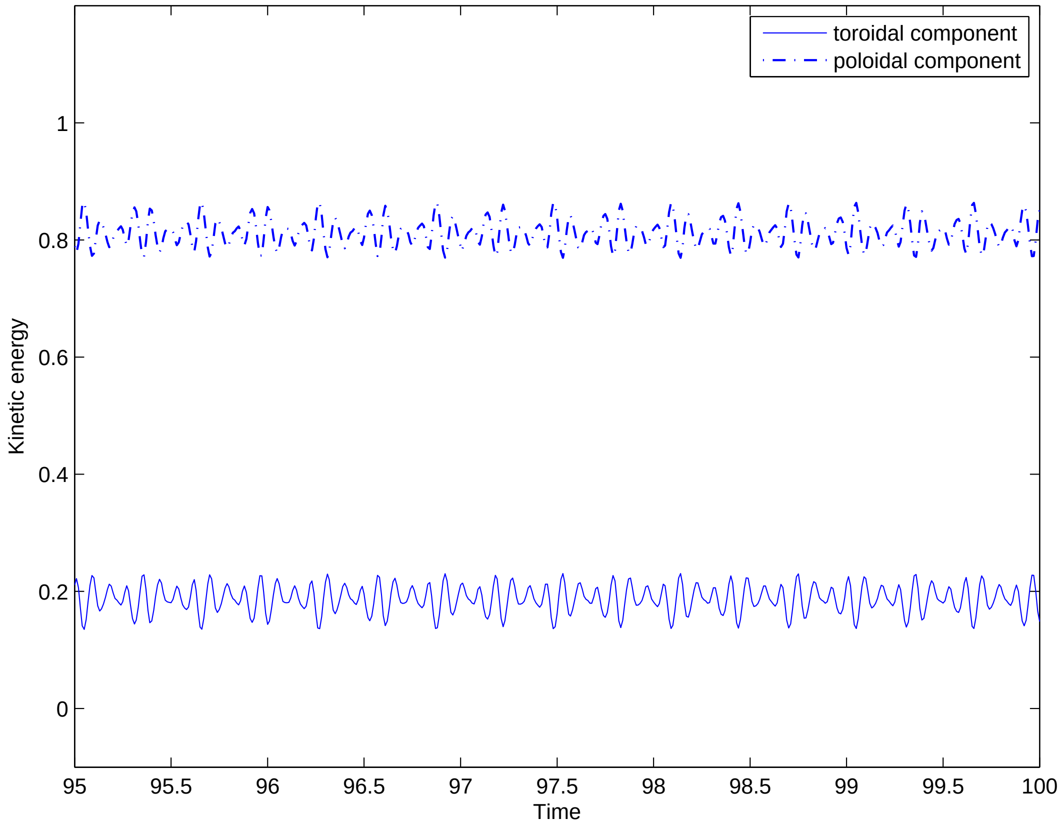

Figure 5.37: Kinetic energy variation of toroidal and poloidal components at the double periodic regime, Pr=0.71, Ra=50000, 16x16x32 resolution

CHAPTER 6

ROTATING RAYLEIGH-BÉNARD CONVECTION

In this chapter, the effect of rotation on Rayleigh Bénard convection is investigated. The governing equations, presented in chapter §2, are used for the linear stability analysis and nonlinear numerical simulation of rotating Rayleigh Bénard convection. Due to the geometrical reasons, just the effect of the coriolis force is considered, while the centrifugal force is neglected.

Solenoidal bases, constructed in chapter §4, are used to represent the solenoidal flow field in the form

$$\mathbf{u} = \sum_{|m|\leq N_x/2} \sum_{|n|\leq N_y/2} e^{ik_x x + ik_y y} \sum_{p=0}^{Q} \left(a_p^{(1)} \hat{V}_p^{(1)}(z) + a_p^{(2)} \hat{V}_p^{(2)}(z) \right), \tag{6.1}$$

with

$$\theta = \sum_{|m|\leq N_x/2} \sum_{|n|\leq N_y/2} e^{ik_x x + ik_y y} \sum_{p=0}^{Q} b_p \hat{T}_p(z), \tag{6.2}$$

which are subsequently substituted into the governing equations (2.21) and (2.22), to yield the residuals

$$\begin{aligned} R_{\mathbf{u}} &= -\frac{\partial \mathbf{u}}{\partial t} - (\mathbf{u} \cdot \nabla)\,\mathbf{u} - \nabla p + PrRa_h \theta e_z + Pr\nabla^2 \mathbf{u} - 2Pr\Omega e_z \times \mathbf{u}, \\ R_\theta &= -\frac{\partial \theta}{\partial t} - (\mathbf{u} \cdot \nabla)\,\theta - \frac{w}{2} + \nabla^2 \theta. \end{aligned}$$

The projection of these residuals onto the dual space spanned by $\bar{V}_p^{(1)}$, $\bar{V}_p^{(2)}$ and $\bar{T}_p$ ($= \hat{T}_p$) is annuled, as explained in §4.1,

$$\left(\bar{V}, R_{\mathbf{u}}\right) = 0, \quad \left(\bar{T}, R_\theta\right) = 0,$$

to get

$$\begin{pmatrix} \left(\bar V^{(1)}, \hat V^{(1)}\right) & \left(\bar V^{(1)}, \hat V^{(2)}\right) \\ \left(\bar V^{(2)}, \hat V^{(1)}\right) & \left(\bar V^{(2)}, \hat V^{(2)}\right) \end{pmatrix} \begin{pmatrix} \dot a^{(1)} \\ \dot a^{(2)} \end{pmatrix} + \begin{pmatrix} c^{(1)} \\ c^{(2)} \end{pmatrix} =$$

$$PrRa_h \begin{pmatrix} \left(\bar V^{(1)}, \hat T e_z\right) \\ \left(\bar V^{(2)}, \hat T e_z\right) \end{pmatrix} \begin{pmatrix} b \\ b \end{pmatrix} + Pr \begin{pmatrix} \left(\bar V^{(1)}, (\nabla^2 - 2\Omega e_z)\hat V^{(1)}\right) & \left(\bar V^{(1)}, (\nabla^2 - 2\Omega e_z)\hat V^{(2)}\right) \\ \left(\bar V^{(2)}, (\nabla^2 - 2\Omega e_z)\hat V^{(1)}\right) & \left(\bar V^{(2)}, (\nabla^2 - 2\Omega e_z)\hat V^{(2)}\right) \end{pmatrix} \begin{pmatrix} a^{(1)} \\ a^{(2)} \end{pmatrix},$$

$$\left(\bar T, \hat T\right) \dot b + d = \left(\bar T, \hat V^{(1)} \cdot e_z\right) a^{(1)} + \left(\bar T, \hat V^{(2)} \cdot e_z\right) a^{(2)} + \left(\bar T, \nabla^2 \hat T\right) b,$$

under Galerkin procedure where $c^{(1)}$, $c^{(2)}$ and d are nonlinear terms. At this point, it is important to note that by the construction of the solenoidal basis and its dual, the pressure term vanishes in the resulting system.

Products of cross components of basis and dual basis vanish by construction and system reduces to:

$$\begin{pmatrix} \left(\bar V^{(1)}, \hat V^{(1)}\right) & 0 \\ 0 & \left(\bar V^{(2)}, \hat V^{(2)}\right) \end{pmatrix} \begin{pmatrix} \dot a^{(1)} \\ \dot a^{(2)} \end{pmatrix} + \begin{pmatrix} c^{(1)} \\ c^{(2)} \end{pmatrix} =$$

$$PrRa_h \begin{pmatrix} 0 \\ \left(\bar V^{(2)}, \hat T e_z\right) \end{pmatrix} \begin{pmatrix} b \\ b \end{pmatrix} + Pr \begin{pmatrix} \left(\bar V^{(1)}, (\nabla^2 - 2\Omega e_z)\hat V^{(1)}\right) & \left(\bar V^{(1)}, (-2\Omega e_z)\hat V^{(2)}\right) \\ \left(\bar V^{(2)}, (-2\Omega e_z)\hat V^{(1)}\right) & \left(\bar V^{(2)}, (\nabla^2 - 2\Omega e_z)\hat V^{(2)}\right) \end{pmatrix} \begin{pmatrix} a^{(1)} \\ a^{(2)} \end{pmatrix},$$

$$\left(\bar T, \hat T\right) \dot b + d = \left(\bar T, \hat V^{(2)} \cdot e_z\right) a^{(2)} + \left(\bar T, \nabla^2 \hat T\right) b.$$

The resulting system governing the time evolution of the time dependent expansion coefficients $a^{(1,2)}, b$ with the mass (M_r) and stiffness (S_r) matrices:

$$\underbrace{\begin{pmatrix} \left(\bar V^{(1)}, \hat V^{(1)}\right) & 0 & 0 \\ 0 & \left(\bar V^{(2)}, \hat V^{(2)}\right) & 0 \\ 0 & 0 & \left(\bar T, \hat T\right) \end{pmatrix}}_{M_r} \begin{pmatrix} \dot a^{(1)} \\ \dot a^{(2)} \\ \dot b \end{pmatrix} + \begin{pmatrix} c^{(1)} \\ c^{(2)} \\ d \end{pmatrix} =$$

$$\underbrace{Pr \begin{pmatrix} \left(\bar V^{(1)}, (\nabla^2 - 2\Omega e_z)\hat V^{(1)}\right) & \left(\bar V^{(1)}, -2\Omega e_z \hat V^{(2)}\right) & 0 \\ \left(\bar V^{(2)}, -2\Omega e_z \hat V^{(1)}\right) & \left(\bar V^{(2)}, (\nabla^2 - 2\Omega e_z)\hat V^{(2)}\right) & Ra_h \left(\bar V^{(2)}, \hat T e_z\right) \\ 0 & \left(\bar T, \hat V^{(2)} \cdot e_z\right)/2Pr & \left(\bar T, \nabla^2 \hat T\right)/Pr \end{pmatrix}}_{S_r} \begin{pmatrix} a^{(1)} \\ a^{(2)} \\ b \end{pmatrix}. \qquad (6.3)$$

are used to investigate the effect of rotation numerically.

6.1 LINEAR STABILITY ANALYSIS

Early theoretical investigation on the linear stability is conducted by Chandrasekhar [2]. Another detailed linear stability analysis of rotating Rayleigh-Bénard equations is performed by Clever and Busse [38]. They reported critical wavenumbers and corresponding critical Rayleigh number values for a range of Ω.

At the onset of convective motions, the velocity and temperature perturbations over the conductive state are negligible, so that the nonlinear terms in equation (6.3) can be neglected to get the linearized system

$$
\begin{pmatrix} \left(\bar{V}^{(1)}, \hat{V}^{(1)}\right) & \left(\bar{V}^{(1)}, \hat{V}^{(2)}\right) \\ \left(\bar{V}^{(2)}, \hat{V}^{(1)}\right) & \left(\bar{V}^{(2)}, \hat{V}^{(2)}\right) \end{pmatrix} \begin{pmatrix} \dot{a}^{(1)} \\ \dot{a}^{(2)} \end{pmatrix} = PrRa_h \begin{pmatrix} \left(\bar{V}^{(1)}, \hat{T} e_z\right) \\ \left(\bar{V}^{(2)}, \hat{T} e_z\right) \end{pmatrix} \begin{pmatrix} b \\ b \end{pmatrix}
$$
$$
+Pr \begin{pmatrix} \left(\bar{V}^{(1)}, (\nabla^2 - 2\Omega e_z)\hat{V}^{(1)}\right) & \left(\bar{V}^{(1)}, (\nabla^2 - 2\Omega e_z)\hat{V}^{(2)}\right) \\ \left(\bar{V}^{(2)}, (\nabla^2 - 2\Omega e_z)\hat{V}^{(1)}\right) & \left(\bar{V}^{(2)}, (\nabla^2 - 2\Omega e_z)\hat{V}^{(2)}\right) \end{pmatrix} \begin{pmatrix} a^{(1)} \\ a^{(2)} \end{pmatrix},
$$

$$
\left(\bar{T}, \hat{T}\right) \dot{b} = \left(\bar{T}, \hat{V}^{(1)} \cdot e_z\right) a^{(1)} + \left(\bar{T}, \hat{V}^{(2)} \cdot e_z\right) a^{(2)} + \left(\bar{T}, \nabla^2 \hat{T}\right) b.
$$

After introducing the zero blocks corresponding to the products of cross components of basis and dual basis as before, the linear system of ODEs reduces to

$$
\begin{pmatrix} \left(\bar{V}^{(1)}, \hat{V}^{(1)}\right) & 0 \\ 0 & \left(\bar{V}^{(2)}, \hat{V}^{(2)}\right) \end{pmatrix} \begin{pmatrix} \dot{a}^{(1)} \\ \dot{a}^{(2)} \end{pmatrix} = PrRa_h \begin{pmatrix} 0 \\ \left(\bar{V}^{(2)}, \hat{T} e_z\right) \end{pmatrix} \begin{pmatrix} b \\ b \end{pmatrix}
$$
$$
+Pr \begin{pmatrix} \left(\bar{V}^{(1)}, (\nabla^2 - 2\Omega e_z)\hat{V}^{(1)}\right) & \left(\bar{V}^{(1)}, -2\Omega e_z \hat{V}^{(2)}\right) \\ \left(\bar{V}^{(2)}, -2\Omega e_z \hat{V}^{(1)}\right) & \left(\bar{V}^{(2)}, (\nabla^2 - 2\Omega e_z)\hat{V}^{(2)}\right) \end{pmatrix} \begin{pmatrix} a^{(1)} \\ a^{(2)} \end{pmatrix},
$$

$$
\left(\bar{T}, \hat{T}\right) \dot{b} = \left(\bar{T}, \hat{V}^{(2)} \cdot e_z\right) a^{(2)} + \left(\bar{T}, \nabla^2 \hat{T}\right) b.
$$

The two system can be combined to form the mass (M_r) and the stiffness (S_r) coefficient matrices for the rotation case

$$\underbrace{\begin{pmatrix} \left(\bar{V}^{(1)}, \hat{V}^{(1)}\right) & 0 & 0 \\ 0 & \left(\bar{V}^{(2)}, \hat{V}^{(2)}\right) & 0 \\ 0 & 0 & \left(\bar{T}, \hat{T}\right) \end{pmatrix}}_{M_r} \begin{pmatrix} \dot{a}^{(1)} \\ \dot{a}^{(2)} \\ \dot{b} \end{pmatrix} =$$

$$\underbrace{Pr \begin{pmatrix} \left(\bar{V}^{(1)}, (\nabla^2 - 2\Omega e_z)\hat{V}^{(1)}\right) & \left(\bar{V}^{(1)}, -2\Omega e_z \hat{V}^{(2)}\right) & 0 \\ \left(\bar{V}^{(2)}, -2\Omega e_z \hat{V}^{(1)}\right) & \left(\bar{V}^{(2)}, (\nabla^2 - 2\Omega e_z)\hat{V}^{(2)}\right) & Ra_h \left(\bar{V}^{(2)}, \hat{T} e_z\right) \\ 0 & \left(\bar{T}, \hat{V}^{(2)} \cdot e_z\right)/2Pr & \left(\bar{T}, \nabla^2 \hat{T}\right)/Pr \end{pmatrix}}_{S_r} \begin{pmatrix} a^{(1)} \\ a^{(2)} \\ b \end{pmatrix}. \quad (6.4)$$

After introducing a time dependence of the expansion coefficients in the form $a^{(1)}(t) = exp(\lambda t)a_0^{(1)}$, $a^{(2)}(t) = exp(\lambda t)a_0^{(2)}$ and $b(t) = exp(\lambda t)b_0$ into the above system, one gets the generalized eigenvalue problem

$$\lambda M_r \begin{pmatrix} a_0^{(1)} \\ a_0^{(2)} \\ b_0 \end{pmatrix} = S_r \begin{pmatrix} a_0^{(1)} \\ a_0^{(2)} \\ b_0 \end{pmatrix}.$$

The stability of this system is determined by the eigenvalues of the Jacobian matrix as explained in § 4.2. Linear stability curves for various rotation rates (see Figure 6.1) are calculated and they are in good agreement with literature [2, 38]. Figures 6.2 and 6.3 show that critical Rayleigh number and the critical wavenumber increase with increasing rotation rate. The rate of increase changes for $\Omega > 20$. More recent research is conducted by Scheel [37]. work. She computed the variation of critical Rayleigh number and critical wavenumber versus rotation. Our findings (figure 6.2 and 6.3) match with the Clever's [38] and Schell's [37] results.

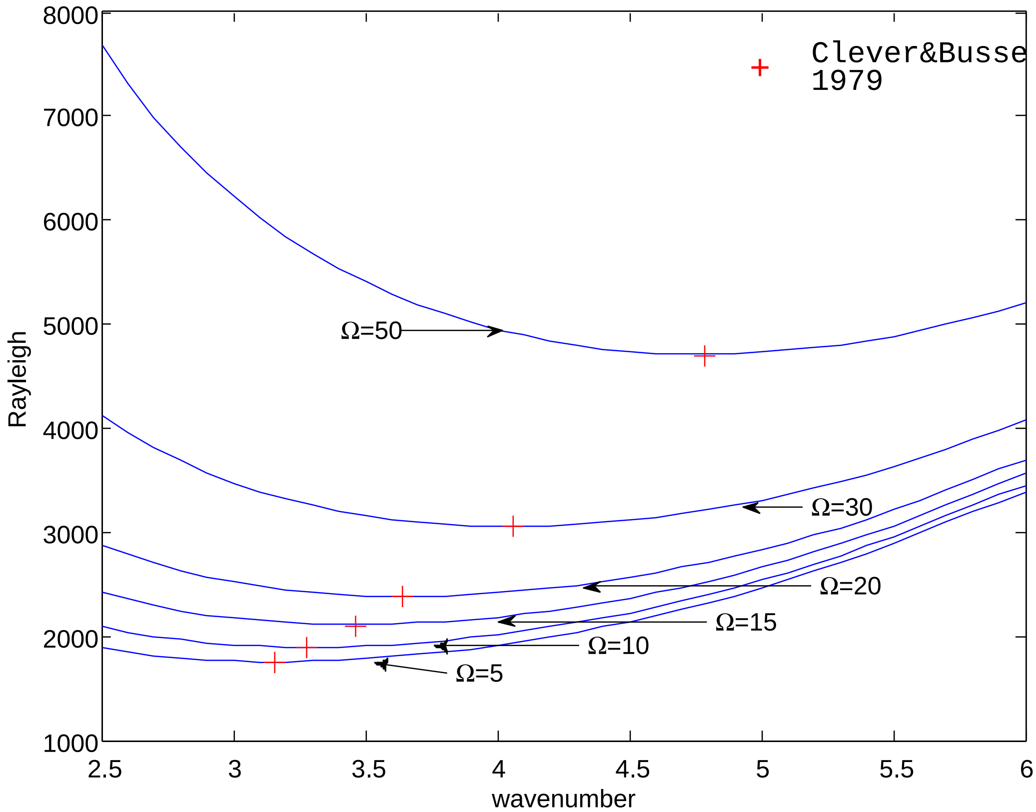

Figure 6.1: Linear stability curve effected by different rotation force

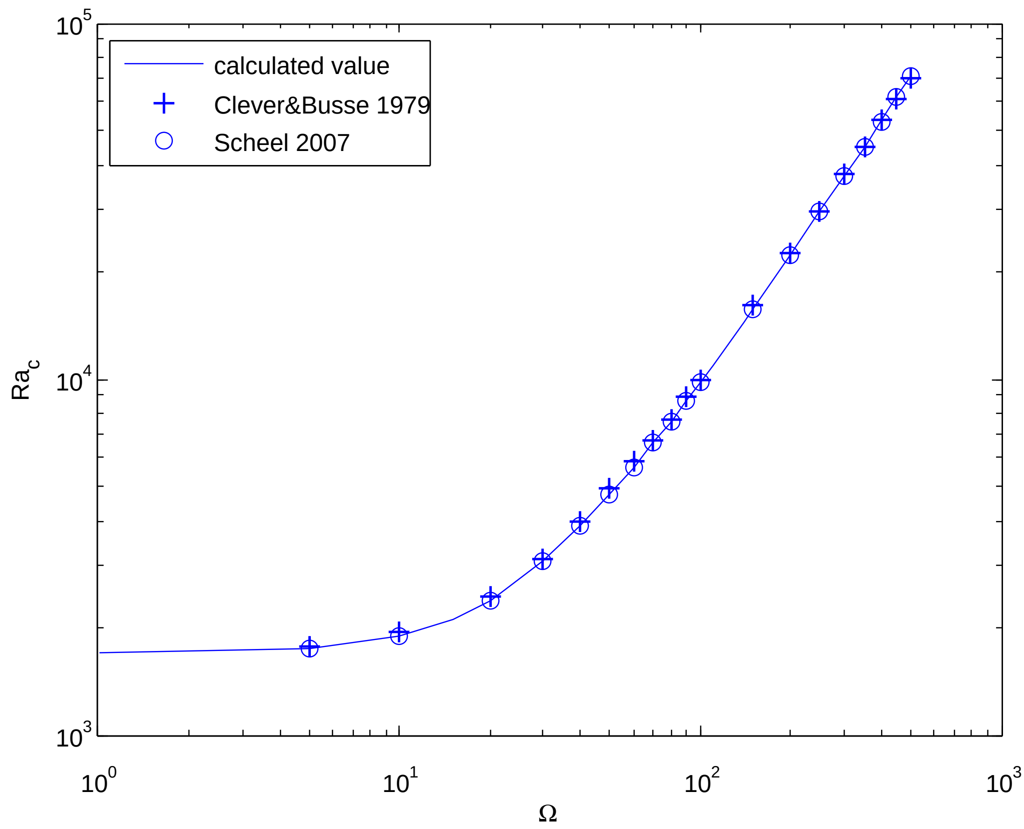

Figure 6.2: The critical Rayleigh number (Ra_c) variation with rotation

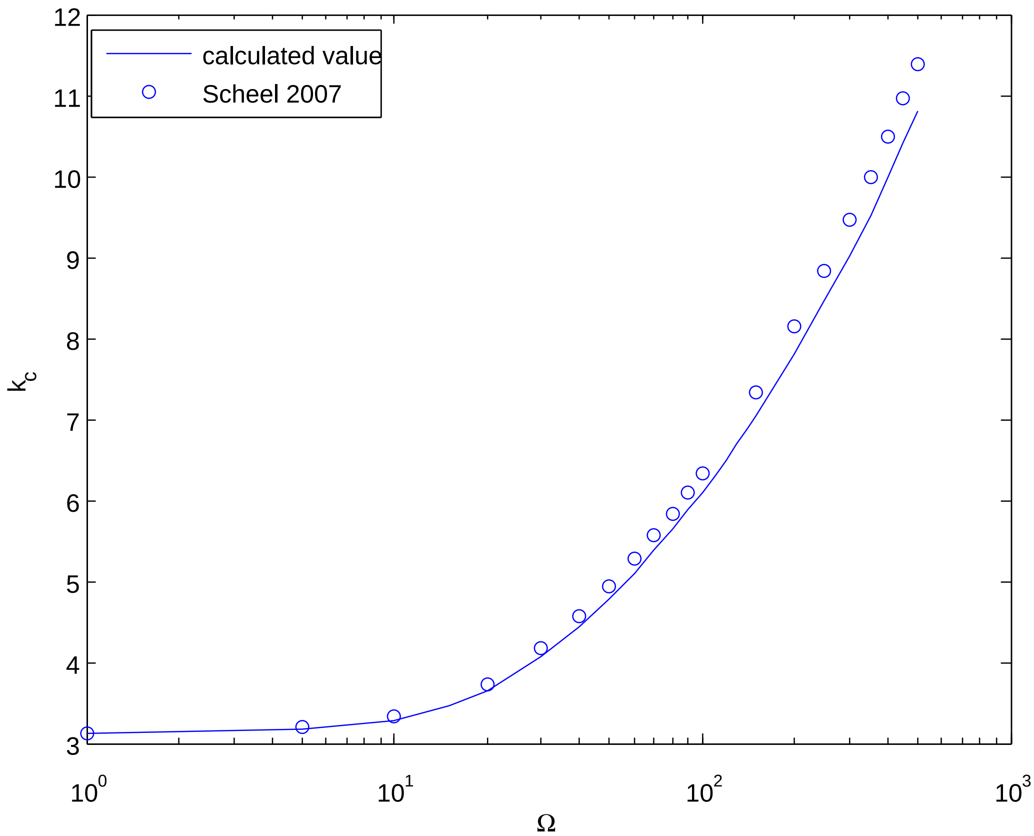

Figure 6.3: The critical wavenumber (k_c) variation with rotation

Table 6.1: Critical Rayleigh number and corresponding critical wavenumber influenced by rotation

Ω	Ra_c	k_c
1	1.709720e+03	3.12
5	1.756340e+03	3.16
10	1.895650e+03	3.28
15	2.110500e+03	3.45
20	2.384370e+03	3.65
30	3.057960e+03	4.06
40	3.845780e+03	4.44
50	4.712040e+03	4.78
60	5.638050e+03	5.09
70	6.613270e+03	5.38
80	7.631280e+03	5.63
90	8.687730e+03	5.87
100	9.779510e+03	6.10
110	1.090426e+04	6.31
120	1.206005e+04	6.50
130	1.324526e+04	6.69
140	1.445853e+04	6.87
150	1.569865e+04	7.04
200	2.226776e+04	7.80
250	2.937952e+04	8.45
300	3.695596e+04	9.02
350	4.493512e+04	9.52
400	5.326733e+04	9.98
450	6.191361e+04	10.40
500	7.084390e+04	10.79

Table 6.2: Comparison of critical values with Chandrasekhar's [2] calculation. Second approximation of Chandrasekhar's value are considered.

Ω ($Ta = 4\Omega^2$)	Ra_c	Ra_c (Ch)	k_c	k_c (Ch)
5	1756.34	1756.6	3.16	3.15
50	4712.04	4713.1	4.78	4.80
500	70843.90	71132	10.79	10.80

6.2 TIME DISCRETIZATION

For time discretization of rotating natural convection semi-implicit integration is used. The nonlinear and driving (buoyancy and Coriolis) terms are integrated explicitly using third order Adams-Bashforth, while diffusive terms are integrated implicitly using third order Adams-Moulton. Under the time discretization, the governing equations (2.21) and (2.22) become:

$$\begin{aligned}\frac{\mathbf{u}^{n+1}-\mathbf{u}^{n}}{\Delta t} =& \frac{23}{12}\left(-\left(\mathbf{u}\cdot\nabla\right)\mathbf{u}+PrRa\theta e_z-2Pr\Omega e_z\times\mathbf{u}\right)^{n}- \\ &\frac{16}{12}\left(-\left(\mathbf{u}\cdot\nabla\right)\mathbf{u}+PrRa\theta e_z-2Pr\Omega e_z\times\mathbf{u}\right)^{n-1}+ \\ &\frac{5}{12}\left(-\left(\mathbf{u}\cdot\nabla\right)\mathbf{u}+PrRa\theta e_z-2Pr\Omega e_z\times\mathbf{u}\right)^{n-2}+ \\ &Pr\nabla^2\left(\frac{5}{12}\mathbf{u}^{n+1}+\frac{8}{12}\mathbf{u}^{n}-\frac{1}{12}\mathbf{u}^{n-1}\right)\end{aligned} \tag{6.5}$$

$$\begin{aligned}\frac{\theta^{n+1}-\theta^{n}}{\Delta t} =& \frac{23}{12}\left(-\left(\mathbf{u}\cdot\nabla\right)\theta+\frac{w}{2}\right)^{n}-\frac{16}{12}\left(-\left(\mathbf{u}\cdot\nabla\right)\theta+\frac{w}{2}\right)^{n-1}+ \\ &\frac{5}{12}\left(-\left(\mathbf{u}\cdot\nabla\right)\theta+\frac{w}{2}\right)^{n-2}+\nabla^2\left(\frac{5}{12}\theta^{n+1}+\frac{8}{12}\theta^{n}-\frac{1}{12}\theta^{n-1}\right)\end{aligned} \tag{6.6}$$

Time discretized equations are projected onto the dual space after the substitution of the expansions for $\mathbf{u}$ (6.1) and for Θ (6.2) to get the nonlinear system the discrete time evolution of the expansion coefficients;

$$\begin{aligned}M_r(1,1)\frac{a^{(1)^{n+1}}-a^{(1)^{n}}}{\Delta t} =& \frac{1}{12}S_r(1,1)\left(5a^{(1)^{n+1}}+8a^{(1)^{n}}-a^{(1)^{n-1}}\right) \\ &+\frac{1}{12}S_r(1,2)\left(5a^{(2)^{n+1}}+8a^{(2)^{n}}-a^{(2)^{n-1}}\right) \\ &-\frac{1}{12}\left(23c^{(1)^{n}}-16c^{(1)^{n-1}}+5c^{(1)^{n-2}}\right) \\ M_r(2,2)\frac{a^{(2)^{n+1}}-a^{(2)^{n}}}{\Delta t} =& \frac{1}{12}S_r(2,1)\left(5a^{(1)^{n+1}}+8a^{(1)^{n}}-a^{(1)^{n-1}}\right) \\ &+\frac{1}{12}S_r(2,2)\left(5a^{(2)^{n+1}}+8a^{(2)^{n}}-a^{(2)^{n-1}}\right) \\ &-\frac{1}{12}\left(23c^{(2)^{n}}-16c^{(2)^{n-1}}+5c^{(2)^{n-2}}\right) \\ &+\frac{1}{12}S_r(2,3)\left(23b^{n}-16b^{n-1}+5b^{n-2}\right) \\ M_r(3,3)\frac{b^{n+1}-b^{n}}{\Delta t} =& \frac{1}{12}S_r(3,3)\left(5b^{n+1}+8b^{n}-b^{n-1}\right) \\ &-\frac{1}{12}\left(23d^{n}-16d^{n-1}+5d^{n-2}\right) \\ &+\frac{1}{12}S_r(3,2)\left(23a^{(2)^{n}}-16a^{(2)^{n-1}}+5a^{(2)^{n-2}}\right)\end{aligned}$$

where $M_r(i, j)$ and $S_r(i, j)$ refer to the $(i, j)^{\text{th}}$ block matrices of the "M_r" and "S_r", respectively. Three known steps are required to calculate one unknown step because of third order discretization. Linear stability eigensolution or known nonlinear solution from the previous run can be used as initial conditions.

6.3 NONLINEAR PROPERTIES OF ROTATION

It is observed in Figure 6.4(c) that limited rotation in moderate Prandtl fluids stabilizes the convection and suppresses the oscillation in high Rayleigh number flow. This phenomena is also observed by Veronis [30]. Increased heat flux is caused by the stabilizing effect of limited rotation for range of $\Omega = 0 - 30$. Coriolis force can balance horizontal temperature gradients. Hence less potential energy is released by horizontal temperature gradients. On the other hand, increasing rotation destabilizes the system and brings new oscillatory motions for $Ra - Ra_c = 20000$ [38]. Increased heat flux with limited rotation is also observed for low Rayleigh number flows in Figure 6.4(a,b), but this increment is very low because convection is still two dimensional at these parameter values. Heat flux decreases at $\Omega = 10$ for $Ra - Ra_c = 2000$, $\Omega = 30$ for $Ra - Ra_c = 10000$ and $\Omega = 30$ for $Ra - Ra_c = 20000$ because horizontal velocities destabilize the system with increasing rotation. Veronis [30] indicated that rotational constraint balances the non-linear processes for up to $Ta \leq 10^{3.6}$ ($\Omega \approx 31$) for convection between free boundaries. More recent work conducted by Clever and Busse [38] reported that rolls are unstable for $Pr > 1$ beyond $\Omega \approx 27$. In general, increasing rotation rate bring unstable behaviour for all Prandtl fluids.

Coriolis term depends linearly on the horizontal velocity. Hence increasing rotation rate magnify the toroidal energy as shown in Figures 6.5, 6.6 and 6.7. For all Rayleigh number values increasing rotation absorbs the poloidal energy and stimulates the toroidal energy. Increase in toroidal energy is very rapid for $Ra - Ra_c = 2000$ and $Ra - Ra_c = 10000$ because both cases correspond to steady two dimensional convection in non-rotating system. Limited Coriolis force, for example $\Omega = 10$, does not affect the roll structure but introduces three dimensional motion as it is seen in Figures 6.8 and 6.9. This motion appears in oblique angle to the roll direction as also observed by Veronis [29]. On the other hand, $Ra - Ra_c = 20000$ case exhibits a different behaviour. Since it corresponds to periodic motion in non-rotating system, it contains small scale motions with vertical vorticity. The motion tends to two dimensional convection with increasing rotation and toroidal energy sharply decreases and poloidal energy conversely increases for $\Omega \approx 15$. It is caused due to the stabilizing effect of limited rotation as explained above. This effect also increases the heat transport because of increasing poloidal component. As vertical shear increases, $\Omega \geq 15$ for low Rayleigh and $\Omega \geq 30$ for high Rayleigh numbers, toroidal motion dominates and brings unstable character.

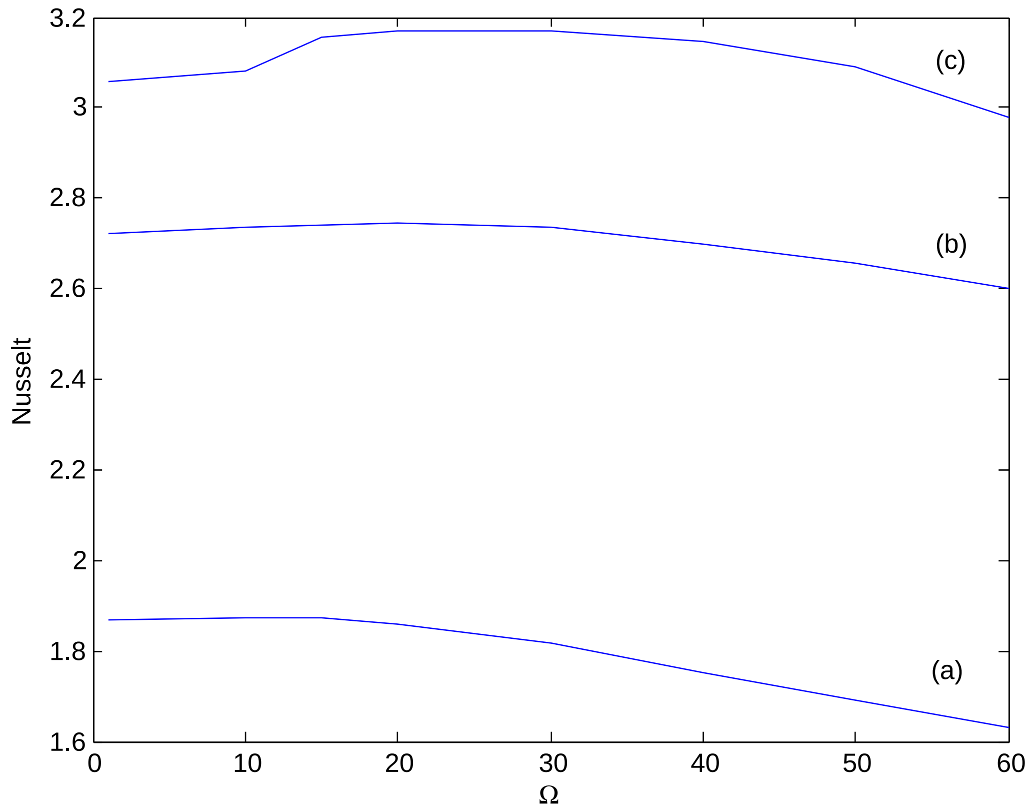

Figure 6.4: Nusselt number variation with rotation, $Pr = 0.71$, $(a) Ra - Ra_c = 2000$, $(b) Ra - Ra_c = 10000$, $(c) Ra - Ra_c = 20000$; $\alpha = k_c(\Omega)$; $(a), (b)$ with 16x16x16 resolution, (c) with 16x16x20 resolution

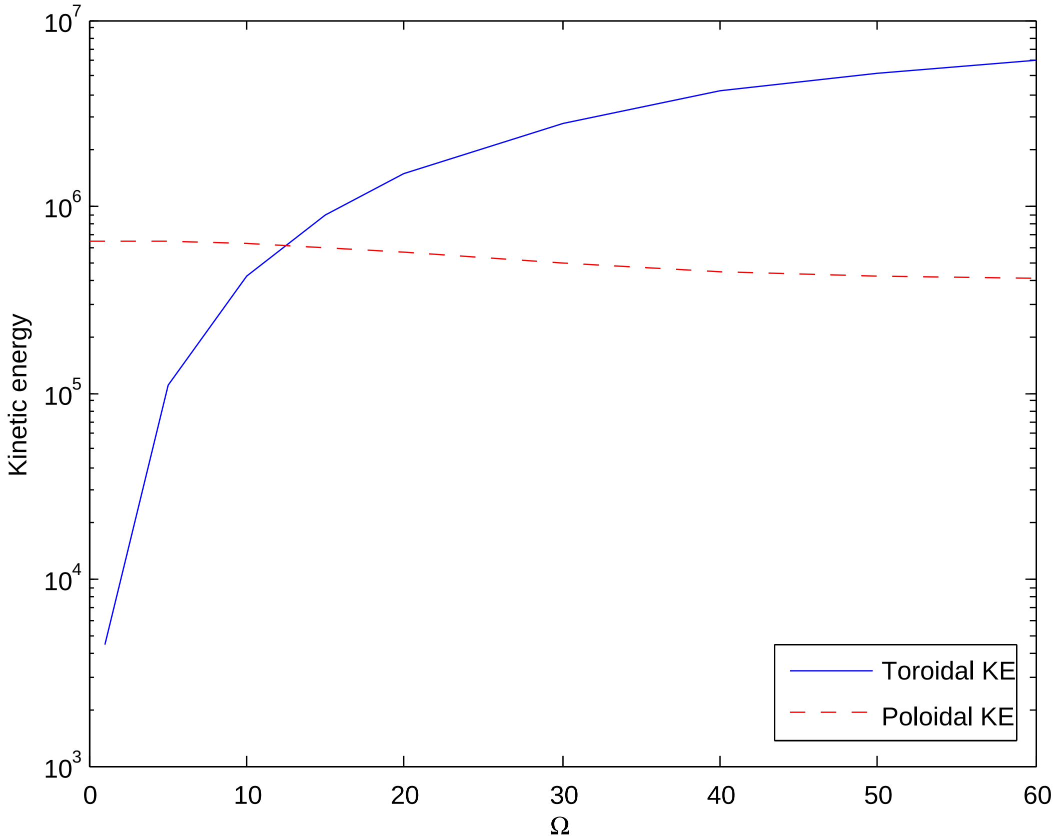

Figure 6.5: Toroidal and poloidal kinetic energy variation with rotation, $Pr = 0.71$, $Ra - Ra_c = 2000$, $\alpha = k_c(\Omega)$, 16x16x16 resolution

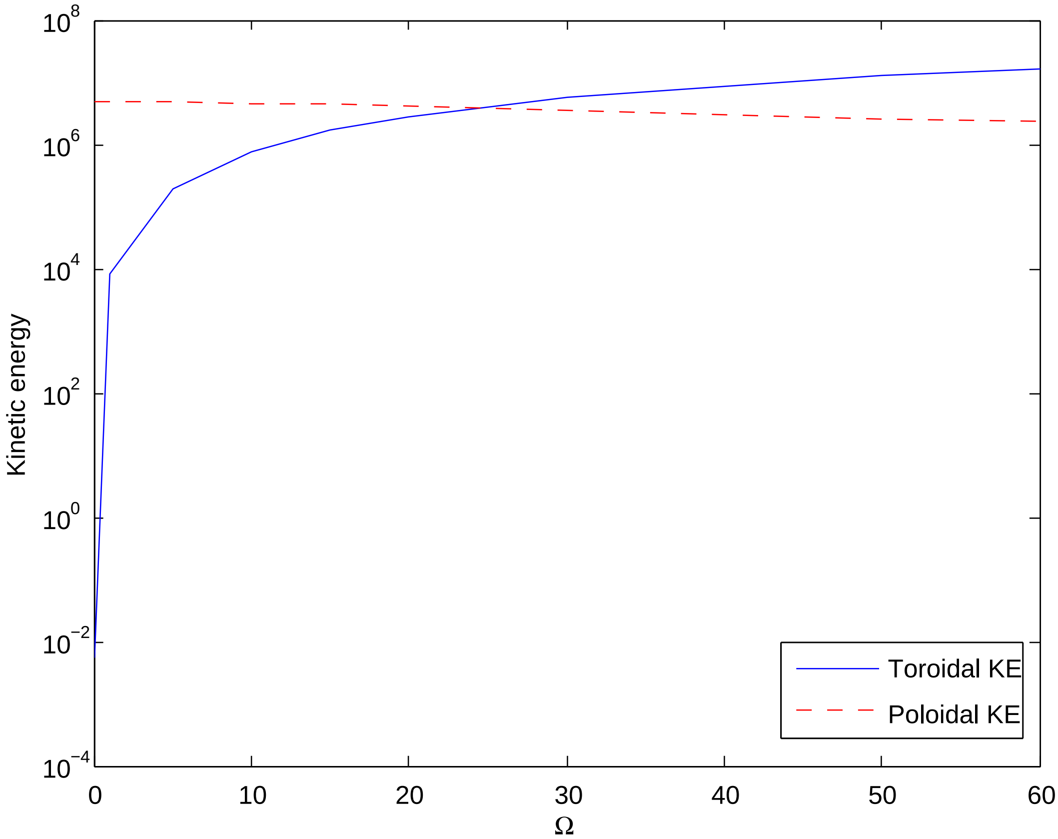

Figure 6.6: Toroidal and poloidal kinetic energy variation with rotation, $Pr = 0.71$, $Ra - Ra_c = 10000$ $\alpha = k_c(\Omega)$, 16x16x16 resolution

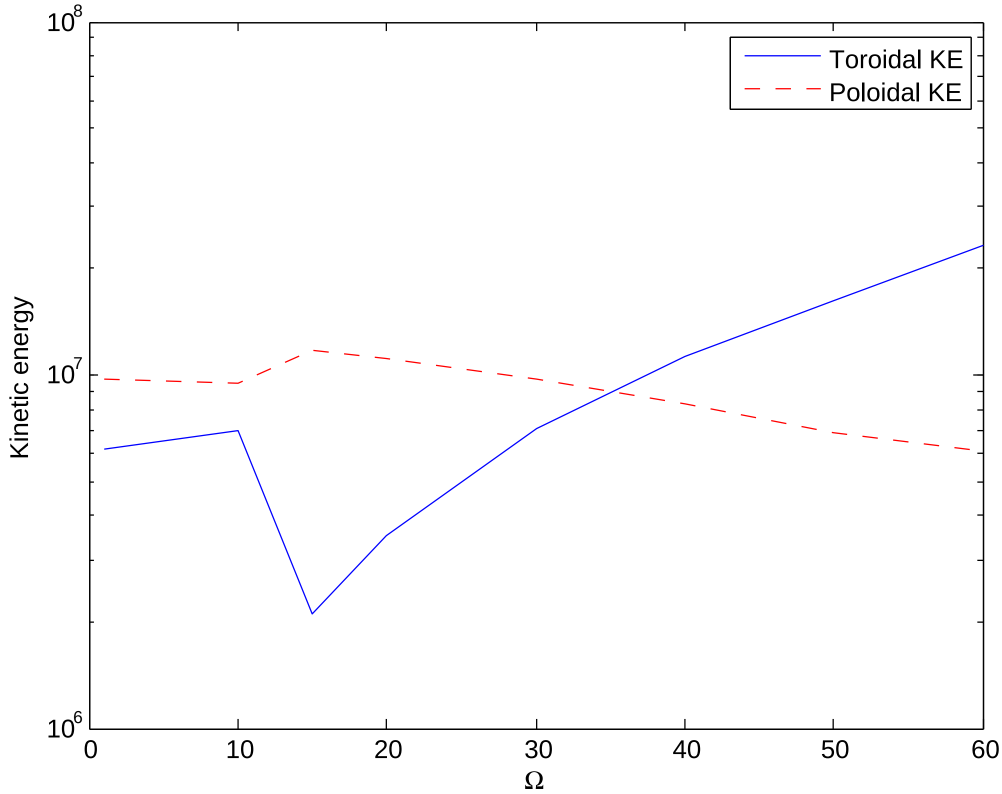

Figure 6.7: Toroidal and poloidal kinetic energy variation with rotation, $Pr = 0.71$, $Ra - Ra_c = 20000$, $\alpha = k_c(\Omega)$, 16x16x20 resolution

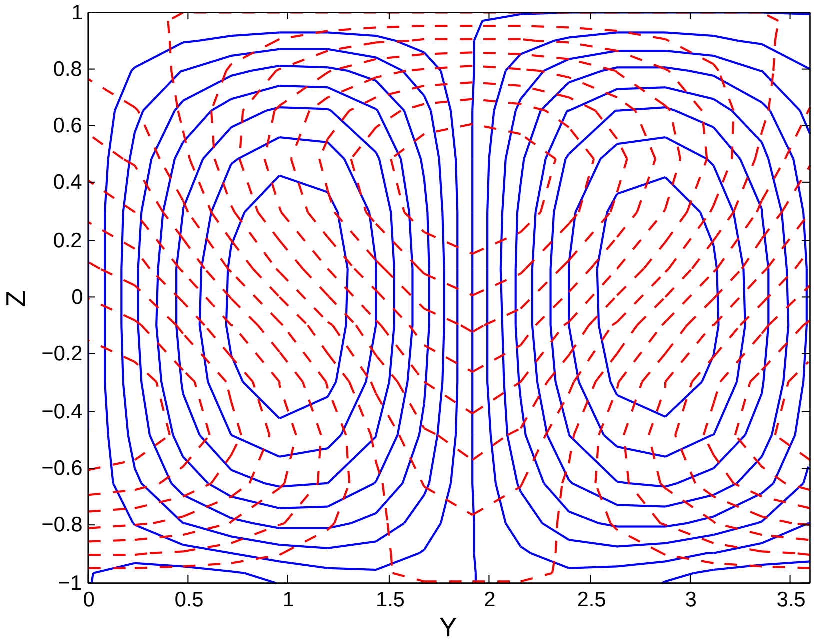

Figure 6.8: v-w streamline (solid line) and temperature contour (dash line) on Y-Z plane at $x = L_x/4$, $Pr = 0.71$, $Ra - Ra_c = 2000$, $\Omega = 10$

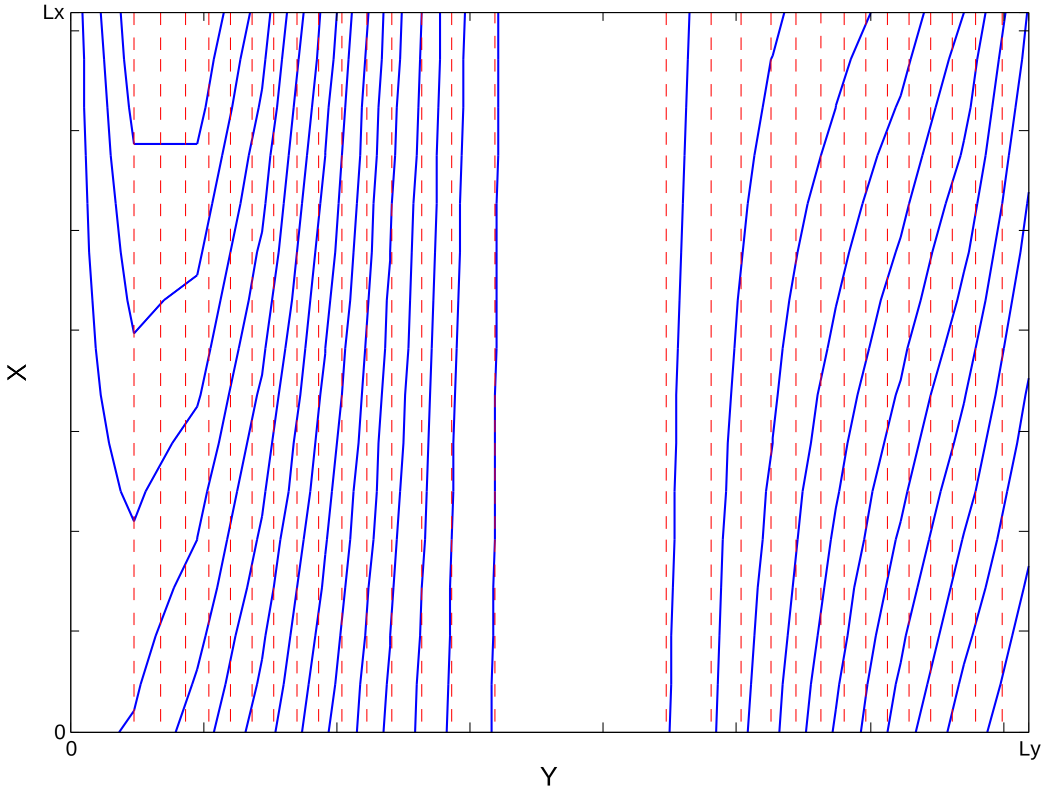

Figure 6.9: u-v streamline (solid line) and temperature contour (dash line) on X-Y plane at $z = 0.4861$, $Pr = 0.71$, $Ra - Ra_c = 2000$, $\Omega = 10$

CHAPTER 7

CONCLUSION

In this thesis, the use of two different solenoidal bases, namely, KL bases and analytic solenoidal bases, is investigated. Both bases are tested on well-known and well-studied Rayleigh-Bénard convection. Rigid vertical and periodic horizontal boundaries are considered for realistic treatment. Periodic horizontal boundaries may account for large horizontal extent convective layers. There are large amount of work on Rayleigh-Bénard convection, however, the construction and implementation of the solenoidal bases in this thesis is novel.

Karhunen-Lóeve decomposition is an efficient tool in extracting hidden or complicated dynamics within a flow database generated numericaly or experimentally. In this work, Boussinesq equations for some reference parameter values are numerically integrated using a spectral element algorithm from literature in order to generate the database. The algorithm, like most incompressible flow solvers in literature, can only produce a limited resolution to the divergence free criteria. This poor resolution is carried to the KL bases in the construction process that involves solving an eigenproblem and KL bases are the eigenvectors of the two-point velocity correlation tensor. This limited satisfaction of the solenoidal condition gets even worse down in the hiearchy of the KL modes due to the loss of accuracy in computing the eigensolutions. Thus, KL modes make poor solenoidal bases. The advantage of the KL bases is in their parametrization of the underlying dynamics in energy optimal sense. For reference parameter values, fewer KL modes are necessary to represent the flow variables in a truncated representation compared to any other bases. However, this optimality is lost at off-reference values of the flow parameters, thus KL bases are parameter dependent. These considerations are precluded the use of KL bases in a parametric study of thermal convection. Instead, they are used to study the underlying dynamics in the generated database for various parameter values. The use of flow symmetries and the underlying Legendre polynomial representation in this part of the study provided the inspiration to be carried to the alternative form of solenoidal bases, namely, analytic solenodal bases, next.

Analytic solenoidal bases (or just solenoidal bases) are used to study the dynamics of thermal convection for a range of parameter values covering different flow regimes. The overall approach may be termed as solenoidal spectral method. The most important advantage of the solenoidal bases is their exact satisfaction of the divergence-free criteria. Their construction does not require a database to be generated beforehand, which ironically necessitates the implementation of another numerical solver, and they are parameter free. Their representation of the flow variables in terms of time dependent expansion coefficients provide the convenient tool to reduce the governing PDEs to a dynamical system that is amenable to implementing the tools of dynamical system theory and bifurcation theory. The ease and high accuracy obtained in the linear stability analysis of the system is encouraging in this direction. The advantage of eliminating the pressure term in the process of projection onto the dual space is in the heart of the implementational convenience. Solenoidal bases lack any rational criteria of ordering the bases elements based on their importance in the dynamics of the flow as opposed to KL bases that come attached with their share of total kinetic energy of the flow. Thus, the expansions in terms solenoidal bases result in larger system. However, the techniques of Fourier and Legendre spectral methods, such as, FFT procedure of computing derivatives and the nonlinear terms, the accurate evaluation of inner product integrals using Legendre Gaussian quadrature, help overcome this drawback. Furthermore, the form of the resulting system facilitates the use of creative implementation techniques such as, iterative solvers and parallelization.

7.1 FUTURE WORKS

Semi-implicit and explicit time solvers are usually employed in order to avoid the need to invert coefficient matrices in advancing to the next time step. Unless some kind of orthogonality can be introduced into the solenoidal bases, the presence of the mass matrix in the resulting system already requires inversion. The work by Moser, Moin and Leonard [60] advices against imposing any further restrictions onto the bases that may degrade the method. Thus, unconditionally stable fully implicit time solvers combined with powerfull Newton method may be explored in the future implementation. This removes severe restrictions imposed by explicit or semi-implicit methods on the time step and improves long term integration.

Iterative solvers for the resulting system may be implemented. This also motivates construction of suitable preconditioners for the system especially when the resulting system is stiff for certain parameter ranges, such as, low Prandtl number cases.

The tools of computational Bifurcation analysis should be implemented in the parametric study in order to better understand the underlying dynamics. Continuation methods and Floquet analysis in studying periodic regimes are important components of these tools. This will be a valuable complement to the implementation of solenoidal spectral method.

Appendix A

KARHUNEN LOÉVE DECOMPOSITION

A.1 THE EIGENVALUE PROBLEM

The aim of the Karhunen Loéve (KL) technique is to determine a vector $\mathbf{\Psi}_i(x_1, x_2, x_3)$ which will maximize the quantity $\sum_{n=1}^{N} |(v_i^n, \mathbf{\Psi}_i)|^2$ subject to the condition $(\mathbf{\Psi}_i, \mathbf{\Psi}_i) = 1$. Here, the inner product is defined as $(a_i, b_i) = \int_D a_i(\mathbf{x})\bar{b}_i(\mathbf{x})d\mathbf{x}$ where repeated index indicates summation over the range of the index and overbar denotes complex conjugation. Then the energy is defined as $|\mathbf{v}|^2 = \mathbf{v}\bar{\mathbf{v}}$, which can be written in terms of eigenfunction expansion as

$$E = \sum_{n=1}^{N} |(v_i^n, \mathbf{\Psi}_i)|^2 = \sum_{n=1}^{N} (\mathbf{\Psi}_i, v_i^n)(v_j^n, \mathbf{\Psi}_j). \tag{A.1}$$

It can be rewritten in the form

$$E = \sum_{n=1}^{N} \int_D \bar{\mathbf{\Psi}}_i(\mathbf{x}) v_i^n(\mathbf{x}) d\mathbf{x} \int_D \bar{v}_j^n(\acute{\mathbf{x}}) \mathbf{\Psi}_j(\acute{\mathbf{x}}) d\acute{\mathbf{x}}, \tag{A.2}$$

or

$$E = \int_D \bar{\mathbf{\Psi}}_i(\mathbf{x}) \int_D \sum_{n=1}^{N} v_i^n(\mathbf{x}) \bar{v}_j^n(\acute{\mathbf{x}}) \mathbf{\Psi}_j(\acute{\mathbf{x}}) d\acute{\mathbf{x}} d\acute{\mathbf{x}}. \tag{A.3}$$

By defining the kernel

$$K_{ij}(\mathbf{x}, \acute{\mathbf{x}}) = \sum_{n=1}^{N} v_i^n(\mathbf{x}) \bar{v}_j^n(\acute{\mathbf{x}}), \tag{A.4}$$

the energy can also be defined as

$$E = (\mathbf{\Psi}_i, K_{ij} \mathbf{\Psi}_j). \tag{A.5}$$

The product of the kernel with a vector is defined by

$$K_{ij}\mathbf{\Psi}_j = \int_D K_{ij}(\mathbf{x},\acute{\mathbf{x}})\mathbf{\Psi}_j(\acute{\mathbf{x}})d\acute{\mathbf{x}}. \tag{A.6}$$

Introducing a Lagrange multiplier λ and considering the orthogonality constraint $(\mathbf{\Psi}_i,\mathbf{\Psi}_i) = 1$, the modified energy becomes

$$E^\star = E - \lambda(\mathbf{\Psi}_i,\mathbf{\Psi}_i). \tag{A.7}$$

Perturbation of the eigenfunction yields the equation

$$\begin{aligned} E^\star(\mathbf{\Psi} + a\acute{\mathbf{\Psi}}) = &\int_D \overline{\mathbf{\Psi}_i + a\acute{\mathbf{\Psi}}_i}\int_D K_{ij}(\mathbf{\Psi}_j + a\acute{\mathbf{\Psi}}_j)d\acute{\mathbf{x}}d\mathbf{x} \\ &- \lambda\int_D \overline{(\mathbf{\Psi}_i + a\acute{\mathbf{\Psi}}_i)}(\mathbf{\Psi}_i + a\acute{\mathbf{\Psi}}_i)d\mathbf{x}, \end{aligned}$$

or

$$\begin{aligned} E^\star(\mathbf{\Psi} + a\acute{\mathbf{\Psi}}) = &\int_D \overline{\mathbf{\Psi}_i + a\acute{\mathbf{\Psi}}_i}\int_D K_{ij}\mathbf{\Psi}_j d\acute{\mathbf{x}}d\mathbf{x} + \int_D \overline{\mathbf{\Psi}_i + a\acute{\mathbf{\Psi}}_i}\int_D K_{ij}a\acute{\mathbf{\Psi}}_j d\acute{\mathbf{x}}d\mathbf{x} \\ &- \lambda\Big(\int_D \overline{\mathbf{\Psi}_i + a\acute{\mathbf{\Psi}}_i}\mathbf{\Psi}_i d\mathbf{x} + \int_D \overline{\mathbf{\Psi}_i + a\acute{\mathbf{\Psi}}_i}a\acute{\mathbf{\Psi}}_i d\mathbf{x}\Big). \end{aligned}$$

Minimization of a and $\overline{a}$ give the equations

$$\frac{\partial}{\partial a}E^\star(\mathbf{\Psi}_i + a\acute{\mathbf{\Psi}}_i)|_{a=\bar{a}=0} = 0 = \int_D\int_D \overline{\mathbf{\Psi}_i}K_{ij}\acute{\mathbf{\Psi}}_j d\acute{\mathbf{x}}d\mathbf{x} - \lambda\int_D \overline{\mathbf{\Psi}_i}\acute{\mathbf{\Psi}}_i d\mathbf{x}, \tag{A.8}$$

$$\frac{\partial}{\partial \overline{a}}E^\star(\mathbf{\Psi}_i + a\acute{\mathbf{\Psi}}_i)|_{a=\bar{a}=0} = 0 = \int_D\int_D \overline{\acute{\mathbf{\Psi}}_i}K_{ij}\mathbf{\Psi}_j d\acute{\mathbf{x}}d\mathbf{x} - \lambda\int_D \overline{\acute{\mathbf{\Psi}}_i}\mathbf{\Psi}_i d\mathbf{x}, \tag{A.9}$$

and thus

$$\int_D\Big[\int_D \mathbf{\Psi}_j K_{ij} d\bar{\acute{x}} - \lambda\mathbf{\Psi}_i\Big]\overline{\acute{\mathbf{\Psi}}_i}d\mathbf{x} = 0. \tag{A.10}$$

This equation is valid if

$$\int_D \mathbf{\Psi}_j(\acute{\mathbf{x}})K_{ij}(\mathbf{x},\acute{\mathbf{x}})d\bar{\acute{\mathbf{x}}} - \lambda\mathbf{\Psi}_i(\mathbf{x}) = 0, \tag{A.11}$$

or

$$\int_D K_{ij}(\mathbf{x},\acute{\mathbf{x}})\mathbf{\Psi}_j(\acute{\mathbf{x}}) = \lambda\mathbf{\Psi}_i(\mathbf{x}), \tag{A.12}$$

which is the eigenvalue problem $K_{ij}\mathbf{\Psi}_j = \lambda\mathbf{\Psi}_i$. The solution of the problem gives the most energetic mode $\mathbf{\Psi}_i(\mathbf{x})$ which will correspond the energy in that mode λ.

A.1.1 BOUNDARY CONDITIONS

The velocity and temperature vectors used to shape the eigenfunctions come from the velocity and temperature fields satisfied by the boundary conditions such as

$$v_i^n(x_1, x_2, 1) = v_i^n(x_1, x_2, -1) = 0. \tag{A.13}$$

Substitution of equation (A.13) into the eigenproblem (A.12) gives the boundary conditions for the eigenproblem

$$\mathbf{\Psi}_i(x_1, x_2, 1) = \frac{1}{\lambda}\int_D K_{ij}(x_1, \acute{x}_1, x_2, \acute{x}_2, 1, \acute{x}_3)\mathbf{\Psi}_j(\acute{x}_1, \acute{x}_2, \acute{x}_3)d\acute{\mathbf{x}}. \tag{A.14}$$

The kernel (A.4) at the boundaries can be written as

$$K_{ij}(x_1, \acute{x}_1, x_2, \acute{x}_2, 1, \acute{x}_3) = \sum_{n=1}^{N} v_i(x_1, x_2, 1)\bar{v}_j(\acute{x}_1, \acute{x}_2, \acute{x}_3) = 0, \tag{A.15}$$

and

$$K_{ij}(x_1, \acute{x}_1, x_2, \acute{x}_2, -1, \acute{x}_3) = \sum_{n=1}^{N} v_i(x_1, x_2, -1)\bar{v}_j(\acute{x}_1, \acute{x}_2, \acute{x}_3) = 0. \tag{A.16}$$

Using these formulas in equation (A.14), the following boundary conditions for the eigenfunctions can be obtained

$$\mathbf{\Psi}_i(x_1, x_2, 1) = \int_D 0 \times \mathbf{\Psi}_j(\acute{x}_1, \acute{x}_2, \acute{x}_3)d\acute{\mathbf{x}} = 0, \tag{A.17}$$

and

$$\mathbf{\Psi}_i(x_1, x_2, -1) = \int_D 0 \times \mathbf{\Psi}_j(\acute{x}_1, \acute{x}_2, \acute{x}_3)d\acute{\mathbf{x}} = 0. \tag{A.18}$$

So the set of eigenfunctions obtained from velocity and temperature fields satisfies the same boundary conditions.

A.1.2 INCOMPRESSIBILITY

The incompressibility condition is

$$\frac{\partial}{\partial x_i} v_i(\mathbf{x}) = 0 \qquad \text{for} \qquad i = 1, 2, 3. \tag{A.19}$$

Divergence of the integral equation (A.12) results

$$\frac{\partial}{\partial x_i}\mathbf{\Psi}_i(\mathbf{x}) = \frac{1}{\lambda}\int_D \frac{\partial}{\partial x_i} K_{ij}(\mathbf{x}, \acute{\mathbf{x}})\mathbf{\Psi}_j(\acute{\mathbf{x}})d\acute{\mathbf{x}}. \tag{A.20}$$

The kernel depend on $\mathbf{x}$ and the definition of (A.4) can be used to write the divergence of kernel as

$$\frac{\partial}{\partial x_i} K_{ij}(\mathbf{x}, \acute{\mathbf{x}}) = \sum_{n=1}^{N} \bar{v}_j(\acute{\mathbf{x}})\frac{\partial}{\partial x_i} v_i(\mathbf{x}) = 0. \tag{A.21}$$

Divergence of the eigenfunctions are

$$\frac{\partial}{\partial x_i}\mathbf{\Psi}_i(\mathbf{x}) = \int_D 0 \times \mathbf{\Psi}_j(\acute{\mathbf{x}})d\acute{\mathbf{x}} = 0. \tag{A.22}$$

Hence the eigenfunctions must be incompressible to satisfy the equation above.

A.1.3 ORTHOGONALITY

If $\mathbf{\Psi}_i^m$ and $\mathbf{\Psi}_i^n$ are two different solutions of the eigenvalue problem with respective eigenvalues λ^m and λ^n, satisfying the integral equations

$$\int_D K_{ij}(\mathbf{x}, \acute{\mathbf{x}})\mathbf{\Psi}_j^m(\acute{\mathbf{x}})d\acute{\mathbf{x}} = \lambda^m \mathbf{\Psi}_i^m(\mathbf{x}), \tag{A.23}$$

and

$$\int_D K_{ij}(\mathbf{x}, \acute{\mathbf{x}})\mathbf{\Psi}_j^n(\acute{\mathbf{x}})d\acute{\mathbf{x}} = \lambda^n \mathbf{\Psi}_i^n(\mathbf{x}), \tag{A.24}$$

then multiplying equation (A.23) by $\bar{\mathbf{\Psi}}_i^n(\mathbf{x})$ and integrating over the domain give the relation

$$\begin{aligned}
\lambda^m \int_D \mathbf{\Psi}_i^m(\mathbf{x})\bar{\mathbf{\Psi}}_i^n(\mathbf{x})d\mathbf{x} &= \int_D \int_D K_{ij}(\mathbf{x}, \acute{\mathbf{x}})\mathbf{\Psi}_j^m(\acute{\mathbf{x}})\bar{\mathbf{\Psi}}_i^n(\mathbf{x})d\acute{\mathbf{x}}d\mathbf{x} \\
&= \int_D \mathbf{\Psi}_j^m(\acute{\mathbf{x}}) \int_D K_{ij}(\mathbf{x}, \acute{\mathbf{x}})\bar{\mathbf{\Psi}}_i^n(\mathbf{x})d\mathbf{x}d\acute{\mathbf{x}} \\
&= \int_D \mathbf{\Psi}_j^m(\acute{\mathbf{x}}) \int_D \bar{K}_{ji}(\acute{\mathbf{x}}, \mathbf{x})\bar{\mathbf{\Psi}}_i^n(\mathbf{x})d\mathbf{x}d\acute{\mathbf{x}} \\
&= \lambda^n \int_D \mathbf{\Psi}_j^m(\acute{\mathbf{x}})\bar{\mathbf{\Psi}}_j^n(\acute{\mathbf{x}})d\acute{\mathbf{x}}.
\end{aligned}$$

Arranging terms to the same side

$$(\lambda^m - \lambda^n)\int_D \mathbf{\Psi}_i^m(\mathbf{x})\bar{\mathbf{\Psi}}_i^n(\mathbf{x})d\mathbf{x} = 0. \tag{A.25}$$

Because $\lambda^m \neq \lambda^n$ for $m \neq n$, this equation must be orthogonal, i.e.,

$$\int_D \mathbf{\Psi}_i^m(\mathbf{x})\overline{\mathbf{\Psi}}_i^n(\mathbf{x})d\mathbf{x} = 0 \quad \text{for} \quad m \neq n. \tag{A.26}$$

In addition to the orthogonality, orthonormality condition, $(\mathbf{\Psi}_i^m, \mathbf{\Psi}_i^n) = \delta_{mn}$, simplifies the decomposition of the velocity and temperature fields. A velocity or temperature field can be expressed as a summation of the eigenfunctions with time dependent coefficients

$$v_i(\mathbf{x}, t) = \sum_m a_m(t)\mathbf{\Psi}_i^m(\mathbf{x}). \tag{A.27}$$

If this equation is multiplied by $\overline{\mathbf{\Psi}}_i^n(\mathbf{x})$ and integrated over the domain D, the expression of time dependent coefficients becomes

$$\int_D \overline{\mathbf{\Psi}}_i^n(\mathbf{x})v_i(\mathbf{x}, t)d\mathbf{x} = \sum_m a_m(t)\int_D \overline{\mathbf{\Psi}}_i^n(\mathbf{x})\mathbf{\Psi}_i^m(\mathbf{x})d\mathbf{x} = \sum_m a_m(t)\delta_{mn}, \tag{A.28}$$

where

$$a_n(t) = \int_D \overline{\mathbf{\Psi}}_i^n(\mathbf{x})v_i(\mathbf{x}, t)d\mathbf{x}. \tag{A.29}$$

Using this equation, time dependent coefficients can be obtained by integrating the product of the velocity or temperature and the eigenfunction. These time dependent coefficients are the magnitude of the corresponding eigenfunctions and used to reconstruct velocity or temperature field as indicated in equation (A.27).

A.1.4 TRANSLATIONAL INVARIANCE AND DISCRETE SYMMETRIES

The flow field for Rayleigh Bénard convection have discrete symmetries in x_1, x_2, x_3 directions and translational invariance in x_1, x_2 directions. So, each symmetry produces an equally valid flow field which can be incorporated into the original flow and hence the statistical sample can be enhanced. Addition of an arbitrary value l to x_1 produces a new velocity or temperature field, $v_i^n = (x_1 + l, x_2, x_3)$. The new kernel is evaluated from a summation over time and over the domain of the new velocity or temperature field

$$K_{ij} = \sum_{n=1}^{N}\int_0^{L_1} v_i^n(x_1 + l, x_2, x_3)\overline{v}_j^n(\acute{x_1} + l, \acute{x_2}, \acute{x_3})dl. \tag{A.30}$$

The kernel can be rewritten in terms of the dummy variable $s = \acute{x_1} + l$ with $x_1 + l = s + x_1 - \acute{x_1}$ and $dl = ds$, as

$$K_{ij} = \sum_{n=1}^{N} \int_{\acute{x_1}}^{\acute{x_1}+L_1} v_i^n(x_1 - \acute{x_1} + s, x_2, x_3)\bar{v}_j^n(s, \acute{x_2}, \acute{x_3})ds. \tag{A.31}$$

This integral equation depend only on $x_1 - \acute{x_1}$ and integral limits can be replaced by 0 and L_1 respectively, because of the periodicity in x_1 direction. The same analysis can be performed in x_2 direction because periodicity and translational invariance are also valid in this direction:

$$\begin{aligned} &K_{ij}(x_1 - \acute{x_1}, x_2 - \acute{x_2}, x_3, \acute{x_3}) = \\ &\sum_{n=1}^{N} \int_0^{L_1} \int_0^{L_2} v_i^n(x_1 - \acute{x_1} + s_1, x_2 - \acute{x_2} + s_2, x_3)\bar{v}_j^n(s_1, s_2, \acute{x_3})ds_2 ds_1. \end{aligned} \tag{A.32}$$

The original eigenproblem is

$$\int_0^{L_1} \int_0^{L_2} \int_{-1}^{1} K_{ij}(x_1 - \acute{x_1}, x_2 - \acute{x_2}, x_3, \acute{x_3})\mathbf{\Psi}_j(\acute{x_1}, \acute{x_2}, \acute{x_3})d\acute{x_3}d\acute{x_2}d\acute{x_1} = \lambda\mathbf{\Psi}_i(x_1, x_2, x_3). \tag{A.33}$$

Multiplying both sides by complex exponentials, $e^{-i2\pi k_1 x_1/L_1} e^{-i2\pi k_2 x_2/L_2}$ and integrating in x_1 and x_2 directions give the equation

$$\begin{aligned} &\int_{-1}^{1} d\acute{x_3} \int_0^{L_1} \int_0^{L_2} e^{-i2\pi k_1 x_1/L_1} e^{-i2\pi k_2 x_2/L_2} \mathbf{\Psi}_j(\acute{x_1}, \acute{x_2}, \acute{x_3}) \\ &\int_0^{L_1} \int_0^{L_2} K_{ij}(x_1 - \acute{x_1}, x_2 - \acute{x_2}, x_3, \acute{x_3})e^{-i2\pi k_1(x_1-\acute{x_1})/L_1} e^{-i2\pi k_2(x_2-\acute{x_2})/L_2} dx_2 dx_1 d\acute{x_2} d\acute{x_1} \\ &= \lambda \int_0^{L_1} \int_0^{L_2} \mathbf{\Psi}_i(x_1, x_2, x_3)e^{-i2\pi k_1 x_1/L_1} e^{-i2\pi k_2 x_2/L_2} dx_2 dx_1, \end{aligned} \tag{A.34}$$

which can be rewritten as

$$\int_0^{L_3} \hat{\mathbf{\Psi}}_j(k_1, k_2, x_3)\hat{K}_{ij}(k_1, k_2, x_3, \acute{x_3})d\acute{x_3} = \lambda\hat{\mathbf{\Psi}}_i(k_1, k_2, x_3), \tag{A.35}$$

where the hat symbol represents the Fourier transform of the quantity in x_1 and x_2 directions. $\hat{K}_{ij}$ can be evaluated from the transformed field vectors. If equation (A.32) is multiplied by the complex exponentials and integrated over x_1 and x_2 directions, thetransformed kernel yields

$$\begin{aligned} \hat{K}_{ij} = &\sum_{n=1}^{N} \int_0^{L_1} \int_0^{L_2} \int_0^{L_1} \int_0^{L_2} v_i^n(x_1 - \acute{x_1} + s_1, x_2 - \acute{x_2} + s_2, x_3)\bar{v}_j^n(s_1, s_2, \acute{x_3})e^{-i2\pi k_1(x_1-\acute{x_1})/L_1} \\ &e^{-i2\pi k_2(x_2-\acute{x_2})/L_2} dx_2 dx_1 ds_2 ds_1. \end{aligned}$$

Changing the variables with $x_1^\star = x_1 - \acute{x_1} + s_1$ and $x_2^\star = x_2 - \acute{x_2} + s_2$ and separating the complex exponentials, give

$$\hat{K}_{ij} = \sum_{n=1}^{N} \int_0^{L_1} \int_0^{L_2} \overline{v}_j^n(s_1, s_2, \acute{x_3}) e^{i2\pi k_1 s_1/L_1} e^{i2\pi k_2 s_2/L_2}$$
$$\int_{-x_1+s_1}^{L_1-x_1+s_1} \int_{-x_2+s_2}^{L_2-x_2+s_2} v_i^n(x_1^\star, x_2^\star, x_3) e^{-i2\pi k_1 x_1^\star/L_1} e^{-i2\pi k_2 x_2^\star/L_2} dx_2^\star dx_1^\star ds_2 ds_1.$$

The velocity and temperature fields are periodic in x_1 and x_2 directions. Therefore, the last two integrals can be rewritten from 0 to L_1 and from 0 to L_2. $\hat{v}_i^n(k_1, k_2, x_3)$ is the Fourier transform of the velocity or temperature fields. The kernel is the summation of the first two integrals because the last two integrals are independent of s_1 and s_2. The first two integrals can be rewritten as

$$\overline{\int_0^{L_1} \int_0^{L_2} v_j^n(s_1, s_2, \acute{x_3}) e^{-i2\pi k_1 s_1/L_1} e^{-i2\pi k_2 s_2/L_2} ds_2 ds_1} = \overline{\hat{v}}_j^n(k_1, k_2, \acute{x_3}). \tag{A.36}$$

Then the transformed kernel can be evaluated as

$$\hat{K}_{ij}(k_1, k_2, x_3, \acute{x_3}) = \sum_{n=1}^{N} \hat{v}_i^n(k_1, k_2, x_3) \overline{\hat{v}}_j^n(k_1, k_2, \acute{x_3}). \tag{A.37}$$

The decomposition is evaluated in x_3 direction using the transformed kernel. Evaluation must be performed for each Fourier mode (k_1, k_2) and quantum number q so the eigenvector is

$$\mathbf{\Psi}_i^{\mathbf{k}}(x_1, x_2, x_3) = \hat{\mathbf{\Psi}}_i^q(k_1, k_2, x_3) e^{i2\pi k_1 x_1/L_1} e^{i2\pi k_2 x_2/L_2}, \tag{A.38}$$

where $\mathbf{k} = (k_1, k_2, q)$. In addition to the translational invariance, discrete symmetries in x_1, x_2 direction and vertical midplane increase the dataset by a factor of eight. Each discrete symmetry produces a new flow field satisfying the boundary conditions and the governing equations. More specifically, with

$$\mathbf{v}^{n_1^+} = (v_1(x_1, x_2, x_3), v_2(x_1, x_2, x_3), v_3(x_1, x_2, x_3), T(x_1, x_2, x_3)), \tag{A.39}$$

and its vertical symmetry

$$\mathbf{v}^{n_1^-} = (v_1(x_1, x_2, -x_3), v_2(x_1, x_2, -x_3), -v_3(x_1, x_2, -x_3), -T(x_1, x_2, -x_3)), \tag{A.40}$$

the flow ensemble can be increased 16-fold by

$$
\begin{aligned}
\mathbf{v}^{n_2^\pm} &= (-v_1(-x_1, x_2, \pm x_3), v_2(-x_1, x_2, \pm x_3), \pm v_3(-x_1, x_2, \pm x_3), \pm T(-x_1, x_2, \pm x_3)),\\
\mathbf{v}^{n_3^\pm} &= (v_1(x_1, -x_2, \pm x_3), -v_2(x_1, -x_2, \pm x_3), \pm v_3(x_1, -x_2, \pm x_3), \pm T(x_1, -x_2, \pm x_3)),\\
\mathbf{v}^{n_4^\pm} &= (-v_1(-x_1, -x_2, \pm x_3), -v_2(-x_1, -x_2, \pm x_3), \pm v_3(-x_1, -x_2, \pm x_3), \pm T(-x_1, -x_2, \pm x_3)),\\
\mathbf{v}^{n_5^\pm} &= (v_2(x_2, x_1, \pm x_3), v_1(x_2, x_1, \pm x_3), \pm v_3(x_2, x_1, \pm x_3), \pm T(x_2, x_1, \pm x_3)),\\
\mathbf{v}^{n_6^\pm} &= (-v_2(-x_2, x_1, \pm x_3), v_1(-x_2, x_1, \pm x_3), \pm v_3(-x_2, x_1, \pm x_3), \pm T(-x_2, x_1, \pm x_3)),\\
\mathbf{v}^{n_7^\pm} &= (v_2(x_2, -x_1, \pm x_3), -v_1(x_2, -x_1, \pm x_3), \pm v_3(x_2, -x_1, \pm x_3), \pm T(x_2, -x_1, \pm x_3)),\\
\mathbf{v}^{n_8^\pm} &= (-v_2(-x_2, -x_1, \pm x_3), -v_1(-x_2, -x_1, \pm x_3), \pm v_3(-x_2, -x_1, \pm x_3), \pm T(-x_2, -x_1, \pm x_3)),
\end{aligned}
$$

where the last four symmetries are valid only when the horizontal planform of the computational domain is a square, that is, $L_1 = L_2$. From these realistic fields the Fourier transforms of the increased dataset can be rewritten in terms of the original form as

$$
\begin{aligned}
\hat{\mathbf{v}}^{n_1^\pm} &= (\hat{v}_1(k_1, k_2, \pm x_3), \hat{v}_2(k_1, k_2, \pm x_3), \pm\hat{v}_3(k_1, k_2, \pm x_3), \pm\hat{T}(k_1, k_2, \pm x_3)),\\
\hat{\mathbf{v}}^{n_2^\pm} &= (-\hat{v}_1(-k_1, k_2, \pm x_3), \hat{v}_2(-k_1, k_2, \pm x_3), \pm\hat{v}_3(-k_1, k_2, \pm x_3), \pm\hat{T}(-k_1, k_2, \pm x_3)),\\
\hat{\mathbf{v}}^{n_3^\pm} &= (\hat{v}_1(k_1, -k_2, \pm x_3), -\hat{v}_2(k_1, -k_2, \pm x_3), \pm\hat{v}_3(k_1, -k_2, \pm x_3), \pm\hat{T}(k_1, -k_2, \pm x_3)),\\
\hat{\mathbf{v}}^{n_4^\pm} &= (-\hat{v}_1(-k_1, -k_2, \pm x_3), -\hat{v}_2(-k_1, -k_2, \pm x_3), \pm\hat{v}_3(-k_1, -k_2, \pm x_3), \pm\hat{T}(-k_1, -k_2, \pm x_3)),\\
\hat{\mathbf{v}}^{n_5^\pm} &= (\hat{v}_2(k_2, k_1, \pm x_3), \hat{v}_1(k_2, k_1, \pm x_3), \pm\hat{v}_3(k_2, k_1, \pm x_3), \pm\hat{T}(k_2, k_1, \pm x_3)), \qquad (A.41)\\
\hat{\mathbf{v}}^{n_6^\pm} &= (-\hat{v}_2(-k_2, k_1, \pm x_3), \hat{v}_1(-k_2, k_1, \pm x_3), \pm\hat{v}_3(-k_2, k_1, \pm x_3), \pm\hat{T}(-k_2, k_1, \pm x_3)),\\
\hat{\mathbf{v}}^{n_7^\pm} &= (\hat{v}_2(k_2, -k_1, \pm x_3), -\hat{v}_1(k_2, -k_1, \pm x_3), \pm\hat{v}_3(k_2, -k_1, \pm x_3), \pm\hat{T}(k_2, -k_1, \pm x_3)),\\
\hat{\mathbf{v}}^{n_8^\pm} &= (-\hat{v}_2(-k_2, -k_1, \pm x_3), -\hat{v}_1(-k_2, -k_1, \pm x_3), \pm\hat{v}_3(-k_2, -k_1, \pm x_3), \pm\hat{T}(-k_2, -k_1, \pm x_3)).
\end{aligned}
$$

The improved form of the kernel is

$$
\hat{K}_{ij}(k_1, k_2, x_3, \acute{x}_3) = \sum_{n=1}^{N} \sum_{p=1}^{8} \hat{v}_i^{n_p^\pm}(k_1, k_2, x_3)\bar{\hat{v}}_j^{n_p^\pm}(k_1, k_2, \acute{x}_3). \qquad (A.42)
$$

The effect of symmetry $n_3^{\pm}$ on the kernel is

$$
\begin{aligned}
\hat{K}_{11}(k_1,-k_2,x_3,\acute{x_3}) &= \hat{K}_{11}(k_1,k_2,x_3,\acute{x_3}),\\
\hat{K}_{12}(k_1,-k_2,x_3,\acute{x_3}) &= -\hat{K}_{12}(k_1,k_2,x_3,\acute{x_3}),\\
\hat{K}_{13}(k_1,-k_2,x_3,\acute{x_3}) &= \hat{K}_{13}(k_1,k_2,x_3,\acute{x_3}),\\
\hat{K}_{14}(k_1,-k_2,x_3,\acute{x_3}) &= \hat{K}_{14}(k_1,k_2,x_3,\acute{x_3}),\\
\hat{K}_{21}(k_1,-k_2,x_3,\acute{x_3}) &= -\hat{K}_{21}(k_1,k_2,x_3,\acute{x_3}),\\
\hat{K}_{22}(k_1,-k_2,x_3,\acute{x_3}) &= \hat{K}_{22}(k_1,k_2,x_3,\acute{x_3}),\\
\hat{K}_{23}(k_1,-k_2,x_3,\acute{x_3}) &= -\hat{K}_{23}(k_1,k_2,x_3,\acute{x_3}),\\
\hat{K}_{24}(k_1,-k_2,x_3,\acute{x_3}) &= -\hat{K}_{24}(k_1,k_2,x_3,\acute{x_3}),\\
\hat{K}_{31}(k_1,-k_2,x_3,\acute{x_3}) &= \hat{K}_{31}(k_1,k_2,x_3,\acute{x_3}),\\
\hat{K}_{32}(k_1,-k_2,x_3,\acute{x_3}) &= -\hat{K}_{32}(k_1,k_2,x_3,\acute{x_3}),\\
\hat{K}_{33}(k_1,-k_2,x_3,\acute{x_3}) &= \hat{K}_{33}(k_1,k_2,x_3,\acute{x_3}),\\
\hat{K}_{34}(k_1,-k_2,x_3,\acute{x_3}) &= \hat{K}_{34}(k_1,k_2,x_3,\acute{x_3}),\\
\hat{K}_{41}(k_1,-k_2,x_3,\acute{x_3}) &= \hat{K}_{41}(k_1,k_2,x_3,\acute{x_3}),\\
\hat{K}_{42}(k_1,-k_2,x_3,\acute{x_3}) &= -\hat{K}_{42}(k_1,k_2,x_3,\acute{x_3}),\\
\hat{K}_{43}(k_1,-k_2,x_3,\acute{x_3}) &= \hat{K}_{43}(k_1,k_2,x_3,\acute{x_3}),\\
\hat{K}_{44}(k_1,-k_2,x_3,\acute{x_3}) &= \hat{K}_{44}(k_1,k_2,x_3,\acute{x_3}).
\end{aligned}
\tag{A.43}
$$

If it is assumed that $(\hat{\mathbf{\Psi}}_1(k_1,k_2,x_3),\hat{\mathbf{\Psi}}_2(k_1,k_2,x_3),\hat{\mathbf{\Psi}}_3(k_1,k_2,x_3),\hat{\mathbf{\Psi}}_4(k_1,k_2,x_3))$ is the solution of the (A.35), then the symmetry above leads

$$(\hat{\mathbf{\Psi}}_1(k_1,-k_2,x_3),-\hat{\mathbf{\Psi}}_2(k_1,-k_2,x_3),\hat{\mathbf{\Psi}}_3(k_1,-k_2,x_3),\hat{\mathbf{\Psi}}_4(k_1,-k_2,x_3)), \tag{A.44}$$

as the solution to $\hat{K}_{ij}(k_1,-k_2,x_3,\acute{x_3})$ with the same eigenvalue. Therefore, it only requires to solve the problem for $x_2 \geq 0$. Similarly, x_1 direction have the symmetry n_2^{+} so only the solution of the problem for $x_1 \geq 0$ is needed. Using the property of the Fourier transform

$$\hat{v}_i(-k_1,-k_2,x_3) = \bar{\hat{v}}_i(k_1,k_2,x_3), \tag{A.45}$$

and similarly for the kernel

$$\hat{K}_{ij}(-k_1,-k_2,x_3) = \bar{\hat{K}}_{ij}(k_1,k_2,x_3). \tag{A.46}$$

The complex conjugate of equation (A.35) tends to $\bar{\hat{\boldsymbol{\Psi}}}(-k_1, -k_2, x_3)$ for corresponding kernel $\hat{K}_{ij}(-k_1, -k_2, x_3)$ with the same eigenvalue. Using the solution of this equation for the set of wavenumbers (k_1, k_2), $k_1 > 0$ and $k_2 > 0$, three additional solutions can be obtained for $(-k_1, k_2), (k_1, -k_2), (-k_1, -k_2)$ using the symmetries. Similarly, for (k_1, k_2) a square planform only requires solution of (A.35) for $k_1 \geq k_2 \geq 0$. As a result, eigenfunctions come with a maximum degeneracy of 8-fold. An eigenvalue of the mode $(0, 0)$ has degeneracy 1. On the other hand, eigenfunction of the mode $(1, 0)$ or $(0, 1)$ has degeneracy 4 and the others has degeneracy 8. The time dependent coefficients can still be computed using (A.29) with three parameters $\mathbf{k}(k_1, k_2, q)$,

$$a_{\mathbf{k}}(t) = \int_0^{L_1} \int_0^{L_2} \int_{-1}^{1} v_i(x_1, x_2, x_3, t) \bar{\hat{\boldsymbol{\Psi}}}_i^q(k_1, k_2, x_3) e^{\frac{-i2\pi k_1 x_1}{L_1}} e^{\frac{-i2\pi k_2 x_2}{L_2}} dx_1 dx_2 dx_3, \quad \text{(A.47)}$$

or

$$a_{\mathbf{k}}(t) = \int_{-1}^{1} \hat{v}_i(k_1, k_2, x_3, t) \bar{\hat{\boldsymbol{\Psi}}}_i^q(k_1, k_2, x_3) dx_3. \quad \text{(A.48)}$$

Appendix B

FLOWCHART OF DIVERGENCE FREE SIMULATION

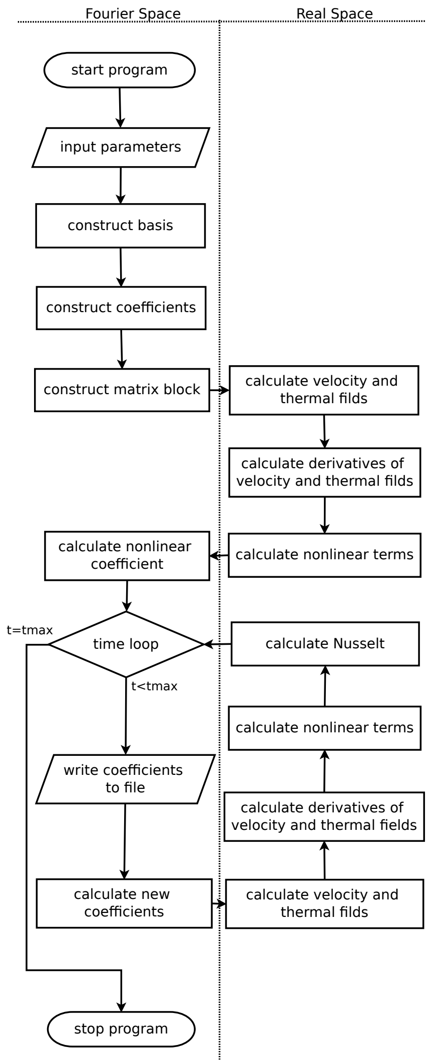

Figure B.1: Flowchart of nonlinear simulation with divergence free basis

REFERENCES

[1] R. M. Clever and F. H. Busse, "Transition to time-dependent convection," *Journal of Fluid Mechanics*, vol. 65, pp. 625–645, Oct. 1974.

[2] S. Chandrasekhar, *Hydrodynamic and hydromagnetic stability*. International Series of Monographs on Physics, Oxford: Clarendon, 1961.

[3] W. V. R. Malkus, "The heat transport and spectrum of thermal turbulence," *Proceedings of the Royal Society of London. Series A, Mathematical and Physical Sciences*, vol. 225, no. 1161, pp. pp. 196–212, 1954.

[4] W. V. R. Malkus and G. Veronis, "Finite amplitude cellular convection," *Journal of Fluid Mechanics*, vol. 4, no. 03, pp. 225–260, 1958.

[5] A. Schlüter, D. Lortz, and F. Busse, "On the stability of steady finite amplitude convection," *Journal of Fluid Mechanics*, vol. 23, no. 01, pp. 129–144, 1965.

[6] W. H. Plows, "Some numerical results for two-dimensional steady laminar b[e-acute]nard convection," *Physics of Fluids*, vol. 11, no. 8, pp. 1593–1599, 1968.

[7] F. H. Busse and J. A. Whitehead, "Instabilities of convection rolls in a high prandtl number fluid," *Journal of Fluid Mechanics*, vol. 47, no. 02, pp. 305–320, 1971.

[8] F. H. Busse and J. A. Whitehead, "Oscillatory and collective instabilities in large prandtl number convection," *Journal of Fluid Mechanics*, vol. 66, no. 01, pp. 67–79, 1974.

[9] R. M. Clever and F. H. Busse, "Low-prandtl-number convection in a layer heated from below," *Journal of Fluid Mechanics*, vol. 102, pp. 61–74, 1981.

[10] H. Frick, F. H. Busse, and R. M. Clever, "Steady three-dimensional convection at high prandtl numbers," *Journal of Fluid Mechanics*, vol. 127, pp. 141–153, 1983.

[11] R. M. Clever and F. H. Busse, "Nonlinear oscillatory convection," *Journal of Fluid Mechanics*, vol. 176, pp. 403–417, 1987.

[12] F. H. Busse and R. M. Clever, "Symmetry considerations in the numerical analysis of bifurcation sequences," *Lectures in Applied Mathematics*, vol. 29, pp. 125–135, 1993.

[13] F. B. Lipps, "Numerical simulation of three-dimensional bénard convection in air," *Journal of Fluid Mechanics*, vol. 75, no. 01, pp. 113–148, 1976.

[14] G. Grötzbach, "Direct numerical simulation of laminar and turbulent bénard convection," *Journal of Fluid Mechanics*, vol. 119, pp. 27–53, 1982.

[15] G. Grötzbach, “Spatial resolution requirements for direct numerical simulation of the Rayleigh-Benard convection,” *Journal of Computational Physics*, vol. 49, pp. 241–264, Feb. 1983.

[16] J. B. McLaughlin and S. A. Orszag, “Transition from periodic to chaotic thermal convection,” *Journal of Fluid Mechanics*, vol. 122, pp. 123–142, 1982.

[17] M. Meneguzzi, C. Sulem, P. L. Sulem, and O. Thual, “Three-dimensional numerical simulation of convection in low-prandtl-number fluids,” *Journal of Fluid Mechanics*, vol. 182, pp. 169–191, 1987.

[18] R. Verzicco and R. Camussi, “Prandtl number effects in convective turbulence,” *Journal of Fluid Mechanics*, vol. 383, pp. 55–73, Mar. 1999.

[19] L. Guessous, *A pseudospectral numerical scheme for the simulation of natural flows*. PhD thesis, University of Michigan, 1999.

[20] L. Guessous, “a Pseudo-Spectral Numerical Scheme for the Simulation of Steady and Oscillating Wall-Bounded Flows,” *Numerical Heat Transfer Part B - Fundamentals*, vol. 45, pp. 135–157, Feb. 2004.

[21] R. Krishnamurti, “Some further studies on the transition to turbulent convection,” *Journal of Fluid Mechanics*, vol. 60, no. 02, pp. 285–303, 1973.

[22] J. P. Gollub and S. V. Benson, “Many routes to turbulent convection,” *Journal of Fluid Mechanics*, vol. 100, no. 03, pp. 449–470, 1980.

[23] F. H. Busse, “The oscillatory instability of convection rolls in a low prandtl number fluid,” *Journal of Fluid Mechanics*, vol. 52, no. 01, pp. 97–112, 1972.

[24] F. B. Lipps and R. C. J. Somerville, “Dynamics of variable wavelength in finite-amplitude b[e-acute]nard convection,” *Physics of Fluids*, vol. 14, no. 4, pp. 759–765, 1971.

[25] E. L. Koschmieder, *Bénard Cells and Taylor Vortices*. Feb. 1993.

[26] M. S. Miesch, “The coupling of solar convection and rotation - (invited review),” *Solar Physics*, vol. 192, pp. 59–89, 2000. 10.1023/A:1005260527450.

[27] M. Evonuk and G. A. Glatzmaier, “The effects of rotation rate on deep convection in giant planets with small solid cores,” *Planetary and Space Science*, vol. 55, no. 4, pp. 407 – 412, 2007.

[28] G. Veronis, “Motions at subcritical values of the rayleigh number in a rotating fluid,” *Journal of Fluid Mechanics*, vol. 24, no. 03, pp. 545–554, 1966.

[29] G. Veronis, “Cellular convection with finite amplitude in a rotating fluid,” *Journal of Fluid Mechanics*, vol. 5, no. 03, pp. 401–435, 1959.

[30] G. Veronis, “Large-amplitude bénard convection in a rotating fluid,” *Journal of Fluid Mechanics*, vol. 31, no. 01, pp. 113–139, 1968.

[31] R. M. Clever and F. H. Busse, “Nonlinear properties of convection rolls in a horizontal layer rotating about a vertical axis,” *Journal of Fluid Mechanics*, vol. 94, no. 04, pp. 609–627, 1979.

[32] H. T. Rossby, “A study of bénard convection with and without rotation,” *Journal of Fluid Mechanics*, vol. 36, no. 02, pp. 309–335, 1969.

[33] G. Küppers and D. Lortz, “Transition from laminar convection to thermal turbulence in a rotating fluid layer,” *Journal of Fluid Mechanics*, vol. 35, no. 03, pp. 609–620, 1969.

[34] G. Küppers, “The stability of steady finite amplitude convection in a rotating fluid layer,” *Physics Letters A*, vol. 32, no. 1, pp. 7–8, 1970. cited By (since 1996) 31.

[35] R. C. J. Somerville and F. B. Lipps, “A Numerical Study in Three Space Dimensions of Bénard Convection in a Rotating Fluid.,” *Journal of Atmospheric Sciences*, vol. 30, pp. 590–596, May 1973.

[36] T. K. E. Clune, “Pattern selection in rotating convection with experimental boundary conditions,” *Physical Review E*, vol. 47, no. 4, pp. 2536–2550, 1993.

[37] J. D. Scheel, *Rotating Rayleigh-Benard convection*. PhD thesis, California Institute of Technology, 2007.

[38] R. B. F. Clever, “Convection in a low prandtl number fluid layer rotating about a vertical axis,” *European Journal of Mechanics, B/Fluids*, vol. 19, no. 2, pp. 213–227, 2000.

[39] E. Kurt, F. Busse, and W. Pesch, “Hydromagnetic convection in a rotating annulus with an azimuthal magnetic field,” *Theoretical and Computational Fluid Dynamics*, vol. 18, pp. 251–263, 2004. 10.1007/s00162-004-0132-6.

[40] E. Kurt, W. Pesch, and F. H. Busse, “Pattern formation in the rotating cylindrical annulus with an azimuthal magnetic field at low prandtl numbers,” *Journal of Vibration and Control*, vol. 13, no. 9-10, pp. 1321–1330, 2007.

[41] K. Karhunen, “Zur spektraltheorie stochasticher prozesse,” *Annales Academiae Scientiarum Fennicae Series A I. Mathematica-Physica*, vol. 37, 1946.

[42] M. Loéve, *Probability Theory*. Springer-Verlag, 1977.

[43] E. N. Lorenz, “Empirical orthogonal functions and statistical weather prediction,” Tech. Rep. Statistical Forecasting Project, MIT, Department of Meteorology, Cambridge,Massachusetts, 1956.

[44] J. L. Lumley, “The structure of inhomogeneous turbulence,” in *Atmospheric Turbulence and Wave Propagation* (A. M. Yaglom, V. I. Tatarski, ed.), pp. 166–178, 1967.

[45] J. L. Lumley, *Stochastic Tools in Turbulence*. Academic Press / New York, 1970.

[46] J. L. L. Philip Holmes and G. Berkooz, *Turbulence, Coherent Structures, Dynamical Systems and Symmetry*. Cambridge University Press, 1996.

[47] L. Sirovich, “Turbulence and the dynamics of coherent structures. I - Coherent structures.,” *Quarterly of Applied Mathematics*, vol. 45, pp. 561–571, Oct. 1987.

[48] L. Sirovich, “Turbulence and the dynamics of coherent structures. II - Symmetries and transformations.,” *Quarterly of Applied Mathematics*, vol. 45, pp. 573–582, Oct. 1987.

[49] L. Sirovich, “Turbulence and the dynamics of coherent structures. III - Dynamics and scaling,” *Quarterly of Applied Mathematics*, vol. 45, pp. 583–590, Oct. 1987.

[50] G. Webber and R. Handler, “The karhunen-loéve decomposition of minimal channel flow,” *Physics of Fluids*, vol. 9, no. 4, p. 1054, 1997.

[51] Webber, G.A., *The Karhunen-Loéve decomposition of minimal channel flow*. PhD thesis, Brown University, 1996.

[52] I. Hakan Tarman, “A Karhunen-Loéve Analysis of Turbulent Thermal Convection,” *International Journal for Numerical Methods in Fluids*, vol. 22, pp. 67–79, Jan. 1996.

[53] I. H. Tarman, “A karhunen-loéve based galerkin approximation to boussinesq equation,” *Computer Methods in Applied Mechanics and Engineering*, vol. 137, no. 3-4, pp. 275 – 284, 1996.

[54] I. H. Tarman, “An improved dynamical approximation to boussinesq equation using karhunen-loéve basis,” *Computer Methods in Applied Mechanics and Engineering*, vol. 144, no. 1-2, pp. 153 – 162, 1997.

[55] H. I. Tarman and L. Sirovich, “Extensions to karhunen-loéve based approximation of complicated phenomena,” *Computer Methods in Applied Mechanics and Engineering*, vol. 155, no. 3-4, pp. 359 – 368, 1998.

[56] H. I. Tarman, “A karhunen-loéve-based approach to numerical simulation of transition in rayleigh-benard convection,” *Numerical Heat Transfer Part B: Fundamentals*, vol. 43, pp. 567–586(20), June 2003.

[57] C. Yıldırım, D. Yarımpabuç, and H. I. Tarman, “Transitional Dynamics in Thermal Convection Between Rigid Plates,” *Journal of Vibration and Control*, vol. 13, no. 9-10, pp. 1331–1342, 2007.

[58] S. A. Orszag and L. C. Kells, “Transition to turbulence in plane poiseuille and plane couette flow,” *Journal of Fluid Mechanics*, vol. 96, no. 01, pp. 159–205, 1980.

[59] L. Kleiser and U. Schumann, “Treatment of incompressibility and boundary conditions in 3-D numerical spectral simulations of plane channel flows,” in *3rd Conference on Numerical Methods in Fluid Mechanics* (E. H. Hirschel, ed.), pp. 165–173, 1980.

[60] R. D. Moser, P. Moin, and A. Leonard, “A spectral numerical method for the Navier-Stokes equations with applications to Taylor-Couette flow,” *Journal of Computational Physics*, vol. 52, pp. 524–544, Dec. 1983.

[61] R. Kessler, “Nonlinear transition in three-dimensional convection,” *Journal of Fluid Mechanics*, vol. 174, pp. 357–379, 1987.

[62] B. R. Noack and H. Eckelmann, “A low-dimensional Galerkin method for the three-dimensional flow around a circular cylinder,” *Physics of Fluids*, vol. 6, pp. 124–143, Jan. 1994.

[63] A. Y. Gelfgat, “Different modes of rayleigh-bénard instability in two- and three-dimensional rectangular enclosures,” *J. Comput. Phys.*, vol. 156, pp. 300–324, December 1999.

[64] D. Puigjaner, J. Herrero, F. Giralt, and C. Simó, “Stability analysis of the flow in a cubical cavity heated from below,” *Physics of Fluids*, vol. 16, pp. 3639–3655, Oct. 2004.

[65] A. Meseguer and L. N. Trefethen, “A spectral petrov-galerkin formulation for pipe flow i: Linear stability and transient growth,” tech. rep., Oxford University Computing Laboratory, 2000.

[66] A. Meseguer and L. N. Trefethen, “A spectral petrov-galerkin formulation for pipe flow ii: Nonlinear transitional stages,” tech. rep., Oxford University Computing Laboratory, 2001.

[67] A. Meseguer and L. N. Trefethen, “Linearized pipe flow to reynolds number 10^7,” *Journal of Computational Physics*, vol. 186, no. 1, pp. 178 – 197, 2003.

[68] A. T. Patera, “A spectral element method for fluid dynamics: Laminar flow in a channel expansion,” *Journal of Computational Physics*, vol. 54, no. 3, pp. 468 – 488, 1984.

[69] N. Becker, J. D. Scheel, M. C. Cross, and G. Ahlers, “Effect of the centrifugal force on domain chaos in rayleigh-bénard convection,” *Phys. Rev. E*, vol. 73, p. 066309, Jun 2006.

[70] M. R. Schumack, W. W. Schultz, and J. P. Boyd, “Spectral method solution of the stokes equations on nonstaggered grids,” *Journal of Computational Physics*, vol. 94, no. 1, pp. 30 – 58, 1991.

[71] C. Canuto, “Spectral methods for viscous, incompressible flows,” in *Algorithmic Trends in Computational Fluid Dynamics; The Institute for Computer Applications in Science and Engineering (ICASE)/LaRC Workshop* (M. Y. Hussaini, A. Kumar, & M. D. Salas, ed.), pp. 169–193, 1993.

[72] J. Boyd and J. Boyd, *Chebyshev and Fourier spectral methods*. Dover books on mathematics, Dover Publications, 2001.

[73] R. Krishnamurti, “On the transition to turbulent convection. part 1. the transition from two- to three-dimensional flow,” *Journal of Fluid Mechanics*, vol. 42, no. 02, pp. 295–307, 1970.

[74] W. H. Reid and D. L. Harris, “Some Further Results on the Bénard Problem,” *Physics of Fluids*, vol. 1, pp. 102–110, Mar. 1958.

[75] A. Meseguer and F. Mellibovsky, “On a solenoidal fourier–chebyshev spectral method for stability analysis of the hagen–poiseuille flow,” *Appl. Numer. Math.*, vol. 57, pp. 920–938, August 2007.

[76] J. A. Weideman and S. C. Reddy, "A matlab differentiation matrix suite," *ACM Trans. Math. Softw.*, vol. 26, pp. 465–519, December 2000.

VITA

Cihan YILDIRIM

Department of Engineering Science
Middle East Technical University
06531 Çankaya, Ankara, TURKEY
Phone : +90 312 210 23 86
E-Mail : ycihan@metu.edu.tr

Personal Information

Nationality : Turkish
Age : 30
Profession : Mechanical Engineer

Languages

English (Proficiency - high)

Academic Background

Doctor of Philosophy in Engineering Science at Middle East Technical University, Ankara, Turkey
GPA : 3.29/4.0
Major : Computational Fluid Dynamics

Dissertation Topic: "NUMERICAL STUDY OF RAYLEIGH BÉNARD THERMAL CONVECTION VIA SOLENOIDAL BASES "
Advisor: Assoc. Prof. Dr. Hakan I. TARMAN

Bachelor of Mechanical Engineering at Osmangazi University, Eskisehir, Turkey, September 1, 2002.

Computer Proficiency

Operating System : Linux (especially Debian and Debian based distro), Unix (Solaris), Windows XP
Programming Language : Fortran, Shell scripting (bash)
Computing Software : Matlab, Mathematica, Mathcad

Certificate

High Performance Computing Workshop, 15 – 26 June 2009, National Centre for High Performance Computing, İstanbul Technical University, İstanbul, Turkey.

Experience

Research and Teaching Assistant, METU, 01 October 2002 - 2011.
System Administrator and Coordinator, METU, October 2005 - 2011.

Teaching Experience

As a teaching assistant hold office hours for the courses;
ES-223 Statics and Strength of Materials (1 semester)
ES-361 Computing Methods in Engineering (2 semester)
ES-503 Finite Element Method (3 semester)
ES-504 Numerical Solution of Partial Differential Equations (1 semester)
ES-510 Numerical Solution of Ordinary Differential Equations (2 semester)
ES-541 Introduction to Biomechanics (1 semester)

Publications

Yıldırım, C., Yarımpabuç, D. and Tarman, I. H., "Transitional Dynamics in Thermal Convection between Rigid Plates", Journal of Vibration and Control, 13: 1331-1342 (2007).

Yıldırım, C. and Tarman, I. H., İki Tabaka Arasındaki Doğal Isı Konveksiyonu Hareketinin Geçiş Evrelerinin Yapısal Analizi, XV. Ulusal Mekanik Kongresi (XV. National Congress of Mechanics), Isparta, 779-790, (2007)

Projects & Awards

- METU-BAP Phd. education support (2003-2011)
- TUBITAK-ARDEB scientific research project (2009-2011)

Social Activities and Memberships

- Member of METU Aikido Society, July 2005 till date (www.aikidoodtu.org)
- Member of METU Sub-aqua Society, September 2008 till date. (www.sat.metu.edu.tr)
- Member of The Chamber of Mechanical Engineers of Turkey, January 2003 till date. (www.mmo.org.tr)
- Member of Association of University Councils, September 2006 till date. (www.universitekonseyleri.org)